

SIMULATING THE EXPANSION OF
TURBULENT BOSE-EINSTEIN CONDENSATES

Bartholomew Andrews

MSci thesis carried out under the supervision of:
Prof. Thomas Gasenzer

Far-From-Equilibrium Quantum Dynamics Group
Institut für Theoretische Physik
Fakultät für Physik und Astronomie
Universität Heidelberg
2013

MSci thesis carried out for the degree title:

Physics with a Year in Europe
Imperial College London

Thesis written by

Bartholomew Andrews
London, UK

Date of submission: 21.06.13

Simulating the Expansion of Turbulent Bose-Einstein Condensates

In this thesis, turbulent Bose-Einstein condensates are modeled and simulated based on solutions to the semi-classical Gross-Pitaevskii equation, using a mean-field description. The initial configuration consists of a Gaussian free gas distribution, which is then propagated in imaginary time, under the influence of a harmonic trapping potential, to reach a ground state. During this process, turbulence is induced in the system by phase imprinting. The condensate is left to freely expand, from a variety of different turbulent states, in an expanding coordinate system. The time steps are iterated using a 4th-order Runge-Kutta scheme and the spatial derivatives are evaluated using finite differences. Motivated by the recent experiments of *Bagnato et al.*, a variety of different turbulent state variations are considered, in order to reproduce the experimentally observed self-similar free expansion of turbulent ellipsoidal condensates; including variations in vortex orientation, separation and density. The experimental condensates are modeled on anisotropic two-dimensional condensates with equally-oriented fcc vortex lattices. The results show that the rotation of the bulk condensate, the rate at which the vortices tend to an Abrikosov lattice configuration and the self-similarity of the free expansion, all increase with vortex density. Extrapolations of these trends agree with the experimental results.

Simulation der Expansion turbulenter Bose-Einstein-Kondensate

In dieser Arbeit werden turbulente Bose-Einstein-Kondensate modelliert und simuliert, basierend auf Lösungen der semi-klassischen Gross-Pitaevskii Gleichung, wobei die Molekularfeld Näherung verwendet wird. Die Anfangskonfiguration besteht aus einer gaußschen freien Gasverteilung und wird in Imaginär-Zeit entwickelt, unter dem Einfluss eines harmonischen Fallenpotentials, um den Grundzustand zu erreichen. Während dieses Prozesses wird Turbulenz im System induziert, indem der Kondensatphasenfunktion Vortices aufgeprägt werden. Dann wird die freie Expansion des Gases betrachtet, weswegen es in einem expandierenden Koordinatensystem simuliert wird. Hierbei wird das Bose-Gas ausgehend von verschiedenen turbulenten Anfangskonfigurationen betrachtet. Die Zeitschritte werden unter Anwendung des 4-stufigen Runge-Kutta Algorithmus iteriert und die räumlichen Ableitungen werden durch finite Differenzen ausgewertet. Motiviert durch aktuelle Experimente werden eine Vielzahl von verschiedenen turbulenten Zuständen untersucht, um die experimentell beobachtete selbstähnliche freie Ausdehnung der turbulenten ellipsenförmigen Kondensate zu reproduzieren, einschließlich Variationen von Vortex-orientierung, -trennung und -dichte. Die experimentellen Kondensate werden durch anisotrope zweidimensionale Kondensate mit gleich-orientierten fcc Vortex-Gittern modelliert. Die Ergebnisse zeigen, dass sowohl die Rotation des Bulk-Kondensats, als auch die Rate, mit der sich die Wirbel zu einem Abrikosov Gitter anordnen, als auch die Selbst-Ähnlichkeit der freien Expansion mit der Vortex Dichte vergrößern. Extrapolationen dieser Beobachtungen stimmen mit den experimentellen Ergebnissen überein.

*For my brother,
Philip Andrews*

Contents

Preface	xi
1 Introduction	1
2 Theoretical Foundation	5
2.1 Bose-Einstein Condensation	5
2.1.1 Theoretical Prediction	5
2.1.2 Experimental Observation	7
2.2 The Semi-Classical Gross-Pitaevskii Model	8
2.2.1 Assumptions and Limitations	8
2.2.2 The Gross-Pitaevskii Equation	9
2.3 Hydrodynamic Formulation and Topological Defects	11
2.4 Modelling Condensates using Gross-Pitaevskii Theory	12
2.4.1 Static Condensates	12
2.4.2 Expanding Condensates	13
2.5 Aspect Ratio Evolution in Turbulent Condensates	14
3 Solving the Linear Schrödinger Equation	17
3.1 The One-Dimensional Free TDSE	17
3.1.1 The Gaussian Wavepacket	17
3.1.2 Dimensionless Form for the One-Dimensional Case	18
3.1.3 Finite Differences	19
3.1.4 The Classical Runge-Kutta Algorithm	20
3.1.5 The One-Dimensional Exact Solution	20
3.1.6 The One-Dimensional Computed Solution	22
3.2 The Two-Dimensional Free TDSE	22
3.2.1 Dimensionless Form for the D -Dimensional Case	22
3.2.2 The Two-Dimensional Computed Solution	24
4 Simulating the Magnetic Trap Confinement of a Bose Gas	25
4.1 The Thomas-Fermi Distribution	25
4.2 The Thomas-Fermi Paraboloid	26
4.2.1 The One-Dimensional Case	26
4.2.2 The Two-Dimensional Case	27
4.3 Imaginary Time Propagation	28
4.3.1 Solving the GPE in Imaginary Time	28
4.3.2 The Particle Number Rescale Algorithm	29
4.4 The Dimensionless Gross-Pitaevskii Equation	30
4.5 Boundary Conditions	30
4.6 The Computed Solutions	31
5 Inducing Turbulence in the Trapped Bose Condensate	35
5.1 The Quantum Vortex	35

5.2	Trapped Real-Time Evolution of Simple Systems	37
5.2.1	Central Vortex in an Isotropic Potential	37
5.2.2	Offset Vortex in an Anisotropic Potential	40
5.2.3	Vortex Pair Interaction in an Anisotropic Potential	42
5.3	Macroscopic Density Fluctuation in an Isotropic Potential	44
5.4	The Abrikosov Lattice	46
5.5	Trapped Real-Time Evolution of an Abrikosov Lattice	48
5.6	Trapped Real-Time Evolution of Anisotropic Vortex Lattices	48
5.6.1	Vortex Lattice in an Anisotropic Potential	48
5.6.2	Vortex-Antivortex Lattice in an Anisotropic Potential	48
6	Two-Dimensional Expansion Dynamics	53
6.1	The Expanding Coordinate System	53
6.2	Isotropic Central Vortex Free Expansion	56
6.3	Free Expansion of Turbulent Anisotropic Condensates	56
6.4	Condensate Vortex Density Relations	59
6.4.1	Angular Velocity Evolution	59
6.4.2	Vortex Mean Separation Evolution	59
6.4.3	Aspect Ratio Evolution	61
7	Conclusion	63
A	Derivations and Additional Working	65
B	Numerical Methods	73
C	<i>D</i>-Dimensional Bose-Einstein Condensation	75
D	Supplementary Figures	79
	References	103

Preface

The method employed in this thesis is based on a procedure previously used in the Institute for Theoretical Physics, Heidelberg¹ [1]. However, all the numerical results in this report are produced from independently-written source code. My main contributions to this project are:

- *Rewriting the simulation.* I wrote the entire computer simulation from the beginning, rather than using the existing simulation, so as to properly understand the numerical methods and physical concepts. I made sure that the code is implemented in the most efficient way by making use of classes in the C++ library and using header files to break-up the code. As a result, my final code for the simulation is approximately four times shorter than the one previously used.
- *Improving the boundary conditions.* I tested a variety of boundary conditions when carrying out my simulations and subsequently, I chose the ones that most effectively minimised the reflections from the lattice border. These new boundary conditions are a slight improvement on the ones employed in the previous simulation.
- *Generalising the expanding coordinate system derivation.* I generalised the expanding frame derivation for different rates of expansion along each axis. This involved generalising the expansion function to a diagonal expansion matrix to account for the distinct expansion rates of the unit vectors.
- *Writing a vortex detection algorithm.* To extend the current simulation, I also wrote an algorithm that is capable of detecting the locations of distinct quantum vortices at any given time. I designed a density-based procedure and subsequently tested it on a variety of trapped simple systems².
- *Investigating the effect of vortex density on free expansion.* Along with the various turbulent initial states that were considered, the issue of vortex density was examined. For this, I calculated appropriate system parameters to observe the free expansion of comparable turbulent condensates, with a variety of vortex densities.

All the code for this simulation was written in C++ and compiled using the GCC under Debian™ GNU/Linux. All the graphs were plotted with Gnuplot™ 4.4.

The style of this thesis is largely instructive. I intend to go through my work in a logically progressive manner, so that the reader has an insight into how the model developed, as well as the important decisions that were made along the way. I have given sufficient numerical details in the captions, so that all the graphs may be reproduced at a later stage, if desired. I hope you enjoy reading this thesis as much as I have enjoyed writing it.

Bartholomew Andrews

¹This refers to the process of evolving a system into its ground state by imaginary time propagation and then letting it evolve in real time, in an expanding frame.

²The far aim of this algorithm is to be able to measure how the mean separation of the vortices evolves. From this, it would also be possible to measure many other pertinent properties of the system, such as the relationship between the angular velocity of the vortex lattice and the mean separation of the vortices.

A Note on Referencing: Every care and attention was given to referencing and citing all of the appropriate sources used in this thesis. My sincerest apologies go out to anyone that I have accidentally overlooked. Throughout this report, citations are attached as close as possible to the statements to which they refer. References have additionally been given at the end of sections, subsections and paragraphs, where particular sources were used to gain a holistic overview of the corresponding concepts.

A Note on Parameter Values: The parameter values chosen for these simulations are, in the most part, only demonstrative and do not necessarily represent the values that are common in equivalent experiments. However, note that a single parameter alone is often not enough to say whether a system is unrealistic, since the phenomena being studied depend on a relationship between the different values. The major factor behind deciding on which parameters to use, for the following simulations, was computation time. The values were chosen such that the simulations were as fast as possible, whilst, at the same time, clearly demonstrating the important phenomena.

1

Introduction

On 24th July 2009, *Bagnato et al.*, a team of experimental researchers from the University of São Paulo, published a paper on the ‘Emergence of Turbulence in an Oscillating Bose-Einstein Condensate’ [2]. This paper was concerned with the free expansion dynamics of ellipsoidal Bose-Einstein condensates (BECs). In particular, they were investigating the change in aspect ratio of tri-axial ellipsoidal condensates as they expanded¹ (see figure 1.1).

Initially, they created a condensate from a gas of rubidium-87 atoms by trapping and cooling them, using an oscillating magnetic field generated by anti-Helmholtz coils². They subsequently nucleated vortices in the cloud by tilting the axis of the anti-Helmholtz coils relative to the long axis of the BEC (see figure 1.2). Then, they switched off the magnetic field and observed the free expansion of the turbulent condensate.

In these experiments, they observed a marked difference between the free expansion of turbulent and non-turbulent BECs. Ordinarily, when starting with an ellipsoidal condensate, an aspect-ratio inversion during free expansion would be expected, due to the fact that the more tightly confined particles have more energy to transfer. However, the experiments showed that the free expansion of a turbulent BEC was quite different and, in fact, self-similar (see figure 1.3). This means that as a turbulent condensate freely expands, it approximately maintains its original shape.

At the time of the paper’s publication, the cause of this effect was not well understood. However, last year, *Bagnato et al.*, along with American theoretical physicist *A. L. Fetter*, published a follow-up to this paper offering a basic theoretical explanation for this phenomenon [4] (discussed in section 2.5). Yet, the paper makes clear that “a more elaborate numerical simulation of the turbulent regime...will be needed in order to fully account for the experimental observations”. The goal of this project is to provide that simulation.

The process used to simulate the condensates in this report is based on the semi-classical Gross-Pitaevskii model and follows the procedure shown in figure 1.4:

- ① At the beginning, the mean-field condensate wavefunction is initialised. The choice of initialisation at this stage is somewhat arbitrary; however, a Gaussian distribution is used, as it is the limiting distribution for a non-interacting gas cloud. At this stage, we also start *imaginary time propagation* to evolve the system into its ground state (section 4.3). The ground state configuration will naturally depend on the parameters of the harmonic trap.
- ② Near the end of the imaginary time propagation, we induce turbulence into the system by *imprinting phase rotations* into the mean-field wavefunction. These phase rotations subsequently develop into radially symmetric dips in the density, known as *quantum vortices* (section 5.1).

¹In this context, the aspect ratio refers to the ratio between the principle axes of the ellipsoid and thus, it is used to quantify change of shape.

²‘Anti-Helmholtz’ implies that the current in the two coils flows in opposite directions.

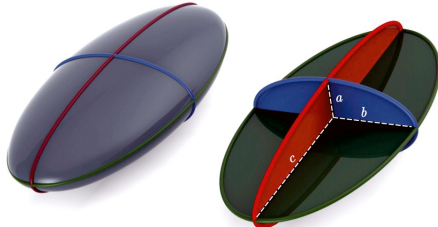


Figure 1.1: A three-dimensional *tri-axial* ellipsoid (*i.e.* $a < b < c$). The diagram on the right shows all three semi-principle axes: the semi-minor axis, a ; the semi-intermediate axis, b and the semi-major axis, c . [3]

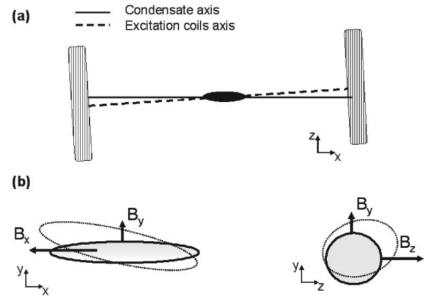


Figure 1.2: Diagrams of the experimental set-up used by *Bagnato et al.*. Diagram (a) shows the configuration used to induce turbulence in the condensate. The cross-sectional view depicts the BEC as the black ellipse in the middle with the two anti-Helmholtz coils at either side. Note that the axis of the excitation coils is tilted relative to the condensate long axis. Diagram (b) shows the predicted deformation oscillation of the condensate due to these disturbances. B_x , B_y and B_z indicate the magnetic field components in the x , y and z -directions, respectively. [2]

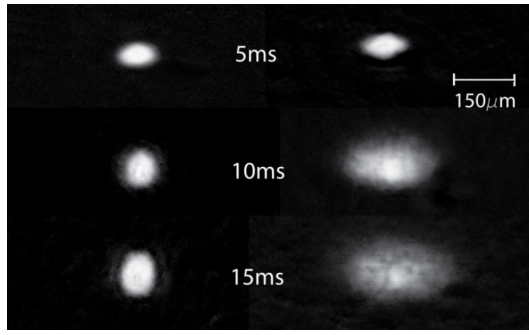


Figure 1.3: Photographs of the observed condensate expansions taken by *Bagnato et al.*. The expansion on the left shows the aspect ratio inversion of a non-turbulent BEC of ^{87}Rb atoms, whereas the self-similar expansion on the right is for the turbulent BEC. The photographs were taken in time steps of 5ms, as indicated in the figure. [2]

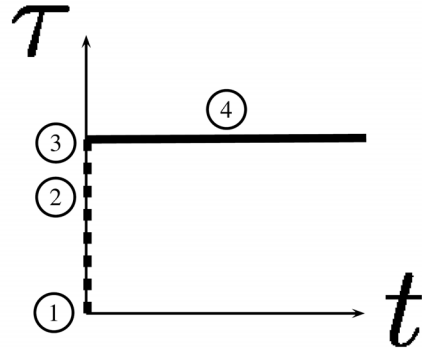


Figure 1.4: Simulation procedure timeline. Since time is generally considered complex in this thesis, the timeline is plotted on an Argand diagram. t and τ are the real and imaginary axes, respectively.

- (3) By this stage, the system should be in its ground state to a very good approximation and the quantum vortices should be fully developed in the density profile. This, therefore, marks the end of the imaginary time propagation. Now, we either keep the trap on and observe the trapped evolution of the turbulent system (chapter 5) or we switch the trap off and observe the free expansion (chapter 6).
- (4) If we leave the trap on and observe the real-time evolution of a trapped condensate, then the region of interest will remain largely confined to the shape of the ground state condensate in stage 3. However, if we are observing the free expansion of a turbulent condensate (particularly an anisotropic one), then the condensate will continuously be spreading and changing shape and so, we will carry out the expansion in an *expanding coordinate system* to reduce computation times (section 6.1).

In this report, we shall start by looking at how general wavefunctions evolve in time by solving the linear Schrödinger equation in chapter 3. Here, we introduce the numerical methods that are used later on and verify that everything is working as it should, by comparing the computed results with the exact solutions. Then, in chapter 4, we look at the imaginary time propagation process (*i.e.* stages $1 \rightarrow 3$ without stage 2) and explain how the system reduces to its ground state. For the chosen parameters, we find that the initial Gaussian density distribution tends to a ‘Thomas-Fermi’ profile. The following chapter focuses on the turbulence induction and quantum vortices (stage 2). This chapter also examines the trapped real-time evolution (stage 4) of a variety of different systems and discusses their real-time dynamics. Last of all, we address the free expansion (stage 4) of a variety of different vortex lattices and look at how the aspect ratio evolves for elliptical turbulent condensates.

2

Theoretical Foundation

Before we embark on simulating turbulent Bose-Einstein condensates, it is important to review the framework and foundation of the physical theory. Doing this not only reminds us of the nature of the physical processes, but it also allows us to find appropriate simulation techniques. There are four main aims of this chapter. First, we shall try to examine the theory of Bose-Einstein condensation from a purely statistical mechanical standpoint. Then, we shall go into the details of the Gross-Pitaevskii theory for an interacting Bose condensate. Third, it is important to study the quantum hydrodynamics and turbulence of the system to learn how vortices form and behave; and finally, we shall look at the theoretical model proposed by *Fetter et al.*, which offers a possible explanation for the self-similar free expansion of turbulent condensates [4]. This chapter should provide the theoretical groundwork needed to begin our computer simulations, as well as the motivation behind them.

2.1 Bose-Einstein Condensation

In 1923, Indian theoretical physicist, Satyendra Nath Bose, submitted a paper to Philosophical Magazine on the statistical description of photons. Unfortunately, this paper was met with scepticism and was refused publication. As a result, Bose sent his paper to Albert Einstein, a respected colleague of his, so that the paper could be translated and published in German. Einstein soon realised the significance of Bose's work and in 1924, subsequently published it in Zeitschrift für Physik, under Bose's name [5]. Not only this, Einstein then went on to extend Bose's model to a gas of non-interacting, massive bosons and he predicted that below a critical temperature, the system would undergo a phase transition and a certain proportion of the atoms would occupy the same quantum state [6] [7]. The implications of generalising Bose's model were profound [8]. However, at that point, the full capabilities of this new unknown state of matter were not properly understood. In the early 20th century, it was not possible to reach the low temperatures required to test this theory. In most cases, the critical temperatures, required to condense a cloud of atoms in this way, are mere fractions of a Kelvin. Consequently, despite many advancements in the field of superfluidity and quantum hydrodynamics, neither Bose nor Einstein lived to see the first experimental realisation of a Bose-Einstein condensate, created in 1995 [9] [10].

2.1.1 Theoretical Prediction

The early 20th century saw many advances in the field of statistical mechanics due to the work of physicists, such as Boltzmann [11] and Fermi [12]. The concept of the Bose-Einstein distribution function representing the mean occupation number for energy levels in a bosonic system was beginning to be developed. The mean occupation number for Bosons, for non-degenerate states, is given by

$$f_{\text{BE}}(E) = \frac{1}{e^{\beta(E-\mu)} - 1}, \quad (2.1)$$

where E is the energy, $\beta \equiv 1/k_B T$ is the inverse temperature and μ is the chemical potential. Normally, with some density of states function, $g(E)$ (see appendix C.1 for derivation), it is possible to determine the total number of particles in the system as

$$N = \int_0^\infty f_{\text{BE}}(E)g(E) dE. \quad (2.2)$$

This is logical, since this simply shows a summation of the number of particles in each energy level over a continuum of levels. In reality of course, the energy levels are not continuous, they are quantized. Physicists were already aware of this when using the density of states approximation and generally, it still gave reasonably accurate results. However, what needed to be addressed was the major flaw in this density of states approximation for the ground state. Since it was only the ground state that was problematic, all the higher energy levels were reasonably accurate in the approximation and a hybrid approach could be taken.

Let us consequently consider the ground state energy, E_0 , separately and the rest of the energy levels as a continuum. Let us also denote the number of particles in the ground state as N_0 . In most cases (including the experiments of *Bagnato et al.*), ultracold particles are confined in electromagnetic harmonic trapping potentials and so, the energy modes of the system are described by the energy levels in the usual parabolic potential well for quantum harmonic oscillators. The energy levels for a typical isotropic three-dimensional case may therefore be given by

$$E_{n_x n_y n_z} = \frac{3}{2}\hbar\omega + (n_x + n_y + n_z)\hbar\omega \quad \forall n_x, n_y, n_z \in \mathbb{N}, \quad (2.3)$$

where $E_0 = E_{000} = 3\hbar\omega/2$ is the zero-point energy, ω is the angular frequency of the oscillator and n_x , n_y and n_z are the principle quantum numbers in the x , y and z -directions, respectively. We may then go on to write the total number of particles as

$$N = N_0 + \int_0^\infty dn_x \int_0^\infty dn_y \int_0^\infty dn_z \frac{1}{\exp(\beta\hbar\omega(n_x + n_y + n_z)) - 1}, \quad (2.4)$$

where the ground state energy of the oscillators has been canceled by the corresponding chemical potential. Note that here we have taken the integrals over the quantum numbers and hence, we do not need to consider the density of states. The density of states approximation is still implied, however, since we are taking integrals over a quantized system. From analysis, we know that the infinite sum of a geometric series may be written as

$$\sum_{k=1}^{\infty} r^{-k} = \frac{1}{r-1} \quad \forall |r| > 1. \quad (2.5)$$

Since temperature and energy can never be negative, $|\exp(\beta\hbar\omega(n_x + n_y + n_z))| > 1$ in all cases and so we may use this result to simplify our equation. Carrying on the calculation, leads to

$$N = N_0 + \sum_{k=1}^{\infty} \int_0^\infty e^{-\beta\hbar\omega n_x k} dn_x \int_0^\infty e^{-\beta\hbar\omega n_y k} dn_y \int_0^\infty e^{-\beta\hbar\omega n_z k} dn_z, \quad (2.6)$$

which after integration reduces to

$$\begin{aligned} N &= N_0 + \sum_{k=1}^{\infty} \left[\frac{e^{-\beta\hbar\omega n_x k}}{-\beta\hbar\omega k} \right]_0^\infty \left[\frac{e^{-\beta\hbar\omega n_y k}}{-\beta\hbar\omega k} \right]_0^\infty \left[\frac{e^{-\beta\hbar\omega n_z k}}{-\beta\hbar\omega k} \right]_0^\infty \\ &= N_0 + \left(\frac{1}{\beta\hbar\omega} \right)^3 \sum_{k=1}^{\infty} \frac{1}{k^3} \\ &= N_0 + \zeta(3) \left(\frac{k_B T}{\hbar\omega} \right)^3. \end{aligned} \quad (2.7)$$

Here, ζ denotes the Riemann zeta function (see equation C.12 for a formal definition). At this point, we should focus our interest on the number of particles in the ground state, N_0 . Specifically, we are interested in how this varies with temperature. Let us now rearrange to arrive at the relation

$$N_0(T) = N \left\{ 1 - \frac{\zeta(3)}{N} \left(\frac{k_B T}{\hbar \omega} \right)^3 \right\}. \quad (2.8)$$

By dimensional analysis, it is clear to see that there is a characteristic temperature for the system, given by

$$T_C \equiv \left(\frac{N}{\zeta(3)} \right)^{1/3} \frac{\hbar \omega}{k_B}, \quad (2.9)$$

which transforms our result into

$$N_0(T) = N \left\{ 1 - \left(\frac{T}{T_C} \right)^3 \right\}$$

(2.10)

This is an extremely important result, as it shows that below some temperature, T_C , a change occurs in our system and the number of the particles in the ground state increases rapidly. In fact, T_C is known as the *critical temperature*¹, this change is known as a *phase transition* and the resulting state of matter is, of course, a Bose-Einstein condensate. It was calculations like these that lead Einstein and many others to believe in this condensed state of matter. Naturally, the consequences of such a phase transition are so unusual that many scientists simply could not accept the idea. According to the theory, if a large fraction of atoms all occupy the same quantum state, then their quantum wavefunctions will superpose and they will start to behave as a macroscopic quantum mechanical state. This implies that quantum effects become visible on the macroscopic scale. Since the field of quantum mechanics was only coming into fruition in the early half of the 20th century, this concept was ahead of its time. Thanks to the work of Landau [13], Lifshitz [14], Feynman [15], Penrose & Onsager [16], and many others, the theory of superfluidity and Bose condensation is now much better understood. [17]

2.1.2 Experimental Observation

Following many advancements made in the field of atomic physics and specifically, in the fields of trapping and cooling, experimental work on Bose-Einstein condensation started, in earnest, in the 1970s. Advanced cooling techniques, such as magneto-optical trapping and laser cooling, were the foundation of many of these experiments. However, despite coming very close, these techniques alone could not quite provide the low temperatures and high densities required for condensation. It was predominantly advancements in evaporative cooling that were responsible for the final temperature reduction². [17] [18]

Using an appropriate combination of the techniques at their disposal, *Cornell, Wiemann et al.*, an experimental team from Boulder, Colorado [9], and *Ketterle et al.*, a team from MIT [10], were the first to experimentally observe Bose-Einstein condensates, in 1995. The three group leaders were subsequently awarded the Nobel Prize in Physics in 2001 “for the achievement of Bose-Einstein condensation in dilute gases of alkali atoms, and for early fundamental studies of the properties of the condensates” [19]. The first condensates were made up of the alkali metals: rubidium-87, sodium-23 and lithium-7, respectively. Alkali metals were chosen, since alkali atoms have an optical transition that can be easily excited by existing lasers and they have a very “favourable internal energy-level structure” for ultracooling [17]. However, since the first condensates in 1995, many other elements have been condensed, such as helium-4 and potassium-41. Many advancements are still being made today and the process is continuously being refined [20]. In 2010, experimental physicists

¹Note that $\omega \rightarrow (\omega_x \omega_y \omega_z)^{1/3}$ in the expression for the critical temperature, for the anisotropic case.

²Evaporative cooling works by selectively removing the high energy particles from the trap, which, in turn, cools the remaining atoms.

from the university of Bonn, Germany, were the first to observe a Bose-Einstein condensate made up of photons [21], as originally predicted by Einstein almost a century ago. Furthermore, attempts are now being made to try and observe condensates at increasingly high temperatures. In the past few years, experimentalists have even managed to increase the critical temperature to the order of 10K, using polaritons [22] [23]. [17]

2.2 The Semi-Classical Gross-Pitaevskii Model

Now that we know some more about the history of condensation, let us turn our attention to a semi-classical model that we can use to simulate this behaviour. The Gross-Pitaevskii model was first introduced by Eugene P. Gross and Lev P. Pitaevskii in 1961 [24] [25]. It is used to study the interactions within a large, weakly-interacting ensemble of bosons in their ground state.

2.2.1 Assumptions and Limitations

First of all, it is important to note the range of applicability of this model, along with its associated equation. Here are some important points to consider:

1. The Gross-Pitaevskii model is only valid for a system of *identical bosons*. In the Gross-Pitaevskii equation (GPE), the mean-field approximation is used in order to describe the many-body quantum wavefunction. Normally, in many-body quantum dynamics, theorists work in a Fock space; a generalisation of Hilbert space to account for many particles³. However, in the GPE, we replace the quantum field with a classical field for the low-temperature approximation and work in a Hilbert space. This is a subtle and highly non-trivial step and is discussed in further detail during the derivation (section 2.2.2). Consequently, the single-particle bosonic wavefunctions need to be as similar as possible for this mean-field approximation to be valid. [17]
2. The model applies only to *dilute gases with simple interactions*. In this context, ‘dilute’ is interchangeable with ‘weakly-interacting’ and means that the scattering length is much smaller than the mean interparticle spacing. In fact, in this model, the contact interactions are treated as Dirac-delta pseudopotentials in position space. They take the form of $g \sum_{i < j} \delta(\mathbf{r}_i - \mathbf{r}'_j)$, where \mathbf{r} and \mathbf{r}' are the positions of any two particles, and g is a constant determined from the scattering length to mass ratio. Consequently, interactions between degrees of freedom corresponding to length scales less than the mean interparticle spacing are not taken into account. This means that the model can only be used to approximate condensation in dilute gases and even then, the approximation simplifies the interactions to point-like potential s-wave scatterings. [18]

Furthermore, the Gross-Pitaevskii *model* is commonly discussed with reference to the Gross-Pitaevskii *equation* (2.21), which imposes two further conditions:

3. The Gross-Pitaevskii equation is only applicable for a *large number of bosons*. As with many equations, large number approximations often simplify the mathematics and usually only introduce insignificant errors into the calculation. The GPE is no exception. Large number approximations are used in the derivation (section 2.2.2) but, in most cases, these introduce negligible errors, when compared to the other approximations on this list. Nevertheless, a condensate with a large number of bosons needs to be used, for this equation to hold true.
4. The equation considers a system at *absolute zero*. As is already well known from the third law of thermodynamics, bringing a system to 0K is fundamentally unobtainable and so from this point alone, we know that the GPE will always be an approximation. The approximation improves, however, the closer a system is brought to zero-temperature. Since the majority of Bose-Einstein condensates are achieved at nano-Kelvin temperatures, this is a reasonable approximation to make. [18]

³Mathematically, a Fock space, \mathcal{F} , is the direct sum of tensor products of copies of a single-particle Hilbert space, \mathcal{H} , and thus, for bosons, may be defined as: $\mathcal{F}(\mathcal{H}) \equiv \bigoplus_{n=0}^{\infty} \mathcal{H}^{\otimes n}$.

2.2.2 The Gross-Pitaevskii Equation

As a starting point for investigating the Gross-Pitaevskii equation, let us consider the model Hamiltonian of the system. The first quantized Hamiltonian for our system of N weakly-interacting, ground state bosons may be written as

$$\hat{H} = \sum_{i=1}^N \left[\frac{\mathbf{p}_i^2}{2m} + V(\mathbf{r}_i) \right] + \frac{g}{2} \sum_{i=1}^N \sum_{j \neq i}^N \delta(\mathbf{r}_i - \mathbf{r}_j), \quad (2.11)$$

where V is an external potential, $g \equiv 4\pi\hbar^2 N a_s / m$ is an interaction constant, a_s is the s-wave scattering length, m is the total mass of the bosons and \mathbf{p}_i is the momentum vector of a particle, i . The term $g\delta(\mathbf{r}_i - \mathbf{r}_j)$ is the internal potential term [18], where \mathbf{r} is a position vector. This is used to model the elastic, ‘hard-sphere’ collisions between any two particles. The factor of a half, in front of the interaction term, is simply there to avoid overcounting the collisions. In this summation, we want to sum the energies of all the collisions between the different particles, hence the $j \neq i$ index. However, these sums alone would count all the collision energies twice, since they would also consider the cases where the i and j indices are swapped.

Although this Hamiltonian is correct, it is not in a useful form for our particular case. This is because it is written using the first quantization formalism. In first quantization, one keeps track of all the particles in a system. However, in our situation, we have N indistinguishable bosons and so it would be superfluous for us to keep track of every particle. After all, knowing the position and momentum of one particular particle is useless, since there is no possible way of identifying it. Therefore, we now switch to a second quantization formalism. In second quantization, we consider the bosonic quantum field. Instead of summing over all the particles in our Hamiltonian, as before, we will now take complete spatial integrals over this field [26].

Let us define a Bose field annihilation operator, $\hat{\Psi}(\mathbf{r}, t)$, with a corresponding Hermitian conjugate creation operator $\hat{\Psi}^\dagger(\mathbf{r}, t)$. The time dependence of these operators is not relevant for this derivation and so, it is dropped. Using this many-body quantum field approach, we may now express our Hamiltonian as

$$\hat{H} = \int d\mathbf{r} \hat{\Psi}^\dagger(\mathbf{r}) \left[\frac{\hat{p}^2}{2m} + \hat{V} \right] \hat{\Psi}(\mathbf{r}) + \frac{g}{2} \int d\mathbf{r} \int d\mathbf{r}' \hat{\Psi}^\dagger(\mathbf{r}) \hat{\Psi}^\dagger(\mathbf{r}') \delta(\mathbf{r} - \mathbf{r}') \hat{\Psi}(\mathbf{r}) \hat{\Psi}(\mathbf{r}'). \quad (2.12)$$

Here, $\hat{p} = -i\hbar\nabla$ and \hat{V} are our momentum and external potential operators, respectively. Note that because of our Dirac-delta pseudopotentials, the \mathbf{r}' -dependence will conveniently integrate out [17]. Before we continue, however, let us denote the operator in square brackets as \hat{H}_0 to simplify our calculations. Now, integrating over all \mathbf{r}' -space leads to

$$\hat{H} = \int d\mathbf{r} \hat{\Psi}^\dagger(\mathbf{r}) \hat{H}_0 \hat{\Psi}(\mathbf{r}) + \frac{g}{2} \int d\mathbf{r} \hat{\Psi}^\dagger(\mathbf{r}) \hat{\Psi}^\dagger(\mathbf{r}) \hat{\Psi}(\mathbf{r}) \hat{\Psi}(\mathbf{r}). \quad (2.13)$$

This is a relatively simple form of our Hamiltonian that we can now use. From quantum theory, we know that Heisenberg’s time evolution equation states that

$$i\hbar \frac{\partial \hat{\Psi}(\mathbf{r}')}{\partial t} = [\hat{\Psi}(\mathbf{r}'), \hat{H}]. \quad (2.14)$$

If we now evaluate the commutator in this equation, for our particular Hamiltonian, then we arrive at

$$i\hbar \frac{\partial \hat{\Psi}(\mathbf{r}')}{\partial t} = \hat{\Psi}(\mathbf{r}') \hat{H} - \int d\mathbf{r} \hat{\Psi}^\dagger(\mathbf{r}) \hat{H}_0 \hat{\Psi}(\mathbf{r}) \hat{\Psi}(\mathbf{r}') - \frac{g}{2} \int d\mathbf{r} \hat{\Psi}^\dagger(\mathbf{r}) \hat{\Psi}^\dagger(\mathbf{r}) \hat{\Psi}(\mathbf{r}) \hat{\Psi}(\mathbf{r}) \hat{\Psi}(\mathbf{r}'). \quad (2.15)$$

From quantum field theory, we know that the bosonic field commutator relations [17] are given by:

$$[\hat{\Psi}(\mathbf{r}'), \hat{\Psi}^\dagger(\mathbf{r})] = \delta(\mathbf{r}' - \mathbf{r}) \quad \text{and} \quad [\hat{\Psi}(\mathbf{r}'), \hat{\Psi}(\mathbf{r})] = [\hat{\Psi}^\dagger(\mathbf{r}'), \hat{\Psi}^\dagger(\mathbf{r})] = 0. \quad (2.16)$$

Using these relations, we can now expand out our calculation. Let us define our field operator, $\hat{\Psi}(\mathbf{r}') \equiv \hat{\Psi}'$, from this point on, to make the working clearer. Continuing the commutator expansion leads to

$$\begin{aligned} i\hbar \frac{\partial \hat{\Psi}'}{\partial t} &= \hat{\Psi}' \hat{H} - \int d\mathbf{r} [\hat{\Psi}' \hat{\Psi}^\dagger - \hat{\Psi}' \hat{\Psi}^\dagger + \hat{\Psi}^\dagger \hat{\Psi}'] \hat{H}_0 \hat{\Psi} \\ &\quad - \frac{g}{2} \int d\mathbf{r} [\hat{\Psi}' \hat{\Psi}^\dagger - 2\hat{\Psi}' \hat{\Psi}^\dagger + 2\hat{\Psi}^\dagger \hat{\Psi}'] \hat{\Psi}^\dagger \hat{\Psi} \hat{\Psi}. \end{aligned} \quad (2.17)$$

Here we have simply introduced some extra terms, so that we can apply our Bose commutator relations. Identifying the commutators yields

$$i\hbar \frac{\partial \hat{\Psi}'}{\partial t} = \hat{\Psi}' \hat{H} - \int d\mathbf{r} [\hat{\Psi}' \hat{\Psi}^\dagger - [\hat{\Psi}', \hat{\Psi}^\dagger]] \hat{H}_0 \hat{\Psi} - \frac{g}{2} \int d\mathbf{r} [\hat{\Psi}' \hat{\Psi}^\dagger - 2[\hat{\Psi}', \hat{\Psi}^\dagger]] \hat{\Psi}^\dagger \hat{\Psi} \hat{\Psi}, \quad (2.18)$$

which after the substitution, leaves us with

$$i\hbar \frac{\partial \hat{\Psi}'}{\partial t} = \hat{\Psi}' \hat{H} - \int d\mathbf{r} [\hat{\Psi}' \hat{\Psi}^\dagger - \delta(\mathbf{r}' - \mathbf{r})] \hat{H}_0 \hat{\Psi} - \frac{g}{2} \int d\mathbf{r} [\hat{\Psi}' \hat{\Psi}^\dagger - 2\delta(\mathbf{r}' - \mathbf{r})] \hat{\Psi}^\dagger \hat{\Psi} \hat{\Psi}. \quad (2.19)$$

Note that we can now integrate out the \mathbf{r} -dependence to arrive at

$$i\hbar \frac{\partial \hat{\Psi}'}{\partial t} = [\hat{H}_0 + g\hat{\Psi}'^\dagger \hat{\Psi}'] \hat{\Psi}'. \quad (2.20)$$

At this point, we can use the fact that a Bose condensate is simply a macroscopic occupation of the lowest quantum state and so, we can apply our mean-field approximation and define a mean-field term, $\Psi(\mathbf{r}') \equiv \langle \hat{\Psi}(\mathbf{r}') \rangle$. “By assuming that the function Ψ varies slowly on distances of the order of the range of the interatomic force”, we can move from \mathbf{r}' to \mathbf{r} in the arguments of Ψ [17]. If we now only take the leading order terms in $\hat{\Psi}'$ and drop the dashes, then we finally arrive at the time-dependent Gross-Pitaevskii equation,

$$i\hbar \frac{\partial \Psi}{\partial t} = \left(-\frac{\hbar^2}{2m} \nabla^2 + V + g|\Psi|^2 \right) \Psi \quad (2.21)$$

In this approximation, we may consider Ψ as a many-particle ‘wavefunction’⁴ that is related to the single-particle wavefunction, ψ , through the relation $\Psi = \sqrt{N}\psi$. This implies that the normalisation conditions may be given by $\langle \psi | \psi \rangle = 1$ and $\langle \Psi | \Psi \rangle = N$. [27]

Naturally, there are many different derivations of the Gross-Pitaevskii equation. For example, it is very common to take the Hartree-Fock product wavefunction approximation, find the expectation value of the energy and then use Lagrange multipliers to minimise the free energy, to show the equation [28]. Alternatively, one could start with the action of the system and then use Hamilton’s stationarity condition to arrive at the result [17]. These are the two main alternatives that are commonly used but many others exist. The field theory approach was taken here to show how naturally the equation arises from a many-body bosonic system. [29]

Note that the Gross-Pitaevskii equation is a 2nd-order, non-linear partial differential equation and so in general, no exact solutions exist. There are certain one-dimensional cases that do yield exact solutions, however these are beyond the scope of this thesis [30].

⁴Strictly speaking, Ψ in the Gross-Pitaevskii equation is not a quantum wavefunction but rather, the expectation value of the field operator with respect to the wavefunction. For the purposes of this thesis, let us adopt definition (2.22) and refer to the result, loosely, as the many-body ‘wavefunction’, whilst bearing in mind the derivation given in this section.

2.3 Hydrodynamic Formulation and Topological Defects

In the previous section, we derived an important equation that can be used to model the behaviour of a Bose-Einstein condensate under the conditions specified in section 2.2.1. Let us now look at the meaning and implications of this equation in more detail.

Let us start by defining our condensate wavefunction as

$$\Psi(\mathbf{r}, t) \equiv \sqrt{\rho(\mathbf{r}, t)} e^{i\phi(\mathbf{r}, t)} \equiv |\Psi| e^{i\phi}, \quad (2.22)$$

where ρ denotes the particle density and ϕ denotes the phase. We can now multiply the GPE by Ψ^* and then subtract the complex conjugate of the result, to arrive at an expression that has the form of the hydrodynamic continuity equation for the particle density [17],

$$\frac{\partial \rho}{\partial t} + \nabla \cdot \mathbf{j} = 0, \quad (2.23)$$

where the current density, \mathbf{j} , is given by

$$\mathbf{j}(\mathbf{r}, t) = -\frac{i\hbar}{2m} (\Psi^* \nabla \Psi - \Psi \nabla \Psi^*) = \rho \frac{\hbar}{m} \nabla \phi. \quad (2.24)$$

From the hydrodynamic relation $\mathbf{j} = \rho \mathbf{v}$, we know that this implies that the velocity of the condensate is proportional to the phase gradient (see appendix A.1 for derivation):

$$\mathbf{v} = \frac{\hbar}{m} \nabla \phi. \quad (2.25)$$

When the condensate is brought into the turbulent regime, topological defects, such as solitons and vortices, emerge in the density profile. Quantum vortices are quantized rotations in the probability density that arise due to the principle of orbital angular momentum conservation. It is important to note now that quantum vortices only occur in *superfluids*. Superfluids are fluids with zero viscosity and so the particles within the fluid all flow together. This implies that superfluids are also irrotational [31]. A Bose-Einstein condensate, on the other hand, is (loosely) defined as a system in which a large fraction of the particles all occupy the lowest quantum state. It is important to note the distinction between these two phenomena, despite the fact that they often occur together. For the purposes of this thesis, we will be modeling a superfluid condensate, as used by *Bagnato et al.* in their experiments.

Now, since the curl of the phase gradient is trivially zero for superfluids, we also know, from equation (2.25), that this implies that the curl of the velocity is zero,

$$\nabla \times \mathbf{v} = \mathbf{0}. \quad (2.26)$$

This mathematically describes the irrotational nature of superfluids. Note that equations (2.25) and (2.26) only apply if ϕ is non-singular [17]. This normally holds true for a superfluid condensate. However, if turbulence is induced in the superfluid and vortices arise, then these equations will not hold true for the vortex cores (see chapter 5).

As mentioned before, the turbulent regime of a superfluid is very different from normal. For example, if a cylindrical container of an ordinary fluid is rotated about the radial symmetry axis, then the fluid would rotate, so as to conserve angular momentum. However, in the case of superfluids, they are irrotational and so would not rotate in this way. Instead, a regular array of quantum vortices would develop on the surface. Furthermore, since the superfluid is irrotational, the possible rotations of these vortices are very restricted. We know that the condensate wavefunction must be single-valued and that there are singularities in the phase at the vortex cores. From the residue theorem, we know that for a closed contour around a vortex, \mathbf{l} , the sum of the phase gradients must be a multiple of 2π , in that

$$\oint \nabla \phi \cdot d\mathbf{l} = 2\pi l \quad \forall l \in \mathbb{Z}. \quad (2.27)$$

Furthermore, from equation (2.25), we know that the *circulation*, Γ , around this contour is given by

$$\Gamma = \oint \mathbf{v} \cdot d\mathbf{l} = \frac{\hbar}{m} 2\pi l = \frac{\hbar}{m} l \quad \forall l \in \mathbb{Z}. \quad (2.28)$$

This shows that the circulation around the vortex line is quantized into multiples of \hbar/m . Note also that, as with most quantum concepts, the Ehrenfest theorem may be applied. For example, if the piece-wise average rotation was taken for a large array of quantum vortices, then the result for the whole condensate would approximate that of classical fluid, $\mathbf{v} = \boldsymbol{\Omega} \times \mathbf{r}$, where $\boldsymbol{\Omega}$ is the macroscopic angular velocity pseudovector and \mathbf{r} is the displacement from the origin of rotation. The concept of quantized vortical flow in the context of superfluids was first proposed by Lars Onsager in 1949 [32]. This was later expanded upon by Richard Feynman in 1955 [15]. [17] [33]

2.4 Modelling Condensates using Gross-Pitaevskii Theory

Let us now briefly discuss how the Gross-Pitaevskii theory applies to static and expanding condensates, as well as the implications for the energy distribution.

2.4.1 Static Condensates

The action for an interacting Bose-fluid for a normalised mean-field wavefunction, Ψ , is given by

$$\mathcal{S} = \iint \mathcal{L} d\mathbf{r} dt = \frac{i\hbar}{2} \iint \left(\Psi^* \frac{\partial \Psi}{\partial t} - \Psi \frac{\partial \Psi^*}{\partial t} \right) d\mathbf{r} dt - \int E dt, \quad (2.29)$$

where the integration is assumed to be across the complete space-time. Here, \mathcal{L} is the interacting Bose-fluid Lagrangian functional and E is the energy functional of the system given by

$$E[\Psi] = \int \left(\frac{\hbar^2}{2m} |\nabla \Psi|^2 + V(\mathbf{r}) |\Psi|^2 + \frac{g}{2} |\Psi|^4 \right) d\mathbf{r}, \quad (2.30)$$

where V is an arbitrary external potential function [34]. The static Bose condensate is described by solutions to the time-independent GPE:

$$\left[-\frac{\hbar^2}{2m} \nabla^2 + V(\mathbf{r}) + g|\Psi(\mathbf{r})|^2 - \mu \right] \Psi(\mathbf{r}) = 0, \quad (2.31)$$

where μ is the eigenenergy of the condensate and to a very good approximation equal to the chemical potential, $\partial E / \partial N$. Let us start by considering the case of a spherical harmonic trap of the form,

$$V(\mathbf{r}) = \frac{1}{2} m\omega r^2, \quad (2.32)$$

in spherical polars, with a characteristic oscillator length given by $a_{\text{osc}} = \sqrt{\hbar/m\omega}$. Let the size of the trapped cloud be given by an approximate radius, R . The different contributions to the mean-field energy per particle are then:

$$E_{\text{kin}} \sim \frac{\hbar^2}{2mR^2}, \quad E_{\text{pot}} \sim \frac{1}{2} m\omega^2 R^2, \quad E_{\text{int}} \sim \frac{gN}{R^3}, \quad (2.33)$$

where E_{kin} , E_{pot} and E_{int} are the kinetic, potential and interaction energies of the particles, respectively. A variational estimate shows that in equilibrium E_{pot} and E_{int} approximately balance each other, which yields

$$R \sim \beta a_{\text{osc}} \quad \text{with} \quad \beta \equiv (Na_s/a_{\text{osc}})^{1/5}. \quad (2.34)$$

Here, β is a parameter that characterises the interactions of the atoms, which play a significant role if $\beta^5 \gg 1$. Consequently, it is clear to see that the kinetic energy only represents a small fraction of

the total energy when β^5 is large:

$$E_{\text{kin}} \sim \beta^{-4}(E_{\text{pot}} + E_{\text{int}}). \quad (2.35)$$

This leads us to the *Thomas-Fermi approximation* (see chapter 4), where the kinetic energy term in the stationary GPE (2.31) is neglected. For the case of the harmonic trap, this implies that the density distribution tends to a paraboloid, such that

$$\rho_{\text{TF}} = \frac{\mu - V(\mathbf{r})}{g} \quad \text{for} \quad V < \mu \quad \text{and} \quad g > 0. \quad (2.36)$$

The radius of the Thomas-Fermi cloud, R_{TF} , is defined as the distance from the origin to the density zero and is given by

$$R_{\text{TF}} = \sqrt{2\mu/m\omega^2} = \sqrt{2\mu/\hbar\omega a_{\text{osc}}}. \quad (2.37)$$

Now, integrating the density distribution over all $\mathbf{r} : |\mathbf{r}| \leq R_{\text{TF}}$ and using the condensate wavefunction normalisation condition, $\langle \Psi | \Psi \rangle = N$, leads to an expression for μ in terms of the parameter β and the trap frequency ω (as shown in chapter 4). The Thomas-Fermi radius subsequently becomes

$$R_{\text{TF}} = 15^{1/5} \beta a_{\text{osc}}, \quad (2.38)$$

which shows that the ground state cloud radius for interacting atoms is several times larger than the equivalent radius for non-interacting particles. [18] [17]

2.4.2 Expanding Condensates

Let us investigate the expanding case by starting with a general Gaussian wavefunction, which is both normalised and isotropic:

$$\Psi(\mathbf{r}) \propto \sqrt{\frac{N}{R^3}} e^{-r^2/2R^2} e^{i\phi(r)}, \quad (2.39)$$

where the now non-constant $\phi(r)$ allows us to describe a particle flow⁵.

The mean-field energy functional (2.30) now splits into a zero-point energy term, E_{zero} , and a particle flow term, E_{flow} :

$$E[\Psi] = \underbrace{\frac{\hbar^2}{2m} \int d\mathbf{r} \left(\frac{d|\Psi(\mathbf{r})|^2}{dr} \right)^2}_{E_{\text{zero}}[\Psi]} + \underbrace{\frac{\hbar^2}{2m} \int d\mathbf{r} |\Psi(\mathbf{r})|^2 (\nabla \phi)^2}_{E_{\text{flow}}[\Psi]}. \quad (2.40)$$

After the insertion of our trial wavefunction (2.39) we can deduce that

$$E_{\text{zero}} = \frac{3\hbar^2 N}{4mR^2}, \quad E_{\text{flow}} = \frac{3mN}{4} \dot{R}^2, \quad E_{\text{int}} = \frac{N^2 g}{2(2\pi)^{3/2} R^3}. \quad (2.41)$$

Now suppose that the condensate is static, $\dot{R} = 0$, until $t = t_0$, when the trap is suddenly switched off. Energy conservation then leads to the dynamic differential equation,

$$\dot{R}^2 = \frac{\hbar^2}{m^2} \left(\frac{1}{R^2(0)} - \frac{1}{R^2} \right) + \frac{2Ng}{3(2\pi)^{3/2} m} \left(\frac{1}{R^3(0)} - \frac{1}{R^3} \right), \quad (2.42)$$

which redistributes the interaction and zero-point energies. For the $g = 0$ case, this integrates to

$$R(t) = \sqrt{R^2(0) + (v_0 t)^2} \quad \text{with} \quad v_0 = \hbar/mR(0). \quad (2.43)$$

The expansion therefore reflects the Heisenberg uncertainty of the condensate atoms' location.

⁵The trial wavefunction is chosen so as to simplify the resulting relations.

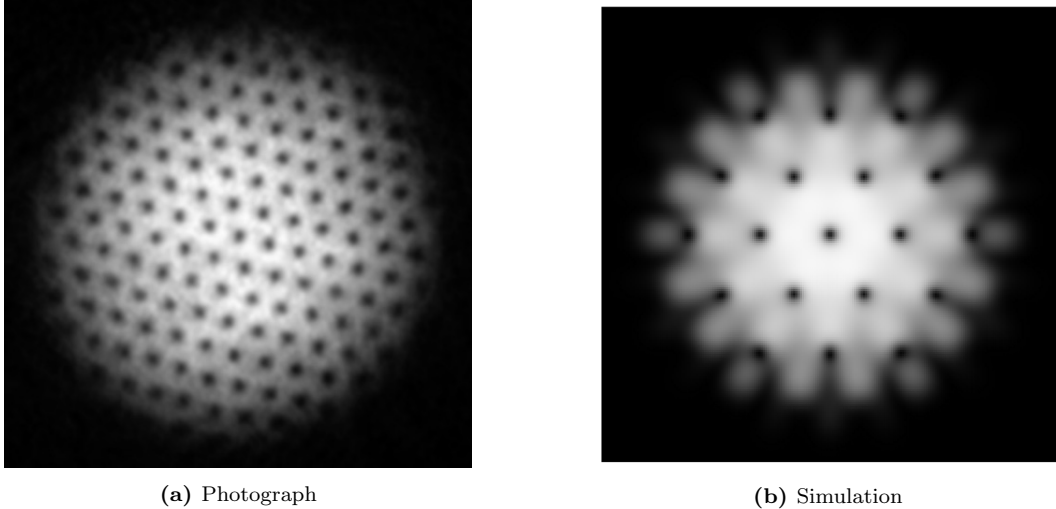


Figure 2.1: (a) Photograph of a laser-cooled, superfluid Bose-Einstein condensate of sodium atoms in the turbulent regime. [35] (b) Simulation of an Abrikosov lattice of 61 identical quantum vortices in an approximately Thomas-Fermi, turbulent BEC. $\{t = 0[\text{d.u.}], g = 1[\text{d.u.}], \omega_x = \omega_y = 100[\text{d.u.}], N = 1000\}$ (see table 4.1) (a,b) The light areas show the atoms and the dark spots indicate the quantized vortices.

Furthermore, in this case, we know that $R(0) = a_{\text{osc}}$ and so

$$R(t) = R(0)\sqrt{1 + \omega^2 t^2}. \quad (2.44)$$

This reproduces the standard dispersion of a Gaussian wavepacket (see chapter 3). [18] [17]

2.5 Aspect Ratio Evolution in Turbulent Condensates

Now that we know the fundamentals of quantum vortices in superfluid condensates, as well as a theoretical model that we can use to simulate their behaviour, let us turn our attention to the problem at hand. The aim of this thesis is to study the aspect ratio evolution of ellipsoidal turbulent superfluid condensates during free expansion. Due to the very nature of vortex quantization, quantum turbulence arises as a neat array of vortex lines. This is very convenient for computer simulations, since, at least at the beginning, the vortices have clear positions in space (see figure 2.1a). The experimental results of *Bagnato et al.* were surprising in many ways, not least because they found that turbulent ellipsoidal condensates undergo self-similar free expansion [2]. This result was particularly exciting at the time because the effect of quantum vortices on the free expansion of condensate clouds had not been studied in great detail. In 2012, *Fetter et al.* published a simple theoretical explanation [4]. In this section, we shall go through the simple theory that was proposed in order to try and explain this strange phenomenon.

To begin, let us consider the hydrodynamics of a superfluid. From the Gross-Pitaevskii equation, we can arrive at two fundamental hydrodynamic equations, namely the continuity equation (2.23) and Euler's equation for a perfect inviscid fluid,

$$m \frac{\partial \mathbf{v}}{\partial t} + \nabla \left[\frac{1}{2} m v^2 + V + g\rho \right] = m \mathbf{v} \times (\nabla \times \mathbf{v}). \quad (2.45)$$

Typically for superfluids, these equations are reduced to forms for irrotational flow and so, the right-hand side of equation (2.45) goes to zero. In this case, the pair of equations can successfully describe the oscillations in superfluid condensates. However, in our case, we are specifically focusing on the effect that the vortices have on the condensate as a whole, and so we cannot neglect turbulence

effects. Therefore, we cannot set the right-hand side of equation (2.45) to zero. Instead, we note that for a large array of vortices, the curl of the velocity field may be expressed as $\nabla \times \mathbf{v} = 2\boldsymbol{\Omega}$, where $\mathbf{v} = \mathbf{v}_I + \mathbf{v}_R$. Here, \mathbf{v}_I is used to denote the irrotational velocity component and $\mathbf{v}_R = \boldsymbol{\Omega} \times \mathbf{r}$, the standard rotational one.

This theoretical model neglects the interactions between vortices and only focuses on the ‘‘macroscopic effect of the rotation in each direction’’. Furthermore, no ‘‘decay mechanism’’ for the vortices is considered during the free expansion [4]. This is a reasonable simplification, since the decrease in density after the magnetic trap is turned off considerably reduces the chances of these phenomena. Finally, the theory implicitly uses the Thomas-Fermi approximation (see chapter 4) and so the interaction energy dominates over the kinetic energy.

From the Thomas-Fermi approximation, we can express the particle density distribution, ρ , as

$$\rho(\mathbf{r}, t) = \rho_0(t) \left(1 - \frac{x^2}{R_x^2(t)} - \frac{y^2}{R_y^2(t)} - \frac{z^2}{R_z^2(t)} \right), \quad (2.46)$$

where

$$\rho_0(t) = \frac{15N}{8\pi} \frac{1}{R_x(t)R_y(t)R_z(t)}. \quad (2.47)$$

Now, extending our previous concept of the two-component velocity field, we may write

$$\mathbf{v}(\mathbf{r}, t) = \underbrace{\frac{1}{2} \nabla(b_x(t)x^2 + b_y(t)y^2 + b_z(t)z^2)}_{\mathbf{v}_I} + \underbrace{\boldsymbol{\Omega}(t) \times \mathbf{r}}_{\mathbf{v}_R}, \quad (2.48)$$

where $b_i(t)$ are unknown coefficients to be determined.

Let us now consider the case where the vortex array is perpendicular to the symmetry axis of the trap (let this be the x -axis). This is fairly representative of what is seen in the laboratory, since vortices usually form along the plane perpendicular to the axis of rotation, where the trap potential is asymmetrical. Due to the asymmetry of the trap in this region, we shall add an additional irrotational term to the velocity field to produce an ‘‘initially stable configuration’’ [4] so that

$$\mathbf{v}(\mathbf{r}, t) = \frac{1}{2} \nabla(b_x(t)x^2 + b_y(t)y^2 + b_z(t)z^2) + \boldsymbol{\Omega}(t) \times \mathbf{r} + \alpha(t) \nabla(yz), \quad (2.49)$$

where $\alpha(t)$ is also an unknown coefficient to be determined. Now substituting our equation for the velocity field (2.49) and the density (2.46) into the continuity equation (2.23), we arrive at the following relations for our unknown coefficients and macroscopic angular velocity, for a given number of vortices, N_V :

$$b_i(t) = \frac{\dot{R}_i(t)}{R_i(t)}, \quad \Omega(t) = \frac{\hbar}{m} \frac{N_V}{R_y(t)R_z(t)}, \quad \alpha(t) = \frac{R_y^2(t) - R_z^2(t)}{R_y^2(t) + R_z^2(t)} \Omega(t), \quad (2.50)$$

where $i \in \{x, y, z\}$. As a final step, if we now substitute these relations into Euler’s hydrodynamic equation (2.45), then we arrive at the set of dynamic equations that describe the evolution of each of the three principle radii of the ellipsoid and implicitly, the aspect ratios:

$$\begin{aligned} \ddot{R}_x - \frac{15N\hbar^2 a_s}{m^2} \frac{1}{R_x^2 R_y R_z} &= 0, \\ \ddot{R}_y - \frac{15N\hbar^2 a_s}{m^2} \frac{1}{R_y^2 R_x R_z} &= 4 \left(\frac{N_V \hbar}{m} \right)^2 \frac{1}{(R_y^2 + R_z^2)^2} R_y, \\ \ddot{R}_z - \frac{15N\hbar^2 a_s}{m^2} \frac{1}{R_z^2 R_x R_y} &= 4 \left(\frac{N_V \hbar}{m} \right)^2 \frac{1}{(R_y^2 + R_z^2)^2} R_z. \end{aligned} \quad (2.51)$$

Here, we have used the Feynman expression for the angular velocity, $\Omega = \pi\hbar\rho_V/m$, with the areal

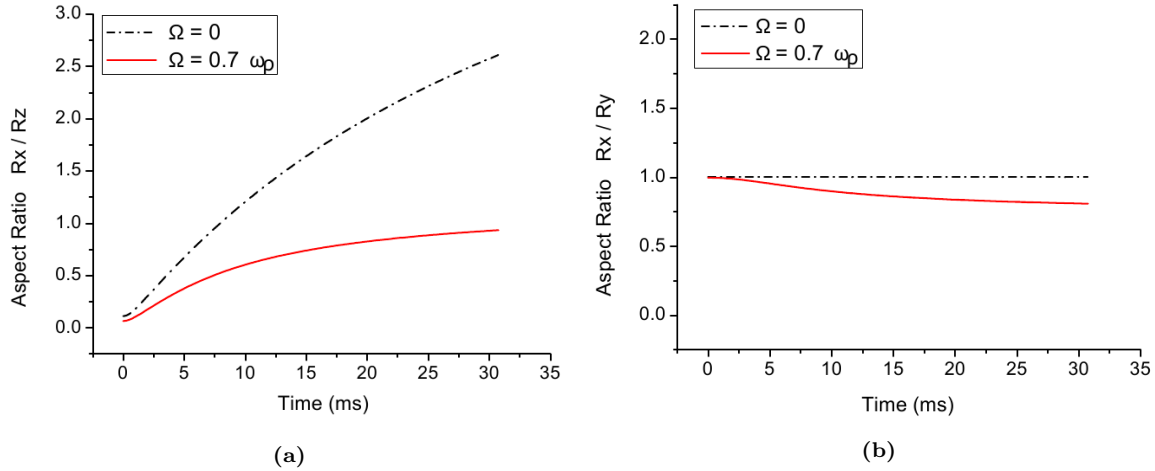


Figure 2.2: Theoretical aspect ratio evolution during free expansion, for non-turbulent and turbulent BECs with the vorticity angular momentum vector directed along the x -axis (perpendicular to the long axis of the condensate). The initial parameters were chosen such that $\omega_\rho = \omega_x = \omega_y$ and so, the semi-minor axis and the semi-major axis are equal at $t = 0$. Graph (a) shows the evolution of the elliptical ratio, R_x/R_z , whereas graph (b) shows the evolution of the circular ratio, R_x/R_y . [4]

vortex density, $\rho_V = N_V/A_{\perp}$, being defined as the vortex number per condensate-area perpendicular to the vortex lines. These equations reproduce the findings of *Bagnato et al.* in that they predict the ‘non-inversion’ of the aspect ratio in these ellipsoidal clouds. Figure 2.2 shows the plotted solutions to these equations, from the *Fetter et al.* paper [4]. Figure 2.2a demonstrates the elliptical ratio inversion along with the turbulent non-inversion, given by the dashed and solid lines, respectively. As shown in figure 2.2b, the circular ratio remains approximately constant. In addition to this, *Fetter et al.* also derived the relations for the case where the vortex array is parallel to the long axis⁶ [4]. In this scenario, the elliptical aspect ratio of the cloud would invert, however the inversion would be at a much slower rate than normal and so may not be easily noticed at experimental time scales. In any case, it is very important to take the vortical rotations into account when calculating the hydrodynamics of turbulent superfluids. This theory is, of course, relatively new and it is limited to the assumptions mentioned earlier. The aim now is to construct computer simulations of turbulent superfluid condensates, in order to see if the results of *Bagnato et al.* may be reproduced and the simple theory of *Fetter et al.*, vindicated. [4] [36]

⁶Note that this is not the preferred direction of the vortex lines in experiments and so is not discussed at length.

3

Solving the Linear Schrödinger Equation

The first step on the road to simulating turbulent BECs is computing how quantum wavefunctions evolve with time. The simplest possible start is to solve the time-dependent Schrödinger equation (TDSE) for a free wavefunction. The aim of this chapter is to quickly review the pertinent concepts of quantum mechanics and to introduce, in the simplest way, many of the numerical methods that are employed later on.

Let us start by reviewing the properties of the Schrödinger equation. In a coordinate-free representation, the TDSE may be expressed as

$$\hat{H}|\psi\rangle = i\hbar \frac{\partial}{\partial t}|\psi\rangle, \quad (3.1)$$

where ψ is a single-particle wavefunction in Hilbert space and the Hamiltonian operator, \hat{H} , is given by

$$\hat{H} = \hat{T} + \hat{V} = \frac{\hat{p}^2}{2m} + \hat{V} = -\frac{\hbar^2}{2m}\nabla^2 + \hat{V}, \quad (3.2)$$

where \hat{T} , \hat{V} and $\hat{p} = -i\hbar\nabla$ are the kinetic energy, potential and momentum operators, respectively. Here we have implied a real space basis, such that $\psi \equiv \psi(\mathbf{r}, t)$, where \mathbf{r} is an arbitrary-dimensional position vector. Now, for a free wavefunction, there is no potential term and so the TDSE reduces to

$$\frac{\partial\psi}{\partial t} = \frac{i\hbar}{2m}\nabla^2\psi. \quad (3.3)$$

This is a 2nd-order linear partial differential equation with both temporal and spatial derivatives. Due to the equation's linearity, analytic solutions generally exist. It consequently serves as a good testing ground for computational methods because most results can be verified algebraically.

3.1 The One-Dimensional Free TDSE

In the one-dimensional case, equation (3.3) reduces to

$$\frac{\partial}{\partial t}\psi(x, t) = \frac{i\hbar}{2m}\frac{\partial^2}{\partial x^2}\psi(x, t) \quad \Rightarrow \quad \dot{\psi} = \frac{i\hbar}{2m}\psi''. \quad (3.4)$$

In this section, the time evolution of a wavepacket will be computed in accordance with this equation.

3.1.1 The Gaussian Wavepacket

For our initial wavefunction, let us start with a Gaussian form. This will indeed be the most realistic start for a non-interacting gas, as we will see when we come to condensate simulations. However,

before we go on, it is important to justify our choice in this context. The special feature of a Gaussian wavepacket is that it is a *minimum uncertainty state*. This means that it fulfills the equality in Heisenberg's uncertainty relation, which for position and momentum may be expressed as

$$\Delta x \Delta p \geq \frac{\hbar}{2}. \quad (3.5)$$

This is easy to verify. For example, if we start with a simple normalised Gaussian wavefunction,

$$\psi(x) = \left(\frac{2}{\pi}\right)^{\frac{1}{4}} e^{-x^2}, \quad (3.6)$$

then it does not take long to analytically calculate the rms uncertainties. The mean-squared uncertainty in position is given by $(\Delta x)^2 = \langle x^2 \rangle - \langle x \rangle^2 = 1/4$ and the mean-squared uncertainty in momentum is $(\Delta p)^2 = \langle p^2 \rangle - \langle p \rangle^2 = \hbar^2$ (see appendix A.3 for a full derivation). Hence,

$$\Delta x \Delta p = \frac{\hbar}{2}. \quad (3.7)$$

This result holds true for *any* Gaussian wavepacket and is the reason why Gaussian wavepackets spread over time (as discussed in section 3.1.5). This makes them an ideal starting choice for our wavefunction¹.

3.1.2 Dimensionless Form for the One-Dimensional Case

Since it is only the *form* of the evolved wavefunction that is under consideration, the equations in these simulations may be made dimensionless to compute the evolution.

Let us start by making the length quantity, x , dimensionless by expressing it in terms of a characteristic length, the lattice constant, a :

$$\bar{x} \equiv \frac{x}{a}. \quad (3.8)$$

Following on from this, we can make all of the physical terms in equation (3.4) dimensionless. From the normalisation condition,

$$\int_{-\infty}^{\infty} \psi \psi^* dx = 1, \quad (3.9)$$

we know that since the dimension of the differential element, dx , is length, then the dimension of the wavefunction, ψ , must be the inverse square root of length. This means that we can make ψ dimensionless by multiplying it by the positive square root of length (*i.e.* \sqrt{a}). Therefore, we impose that

$$\bar{\psi} \equiv \sqrt{a} \psi. \quad (3.10)$$

We can now substitute relations (3.8) and (3.10) into equation (3.4) to arrive at

$$\frac{\partial}{\partial t} \frac{\bar{\psi}}{\sqrt{a}} = \frac{i\hbar}{2ma^2} \frac{\partial^2}{\partial \bar{x}^2} \frac{\bar{\psi}}{\sqrt{a}}, \quad (3.11)$$

which after some cancellation and rearrangement leads to the result:

$$\frac{\partial \bar{\psi}}{\partial t} \left(\frac{ma^2}{\hbar} \right) = \frac{i}{2} \frac{\partial^2 \bar{\psi}}{\partial \bar{x}^2}. \quad (3.12)$$

Now, by choosing an appropriate definition for dimensionless time, such as

$$\bar{t} \equiv \frac{\hbar}{ma^2} t, \quad (3.13)$$

¹A Gaussian distribution is also the limiting case of a general linear TDSE.

we can rewrite equation (3.4) in a completely dimensionless form:

$$\boxed{\frac{\partial \bar{\psi}}{\partial t} = \frac{i}{2} \frac{\partial^2 \bar{\psi}}{\partial \bar{x}^2}} \quad (3.14)$$

Here, we have a purely mathematical equation that we can solve, which represents the time evolution of a free wavefunction in accordance with the TDSE². From this point on, let us denote a dimensionless unit as 1[d.u.]. For example, let us denote one dimensionless unit of time as 1[d.u.] = ($\hbar/m a^2$)[T]. Notice that our dimensionless unit depends on a particle mass, m , which is never defined. This makes dimensionless units not only simpler, but also more versatile, than ordinary units. In addition, it is important to bear in mind that our dimensionless units will generally depend on the lattice constant, a ; where a represents the discrete interval length of our spatial grid. This means that if simulations are carried out on a finer grid, then the time intervals, for example, may also change; depending on how the positions are defined. Dimensionless units are rather non-intuitive, however they are widely used in computer programming, due to the way they can transform physical equations.

3.1.3 Finite Differences

Now that we have the equation that we need to compute (3.14), we should think about how the derivatives are going to be evaluated. The time derivative is naturally the most important because we are studying the wavefunction's time evolution, so that will make up our differential equation. The spatial derivative, however, can just be evaluated using a *central-difference* approximation. Central-difference approximations are simple methods used to approximate the value of a derivative at a certain point using Taylor series. For example, if we want to know the derivative of a function at a point x_0 , then we can do this by looking at the points either side of x_0 (*i.e.* $x_0 \pm h$). Assuming that the function we are analysing is infinitely differentiable (which holds for a Gaussian), then the Taylor expansion of the function at the points either side of x_0 may be written as:

$$\begin{aligned} f(x_0 + h) &= f(x_0) + hf'(x_0) + \frac{h^2 f''(x_0)}{2} + \dots \\ f(x_0 - h) &= f(x_0) - hf'(x_0) + \frac{h^2 f''(x_0)}{2} - \dots \end{aligned} \quad (3.15)$$

So, if we are looking for an expression for $f'(x_0)$, then we can obtain one by truncating the series after second order in h and subtracting one series from the other, which gives:

$$\begin{aligned} f(x_0 + h) - f(x_0 - h) &= 2hf'(x_0) + O(h^3) \\ \Rightarrow f'(x_0) &\approx \frac{f(x_0 + h) - f(x_0 - h)}{2h}. \end{aligned} \quad (3.16)$$

This is known as a 1st-order central-difference approximation for the first derivative. However, at the moment, we only need a second derivative approximation. Naturally, all we need to do for this is to add the two series in equation (3.15), to obtain:

$$\begin{aligned} f(x_0 + h) + f(x_0 - h) &= 2f(x_0) + h^2 f''(x_0) + O(h^4) \\ \Rightarrow f''(x_0) &\approx \frac{f(x_0 + h) - 2f(x_0) + f(x_0 - h)}{h^2}. \end{aligned} \quad (3.17)$$

This gives us the 1st-order central-difference approximation for the second derivative, which can be easily computed, provided that the function can be evaluated at either side of x_0 . As stated before, the error of these approximations is of the order of h^2 , where $h = a$ represents the extent to which the x -axis has been discretised. Therefore, the smaller the value of h , the better the approximation. The error in this stage of the computation is, in most cases, comparatively small but it should be taken into account nevertheless.

²Note that dimensionless equations generally need to be re-derived when working in higher dimensions.

3.1.4 The Classical Runge-Kutta Algorithm

Given that the spatial derivative in equation (3.14) has already been approximated, we now have what is essentially an ordinary differential equation (ODE) in t . Now we just need an appropriate numerical method to solve it. The 4th-order classical Runge-Kutta algorithm (RK4), is a well-known computational technique used to solve these types of ODEs³. It is popular in computation because it is robust, reasonably accurate and easy to program [38]. The derivation of the algorithm is rather cumbersome and so is left to appendix A.5. However, the logic involved is similar to that of the Euler method, since that can also be regarded as a Runge-Kutta method (of 1st-order). The RK4 algorithm may be defined in the following way:

Supposing we have an initial value problem of the form

$$\dot{\psi} = f(\psi) \quad \text{with} \quad \psi(x, t_0) = \psi_0(x), \quad (3.18)$$

where t_0 is some initial time and ψ_0 is some initial form of the wavefunction; then the iteration scheme for ψ may be written as

$$\psi_{n+1} = \psi_n + \frac{\delta t}{6}(K_1 + 2K_2 + 2K_3 + K_4), \quad (3.19)$$

where the Runge-Kutta coefficients are given by

$$\begin{aligned} K_1 &= f(\psi_n) \\ K_2 &= f\left(\psi_n + \frac{1}{2}K_1\delta t\right) \\ K_3 &= f\left(\psi_n + \frac{1}{2}K_2\delta t\right) \\ K_4 &= f(\psi_n + K_3\delta t), \end{aligned} \quad n \in \mathbb{N}. \quad (3.20)$$

As stated before, the error in this approximation is of the order of δt^5 and so this needs to be taken into account when choosing the time-step size. In addition, the algorithm becomes unstable when the time-step is too large.

In our particular case, we are going to start from an initial time $t_0 = 0$ and an initial wavefunction $\psi_0 = e^{-x^2}$ (*i.e.* the simplest unnormalised Gaussian function). Setting equation (3.14) into the form required for the RK4 initial value problem yields

$$\dot{\psi} = \frac{i}{2}\bar{\psi}'' \quad \text{with} \quad \bar{\psi}(x, 0) = e^{-x^2}. \quad (3.21)$$

Now, we have everything we need to simulate the evolution of a Gaussian wavefunction. Before we go on, however, we should check the solution we expect, to make sure that everything is working properly.

3.1.5 The One-Dimensional Exact Solution

To begin with, we have our initial Gaussian wavefunction

$$\psi(x, 0) = Ae^{-x^2}, \quad (3.22)$$

where A is a normalisation constant. For our computer simulations, the normalisation constant does not matter and the wavefunction is just left unnormalised and dimensionless for simplicity. This is acceptable because we are just interested in how the *form* evolves when running the simulations. However, here, let us derive the actual physical solution.

First of all, we need to normalise the wavefunction in accordance with the one-dimensional normali-

³The Runge-Kutta algorithms were developed in the early 20th century by German mathematicians C. Runge and M. W. Kutta [37].

sation condition (3.9) which leads to

$$A^2 \int_{-\infty}^{\infty} e^{-2x^2} dx = 1 \Rightarrow A = \left(\frac{2}{\pi} \right)^{\frac{1}{4}}, \quad (3.23)$$

for $A > 0$. Next, we note that since the wave only phase-rotates in time, the normalised wavefunction can, more generally, be described by

$$\mathfrak{F}\{\psi(x, t)\} = \hat{\psi}(k)e^{-\frac{iEt}{\hbar}}, \quad (3.24)$$

where E is the instantaneous energy eigenvalue of the wave and \mathfrak{F} denotes the Fourier transform⁴. Knowing that we can also obtain the wavefunction by taking a normalisable combination of stationary states, leads to the relation:

$$\psi(x, t) = \frac{1}{\sqrt{2\pi}} \int_{-\infty}^{\infty} \hat{\psi}(k)e^{-\frac{iEt}{\hbar}} e^{ikx} dk. \quad (3.25)$$

Since we know the initial wavefunction, we can find $\hat{\psi}(k)$ via Plancherel's theorem (see appendix A.4 for derivation):

$$\hat{\psi}(k) = \frac{1}{\sqrt{2\pi}} \int_{-\infty}^{\infty} \psi(x, 0)e^{-ikx} dx = \left(\frac{1}{2\pi} \right)^{\frac{1}{4}} e^{-\frac{k^2}{4}}. \quad (3.26)$$

Now, if we substitute this result back into equation (3.25) then we obtain

$$\psi(x, t) = \left(\frac{2}{\pi} \right)^{\frac{1}{4}} \frac{e^{-x^2/(1+2i\hbar t/m)}}{\sqrt{1+2i\hbar t/m}}, \quad (3.27)$$

where we have used the fact that the energy of a wave expressed as a function of its wavenumber is $E = \hbar^2 k^2 / 2m$. Using this result, we can finally calculate the probability density function:

$$|\psi(x, t)|^2 = \sqrt{\frac{2}{\pi}} \omega e^{-2\omega^2 x^2} \quad \text{where} \quad \omega \equiv \frac{1}{\sqrt{1+(2\hbar t/m)^2}}. \quad (3.28)$$

This is the exact solution for the one-dimensional time evolution of a Gaussian wavefunction. Note that as t increases, ω decreases. However, the centre of the Gaussian stays fixed at the origin and so the wavepacket should spread out to maintain the normalisation condition (3.9). By the symmetry of the expansion, we know that $\langle x \rangle = \langle p \rangle = 0$ and the second moments can be calculated by integration as in section 3.1.1. After the lengthy integration, we obtain

$$\begin{aligned} \langle x^2 \rangle &= \int_{-\infty}^{\infty} \psi^* \hat{x} \psi dx = \frac{1}{4\omega^2}, \\ \langle p^2 \rangle &= \int_{-\infty}^{\infty} \psi^* \hat{p} \psi dx = \hbar^2. \end{aligned} \quad (3.29)$$

This leads to an uncertainty product of

$$\Delta x \Delta p = \sqrt{\langle x^2 \rangle \langle p^2 \rangle} = \frac{\hbar}{2} \frac{1}{\omega} = \frac{\hbar}{2} \underbrace{\sqrt{1+(2\hbar t/m)^2}}_{\geq 1}. \quad (3.30)$$

This shows that our initial wavefunction at time $t = 0$ is a minimum uncertainty state (as shown in section 3.1.1) and uncertainty increases with time as the wavepacket spreads. [39]

⁴Here, $\hat{\psi}$ denotes to the Fourier transform of the corresponding wavefunction, ψ .

3.1.6 The One-Dimensional Computed Solution

If we now compute the evolution of the unnormalised single-particle wavefunction, $\psi_0 = e^{-x^2}$, then we obtain figure 3.1 for the wavepacket spreading⁵. This is in agreement with the exact solution obtained, since the probability density stays centred on $x = 0$ and spreads out in time. The areas under all the graphs in figure 3.1c are equal, in accordance with the normalisation condition (3.9). Figure 3.1a shows that the initial function quickly takes the form of a Gaussian multiplied by a cosine, due to the complex temporal phase factor. Similarly, figure 3.1b shows that the initial function takes the form of a Gaussian multiplied by a sine and so, by Pythagoras' theorem, the modulus squared of the wavefunction is Gaussian.

3.2 The Two-Dimensional Free TDSE

In the two-dimensional case, equation (3.3) reduces to

$$\frac{\partial}{\partial t}\psi(x, y, t) = \frac{i\hbar}{2m} \left\{ \frac{\partial^2}{\partial x^2}\psi(x, y, t) + \frac{\partial^2}{\partial y^2}\psi(x, y, t) \right\} \quad \Rightarrow \quad \dot{\psi} = \frac{i\hbar}{2m} \{ \partial_{xx}\psi + \partial_{yy}\psi \}. \quad (3.31)$$

In this section, the time evolution of a wavepacket will be computed in accordance with this equation, using the methods introduced in section 3.1. The exact solution naturally has a similar form to that calculated in section 3.1.5. In two dimensions, it is simply a radially symmetric analogue of the one-dimensional solution⁶, about the origin.

3.2.1 Dimensionless Form for the D -Dimensional Case

As mentioned in section 3.1.2, the dimensionless quantities may change when working in a new number of dimensions. In order to save work for the future, let us derive the general forms of the dimensionless quantities in an arbitrary number of dimensions, $D \in \mathbb{N}$.

In this case, similar to what was done before, we can make our D -dimensional position vector, \mathbf{r} , dimensionless by scaling it with the lattice constant:

$$\bar{\mathbf{r}} \equiv \frac{\mathbf{r}}{a}. \quad (3.32)$$

Given that the generalised D -dimensional normalisation condition is given by

$$\int_{\mathbb{R}^D} \psi\psi^* d^Dr = 1, \quad (3.33)$$

we can now make all of the quantities dimensionless. Since the differential element d^Dr has the dimensions of length to the power of D , the wavefunction, ψ , must have the dimensions of the reciprocal of the square root of length to the power of D (*i.e.* $1/\sqrt{a^D}$). Consequently, we can make ψ dimensionless by scaling it with the lattice constant as follows:

$$\bar{\psi} \equiv \sqrt{a^D}\psi. \quad (3.34)$$

As before, we can substitute relations (3.32) and (3.33) into the TDSE (3.3) to obtain

$$\frac{\partial}{\partial t} \frac{\bar{\psi}}{\sqrt{a^D}} = \frac{i\hbar}{2ma^2} \frac{\partial^2}{\partial \bar{\mathbf{r}}^2} \frac{\bar{\psi}}{\sqrt{a^D}}, \quad (3.35)$$

⁵Note that all the computer simulations in this thesis are carried out using *unnormalised* and *dimensionless* wavefunctions, so as to simplify the computations. This means that any normalisation conditions, given theoretically, only hold true as *proportionality conditions* for the graphs, where the normalisation constants are the constants of proportionality. Furthermore, since all the wavefunctions used in our computer simulations are dimensionless, the dashes are dropped, for brevity.

⁶Note that the normalisation constant in two dimensions would be $(2/\pi)^{\frac{1}{2}}$, rather than $(2/\pi)^{\frac{1}{4}}$.

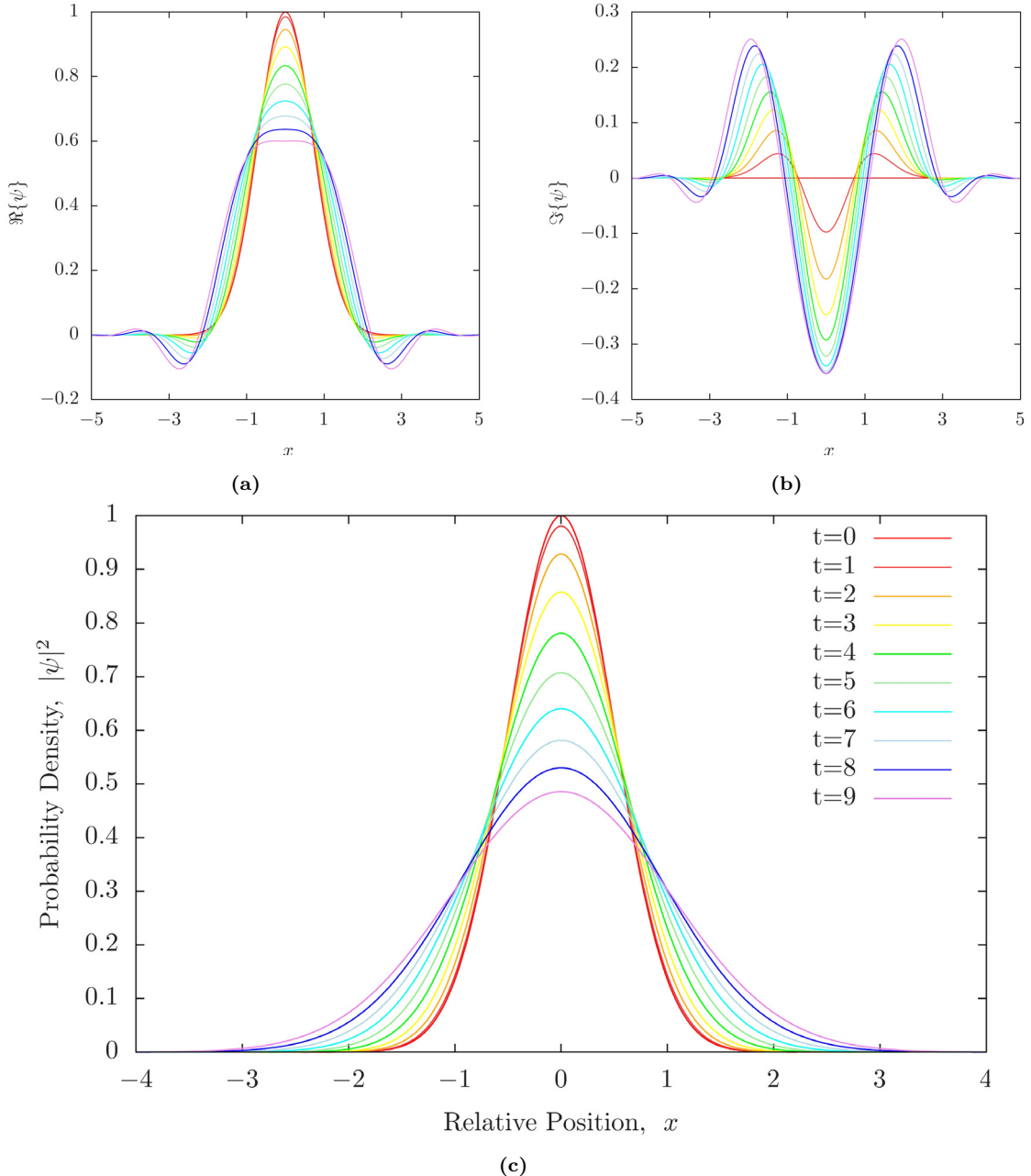


Figure 3.1: (a) The time evolution of the real part of the wavefunction, $\Re\{\psi\}$. (b) The time evolution of the imaginary part of the wavefunction, $\Im\{\psi\}$. (c) The time evolution of the unnormalised probability density, $|\psi|^2$, in temporal units of 0.1[d.u.]. The initial graph is $|\psi_0|^2 = e^{-2x^2}$ and the interval between each of the graphs is 10^4 iterations of a 10^{-5} [d.u.] time-step. The one-dimensional lattice in the x -direction has $n = 2000$ points and so the x -axes, which are defined from -10 to 10, are discretised into intervals of $h = 0.01$.

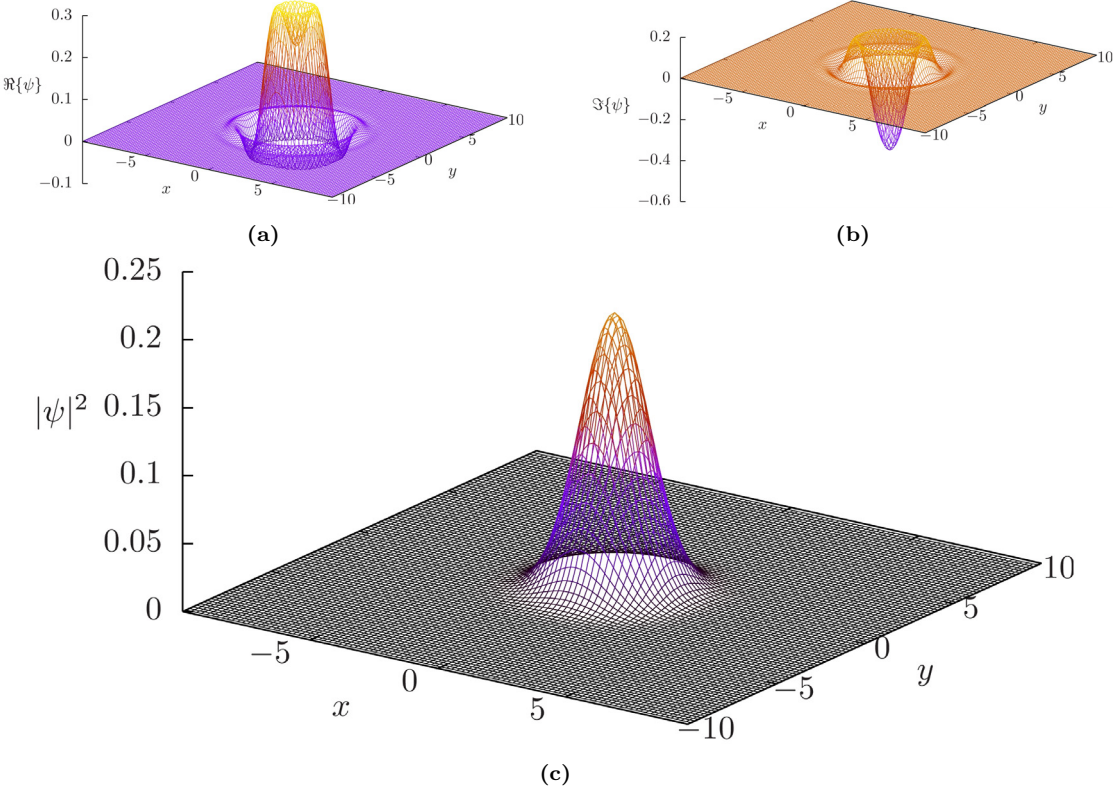


Figure 3.2: (a) The real part of the wavefunction, $\Re\{\psi\}$. (b) The imaginary part of the wavefunction, $\Im\{\psi\}$. (c) The unnormalised probability density, $|\psi|^2$, after a time of 1[d.u.]. The initial graph was $|\psi_0|^2 = e^{-2(x^2+y^2)}$ and the time evolution consisted of 10^5 iterations of a 10^{-5} [d.u.] time-step. The two-dimensional square lattice has $n^2 = 100^2$ points and so the axes in the figures are discretised into intervals of $h = 0.2$.

which after some cancellation and rearrangement leads to

$$\frac{\partial \bar{\psi}}{\partial t} \left(\frac{ma^2}{\hbar} \right) = \frac{i}{2} \frac{\partial^2 \bar{\psi}}{\partial \bar{r}^2} \quad \Rightarrow \quad \frac{\partial \bar{\psi}}{\partial t} = \frac{i}{2} \bar{\nabla}^2 \bar{\psi}. \quad (3.36)$$

This means that the subsequent definition of dimensionless time is the same as the identity given before (3.13). Therefore, the zero-potential TDSE is actually a special case and the dimensionless form of the equation is independent of the number of spatial dimensions that the equation had originally. The general dimensionless form of the two-dimensional, zero-potential TDSE may consequently be written as

$$\boxed{\frac{\partial \bar{\psi}}{\partial t} = \frac{i}{2} \left\{ \frac{\partial^2 \bar{\psi}}{\partial \bar{x}^2} + \frac{\partial^2 \bar{\psi}}{\partial \bar{y}^2} \right\}} \quad (3.37)$$

3.2.2 The Two-Dimensional Computed Solution

For the two-dimensional simulations, the initial wavefunction $\psi_0 = \psi(x, y, 0) = e^{-x^2-y^2}$ is chosen. Consequently, the expansion of the wavefunction has the same form as before but now with radial symmetry about the origin, as shown in figures 3.2a, 3.2b and 3.2c. The figures shown here depict the two-dimensional analogues of the one-dimensional case, at a time point just after the last curves shown in figure 3.1. Note that the maximum probability density for the two-dimensional case is smaller than the corresponding value in one dimension; this is due to the fact that in two dimensions, the normalisation proportionality sets the *volume* under the curve, rather than the area.

Simulating the Magnetic Trap Confinement of a Bose Gas

In the previous chapter, we saw how we could simulate the time evolution of a free, non-interacting Bose-fluid distribution using the zero-potential TDSE. However, in order to achieve condensation, the gas distribution is not free at the beginning, it is in a trap. Furthermore, the bosons in the fluid collide and scatter off one another and so the distribution is interacting. In the experiments of *Bagnato et al.*, a gas of ^{87}Rb atoms is cooled using magneto-optical confinement with a harmonic potential [2]. In this chapter, we explain how this trapping mechanism can be simulated, using the Gross-Pitaevskii equation.

4.1 The Thomas-Fermi Distribution

By trapping and cooling an ensemble of atoms down into their lowest quantum state, the kinetic energy of the individual atoms becomes increasingly negligible compared to their potential and interaction energies. Taking the time-independent GPE, for instance, we can approximate this limit by neglecting the kinetic term:

$$\begin{aligned} \mu\Psi &= \left[-\frac{\hbar^2}{2m} \nabla^2 + \hat{V} + g|\Psi|^2 \right] \Psi \\ &\Rightarrow \mu\Psi \approx (\hat{V} + g|\Psi|^2)\Psi. \end{aligned} \quad (4.1)$$

Equation (4.1) is what is known as the Thomas-Fermi approximation (introduced in section 2.4), named after Llewellyn Thomas and Enrico Fermi. The approximation is an offshoot of the semi-classical Thomas-Fermi model, developed shortly after the introduction of the Schrödinger equation [40] [41]. A simple rearrangement of the equation leads to an expression for the probability density in this approximation:

$$|\Psi|^2 = \begin{cases} \frac{1}{g}(\mu - V) & \text{if } V < \mu \\ 0 & \text{otherwise.} \end{cases} \quad (4.2)$$

Now we know that since the interaction constant, g , and the chemical potential, μ , are both constant in space, then we can examine the functional form of the potential function, V , in order to deduce the spatial distribution of the probability density. In these simulations, just as in the experiments of *Bagnato et al.* (and most cooling and trapping experiments for that matter), we will use a harmonic trapping potential. In Cartesian coordinates, this may be written as

$$V(x, y, z) = \frac{1}{2}m [\omega_x^2x^2 + \omega_y^2y^2 + \omega_z^2z^2], \quad (4.3)$$

where ω_i is the angular frequency of the oscillator in the i -direction, with $i \in \{x, y, z\}$. The potential well of a quantum harmonic oscillator is paraboloidal in nature and so, since the potential is the only

spatially varying quantity in the Thomas-Fermi approximation, we know that the probability density will also be paraboloidal. [18] [17]

4.2 The Thomas-Fermi Paraboloid

When these experiments are being conducted in the laboratory, the initial configuration consists of a homogeneous condensate which is deformed due to the trapping potential. After this, the gas is allowed to gradually reach dynamic equilibrium within the trap. When programming computer simulations of this, however, there are two possibilities: either one could skip this transition and approximate the final ground state distribution directly (for non-turbulent condensates), or one could start with a free distribution and then let it ‘evolve’ to the ground state (for turbulent cases). In this section, let us consider the prior.

4.2.1 The One-Dimensional Case

Let us consider a one-dimensional harmonic potential of the form:

$$V(x) = \frac{1}{2}m\omega_x^2x^2. \quad (4.4)$$

Now, looking back at the equation for the Thomas-Fermi approximation we can see that, in the region of interest,

$$|\Psi|^2(x) = \frac{1}{g} \left(\mu - \frac{1}{2}m\omega_x^2x^2 \right). \quad (4.5)$$

In a standard simulation, we will set all the parameters, apart from the chemical potential. Therefore, once we can calculate an expression for μ , we can consequently also calculate the Thomas-Fermi paraboloid. From the one-dimensional normalisation condition (3.9), we know that the integral of the probability density over all space is unity. However, if we consider a system of N particles, then we know that the probability density can be interpreted as the number density, $\rho(x)$, with the equivalent normalisation condition:

$$\int_{-\infty}^{\infty} \rho(x) dx = N. \quad (4.6)$$

Now, if we integrate both sides of equation (4.5) over all space then we obtain:

$$\begin{aligned} N &= \frac{1}{g} \int_{-\infty}^{\infty} \left(\mu - \frac{1}{2}m\omega_x^2x^2 \right) dx \\ &= \frac{\mu}{g} \int_{-R_{\text{TF}}}^{R_{\text{TF}}} \left(1 - \frac{x^2}{R_{\text{TF}}^2} \right) dx \\ &= \frac{\mu R_{\text{TF}}}{g} \int_{-1}^1 (1 - \tilde{x}^2) d\tilde{x} \\ &= \frac{4}{3} \frac{\mu R_{\text{TF}}}{g} \\ &= \frac{4}{3} \sqrt{\frac{2}{m\omega_x^2}} \frac{\mu^{3/2}}{g} \\ \Rightarrow \mu_{1D} &= \left[\frac{3}{4} \sqrt{\frac{m}{2}} g\omega_x N \right]^{2/3}. \end{aligned} \quad (4.7)$$

In this derivation, we have defined the Thomas-Fermi radius, $R_{\text{TF}} \equiv \sqrt{2\mu/m\omega_x^2}$, to be the distance from the x -coordinate of the maximum of the parabola to the point where it intersects the axis (as discussed in section 2.4). We have also used the fact that the number density can never be negative ($\rho(x) \geq 0$) when changing variables to $\tilde{x} = x/R_{\text{TF}}$.

Since m , g , ω_x and N are all fixed parameters for the system, we can now arrive at an expression for the Thomas-Fermi parabola in terms of known quantities:

$$|\Psi|^2(x) = \frac{1}{g} \left(\left[\frac{3}{4} \sqrt{\frac{m}{2}} g \omega_x N \right]^{2/3} - \frac{1}{2} m \omega_x^2 x^2 \right). \quad (4.8)$$

This is the distribution we could start with, if we want to skip the transition from a free to a trapped, non-turbulent distribution or, alternatively, this is what we could check the evolved distribution against to see how close it is to the ground state.

4.2.2 The Two-Dimensional Case

Now, in a similar fashion, let us consider the two-dimensional potential function:

$$V(x, y) = \frac{1}{2} m [\omega_x^2 x^2 + \omega_y^2 y^2]. \quad (4.9)$$

Using a generalised form of equation (4.6),

$$\int_{\mathbb{R}^D} \rho d^D x = N, \quad (4.10)$$

coupled with the two-dimensional equation for the Thomas-Fermi approximation,

$$|\Psi|^2(x, y) = \frac{1}{g} \left(\mu - \frac{1}{2} m [\omega_x^2 x^2 + \omega_y^2 y^2] \right), \quad (4.11)$$

we can integrate both sides over all space to obtain the chemical potential, as before. This yields:

$$\begin{aligned} N &= \frac{1}{g} \int_{-\infty}^{\infty} \int_{-\infty}^{\infty} \left(\mu - \frac{1}{2} m [\omega_x^2 x^2 + \omega_y^2 y^2] \right) dx dy \\ &= \frac{\mu}{g} \int_{-R_{\text{TF}}^x}^{R_{\text{TF}}^x} \int_{-R_{\text{TF}}^y}^{R_{\text{TF}}^y} \left(1 - \frac{x^2}{R_{\text{TF}}^x} - \frac{y^2}{R_{\text{TF}}^y} \right) dx dy \\ &= \frac{\mu R_{\text{TF}}^x R_{\text{TF}}^y}{g} \int_{-1}^1 \int_{-1}^1 (1 - \tilde{x}^2 - \tilde{y}^2) d\tilde{x} d\tilde{y} \\ &= \frac{4 \mu R_{\text{TF}}^x R_{\text{TF}}^y}{3 g} \\ &= \frac{4}{3} \sqrt{\frac{2}{m \omega_x^2}} \sqrt{\frac{2}{m \omega_y^2}} \mu^2 \\ \Rightarrow \mu_{2D} &= \left[\frac{3}{4} \frac{m}{2} g \omega_x \omega_y N \right]^{1/2}. \end{aligned} \quad (4.12)$$

Notice that this expression has a similar form to the one derived for the one-dimensional case. Here, R_{TF}^x and R_{TF}^y are the Thomas-Fermi radii in the x and y -directions, respectively¹. Now, as before, we can write down the equation for the Thomas-Fermi paraboloid in terms of the known quantities:

$$|\Psi|^2(x, y) = \frac{1}{g} \left(\left[\frac{3}{4} \frac{m}{2} g \omega_x \omega_y N \right]^{1/2} - \frac{1}{2} m [\omega_x^2 x^2 + \omega_y^2 y^2] \right). \quad (4.13)$$

This procedure could then trivially be extended into three dimensions.

¹The superscripts x and y used for these symbols are simply indices used for clarity. They do not imply raising to a power.

4.3 Imaginary Time Propagation

In order to start with a topologically defective ground state, however, we need an alternative way of reaching this configuration. We need to project our desired state on the topologically allowed ground state of the system. For this, we can use a process known as *imaginary time propagation*.

4.3.1 Solving the GPE in Imaginary Time

To begin with, let us define some imaginary time variable,

$$\tau \equiv \frac{it}{\hbar}. \quad (4.14)$$

The reason for the factor of $1/\hbar$ will become evident in the next step. We can subsequently rewrite our time-dependent GPE in terms of this new variable, using the chain rule:

$$\hat{H}\Psi = i\hbar \frac{\partial\Psi}{\partial t} = i\hbar \frac{\partial\tau}{\partial t} \frac{\partial\Psi}{\partial\tau} = -\frac{\partial\Psi}{\partial\tau}. \quad (4.15)$$

Now, it can be seen how the factor of $1/\hbar$ merely simplifies the resulting equation. From the fourth postulate of quantum mechanics, we know that:

“When a measurement of a dynamic variable represented by a Hermitian operator is carried out on a system whose wavefunction is Ψ , then the probability of the result being equal to a particular eigenvalue q_n will be $|a_n|^2$, where $\Psi = \sum_n a_n \Phi_n$ and the Φ_n are the eigenstates of the operator corresponding to the q_n .” [42]

Using the fact that the eigenstates of our condensate wavefunction, Ψ , form a complete orthonormal set, we can write our wavefunction as

$$\Psi = \sum_n a_n \Phi_n \quad \forall n \in \mathbb{N}, \quad (4.16)$$

where a_n and Φ_n are the eigenvalues and -states, respectively. Since every eigenstate has a corresponding energy eigenvalue,

$$\frac{\partial\Phi_n}{\partial\tau} = -E_n \Phi_n \quad \forall n \in \mathbb{N} : E_n > 0. \quad (4.17)$$

Now, since the Hamiltonian operator is time-independent, we can write our eigenfunction at a later complex time, $t_0 + \tau$, as

$$\Phi_n(t_0 + \tau) = \Phi_n(t_0) e^{-E_n \tau}. \quad (4.18)$$

Using this result, we can now see that our wavefunction at some imaginary time, τ , may be written as

$$\Psi(\tau) = \sum_n a_n \Phi_n(\tau) = \sum_n a_n \Phi_n(0) e^{-E_n \tau}. \quad (4.19)$$

Let us now denote the ground state energy eigenvalue as E_0 . We know that E_0 is the smallest energy eigenvalue possible and so it will decay the slowest in imaginary time. Separating out the ground state in this equation yields

$$\Psi(\tau) = a_0 e^{-E_0 \tau} \Phi_0(0) + \sum_{n=1}^{\infty} a_n \Phi_n(0) e^{-E_n \tau}. \quad (4.20)$$

Therefore, as imaginary time propagates, the higher order eigenstates exponentially decay faster than the ground state and so the ground state can eventually be filtered to a very good approximation:

$$\Psi(\tau) \approx \Psi_0(0) e^{-E_0 \tau} \quad \forall \tau \gg 0. \quad (4.21)$$

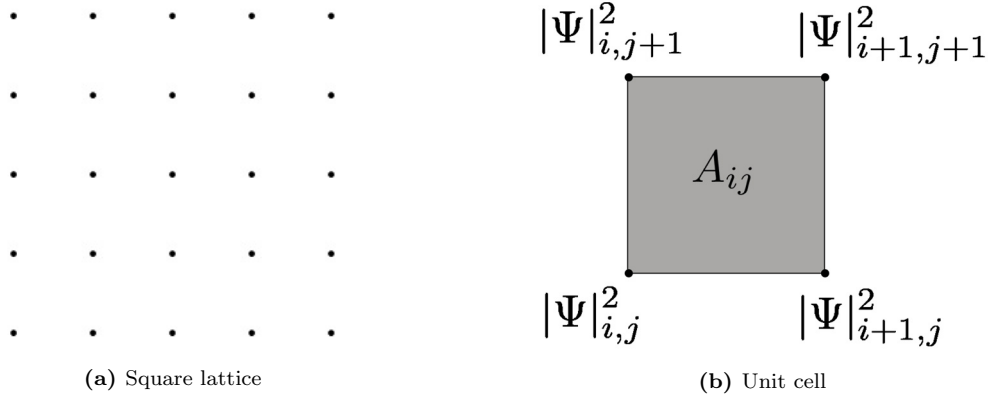


Figure 4.1: (a) Diagrammatic representation of a section of the two-dimensional, spatial square lattice used for computation. (b) Unit cell of the square lattice used for computation. The number density has been labeled at each of the four corner points and A_{ij} denotes the area of the cell.

Of course, during the process, the magnitude of the wavefunction will also decrease considerably. In order to reconcile this issue, the particle number is actively rescaled in code. [1]

4.3.2 The Particle Number Rescale Algorithm

The rescaling process employed is very simple in principle. After every loop of imaginary time propagation, we simply count the total number of particles by performing a numerical integral over the whole lattice. Then, if we notice that we have lost some, we can rescale our wavefunction accordingly. Let us now depict our grid points as those forming a square lattice, shown in figure 4.1a. To perform our integral, we find the area of one unit cell of this lattice and then multiply this by the average of the probability densities at the four corner points. Then, to find the complete integral, we just sum all of the particle numbers over the whole lattice. From our normalisation condition (3.33), we know that the probabilities should always sum to unity. If we find that they do not, then we can multiply our wavefunction by the appropriate scale factor. Let us denote the area of each unit cell as, A_{ij} , where i and j are the indices for the x and y -directions respectively (as shown in figure 4.1b). At the moment, the areas of all the unit cells will always be the same (*i.e.* $A_{ij} = a^2 = h^2$). However, let us keep these calculations general for when we come to deal with an expanding coordinate system (see section 6.1). Let us also denote the average probability density of the four corner points as $\langle |\psi|^2 \rangle_{ij}$. Now, our particle number rescale algorithm is essentially imposing the standard normalisation condition and so, if we refer to total particle number, we can equivalently convert this single-particle wavefunction into the total condensate wavefunction and state that

$$\sum_i \sum_j A_{ij} \langle |\psi|^2 \rangle_{ij} \stackrel{!}{=} 1 \quad \Rightarrow \quad \sum_i \sum_j A_{ij} \langle |\Psi|^2 \rangle_{ij} \stackrel{!}{=} N. \quad (4.22)$$

Let us subsequently define a scale factor, κ , such that

$$\kappa \equiv \frac{N}{\sum_i \sum_j A_{ij} \langle |\Psi|^2 \rangle_{ij}}, \quad (4.23)$$

where our rescaling process is simply an iterative computation of

$$\Psi_{n+1} = \sqrt{\kappa} \Psi_n \quad \forall n \in \mathbb{N}. \quad (4.24)$$

This assignment is performed at the end of every imaginary time step. We are still filtering the ground state, since the exponential decay factors are still present; however, now at the end of the process, we will not have lost any particles and our ground state will not be reduced in magnitude.

4.4 The Dimensionless Gross-Pitaevskii Equation

For this ground state evolution process, we will be evolving our standard time-dependent GPE (2.21) in imaginary time. However, before we proceed, we should make our GPE dimensionless for the reasons discussed in section 3.1.2. Let us derive the dimensionless GPE in D dimensions, so that it will apply to all cases.

We can start, as before, by scaling our position vector with some lattice constant and then invoking the D -dimensional normalisation condition. This leads to

$$\bar{\mathbf{r}} \equiv \frac{\mathbf{r}}{a} \quad \Rightarrow \quad \bar{\Psi} \equiv \sqrt{a^D} \Psi. \quad (4.25)$$

Now, all we have to do is substitute these relations into the time-dependent Gross-Pitaevskii equation and define our new variables so that we eliminate all of the physical constants. In D dimensions, the original time-dependent GPE may be written as

$$\left[-\frac{\hbar^2}{2m} \frac{\partial^2}{\partial \mathbf{r}^2} + V + g|\Psi|^2 \right] \Psi = i\hbar \frac{\partial \Psi}{\partial t}. \quad (4.26)$$

If we substitute in the relations given in (4.25), then the equation becomes

$$\left[-\frac{\hbar^2}{2ma^2} \frac{\partial^2}{\partial \bar{\mathbf{r}}^2} + V + g \frac{|\bar{\Psi}|^2}{a^D} \right] \frac{\bar{\Psi}}{\sqrt{a^D}} = \frac{i\hbar}{\sqrt{a^D}} \frac{\partial \bar{\Psi}}{\partial t}, \quad (4.27)$$

which after some rearrangement leads to

$$-\frac{1}{2} \frac{\partial^2 \bar{\Psi}}{\partial \bar{\mathbf{r}}^2} + V \left(\frac{ma^2}{\hbar^2} \right) \bar{\Psi} + g \left(\frac{ma^{2-D}}{\hbar^2} \right) |\bar{\Psi}|^2 \bar{\Psi} = i \frac{\partial \bar{\Psi}}{\partial t} \left(\frac{ma^2}{\hbar} \right). \quad (4.28)$$

As shown in equation (4.28), we have grouped all of the physical constants beside all of the parameters that we want to scale. We can now easily define all the dimensionless counterparts for V , g and t . Eliminating all the physical constants in this way allows to write our general dimensionless GPE as

$$-\frac{1}{2} \frac{\partial^2 \bar{\Psi}}{\partial \bar{\mathbf{r}}^2} + \bar{V} \bar{\Psi} + \bar{g} |\bar{\Psi}|^2 \bar{\Psi} = i \frac{\partial \bar{\Psi}}{\partial \bar{t}}, \quad (4.29)$$

or, expressed in a more compact form:

$$\left[-\frac{1}{2} \bar{\nabla}^2 + \bar{V} + \bar{g} |\bar{\Psi}|^2 \right] \bar{\Psi} = i \partial_{\bar{t}} \bar{\Psi}$$

(4.30)

where the dimensionless parameters \bar{V} , \bar{g} , \bar{t} are defined in table 4.1.

4.5 Boundary Conditions

The boundary conditions that are used in these calculations are of critical importance and are unfortunately, rather tricky to implement. If we do not set any explicit boundary conditions for the imaginary time propagation then our resulting simulation will suffer from reflections, interference and discontinuities. The reflections will arise when our wavefunction reaches the lattice edge and then reflects back again. Interference will also occur if these reflected wavefronts superpose. Furthermore, discontinuities and other inconsistencies may be observed when the case of the wavefunction hitting the lattice edge is left completely unaccounted. In choosing the boundary conditions for the imaginary time propagation, we should simply choose the ones that are effective for our particular simulations. By experimenting with different set-ups, we can conclude that *Neumann boundary conditions* work comparatively well in this situation. Neumann boundary conditions are second-type or *fixed derivative*

Table 4.1: Dimensionless parameter definitions

Parameter	Symbol	Dimensionless Counterpart
Time	t	$\bar{t} \equiv \frac{\hbar}{ma^2} t$
External Potential	V	$\bar{V} \equiv \frac{ma^2}{\hbar^2} V$
Interaction Constant	g	$\bar{g} \equiv \frac{ma^{2-D}}{\hbar^2} g$
Probability Density	$ \Psi ^2$	$ \bar{\Psi} ^2 \equiv a^D \Psi ^2$

itive boundary conditions. Therefore, at the lattice edge, we simply set the spatial derivative of the wavefunction equal to zero. In this way, the kinetic term of our GPE vanishes and so, we are essentially evaluating a kinetic-free time-dependent GPE, on the lattice border. This drastically reduces reflections and removes inconsistencies and discontinuities in the phase and density profiles.

4.6 The Computed Solutions

Now that we have a complete framework in place, we can start to simulate the trapping process. To recap, we shall start with a Bose-fluid distribution in the non-interacting limit (*i.e.* a Gaussian). Then, we shall evolve this distribution in accordance with the GPE in imaginary time, whilst continuously making sure that the spatial derivative of the wavefunction is kept fixed at the lattice border and the particle number is conserved. We shall propagate the distribution in imaginary time, until it reaches its ground state to a very good approximation.

For the one-dimensional simulations, we shall again start with the simplest unnormalised wavefunction, $\Psi_0 \propto e^{-x^2}$. Then we can perform the propagation as shown in figure 4.2a. As one can see, the original Gaussian is gradually taking a parabolic shape due to the imaginary time propagation. Furthermore, the rescale algorithm is ensuring that the area under all of the graphs is equal. If we now carry on the propagation, we will reach the Thomas-Fermi limit to a very good approximation, as shown in figure 4.2b. Here, one can see that the ground state can essentially be approximated by a parabola, apart from the small tails close to the x -axis. The distance over which the Thomas-Fermi distribution drops by a factor $1/e$, away from the parabolic approximation, is known as the condensed matter *coherence length* or *healing length*, ξ , as shown in figure 4.2c. The general definition of ξ is “the distance over which the wavefunction tends to its bulk value after being subjected to a localized perturbation” [18] and, by equating kinetic and interaction energies at these length scales, may be expressed as

$$\frac{\hbar^2}{2m\xi^2} = g\rho \quad \Rightarrow \quad \xi = \frac{\hbar}{\sqrt{2mg\rho}} \propto \frac{1}{\sqrt{a_s}}. \quad (4.31)$$

This length will become important when we start to look at turbulence induction in chapter 5.

We can follow a similar procedure in two dimensions. We start, as before, with the simplest unnormalised condensate wavefunction, $\Psi_0 \propto e^{-x^2-y^2}$. Figure 4.3 shows how the two-dimensional Gaussian density distribution gradually tends to an approximate paraboloid, just as in the one-dimensional case. Note that in this figure, the angular trap frequencies in the x and y -directions are not equal, which results in the elliptical density profile (shown in figure 4.3e). This is the desired ground state profile for a simulation of the experiments carried out by *Bagnato et al.* [43].

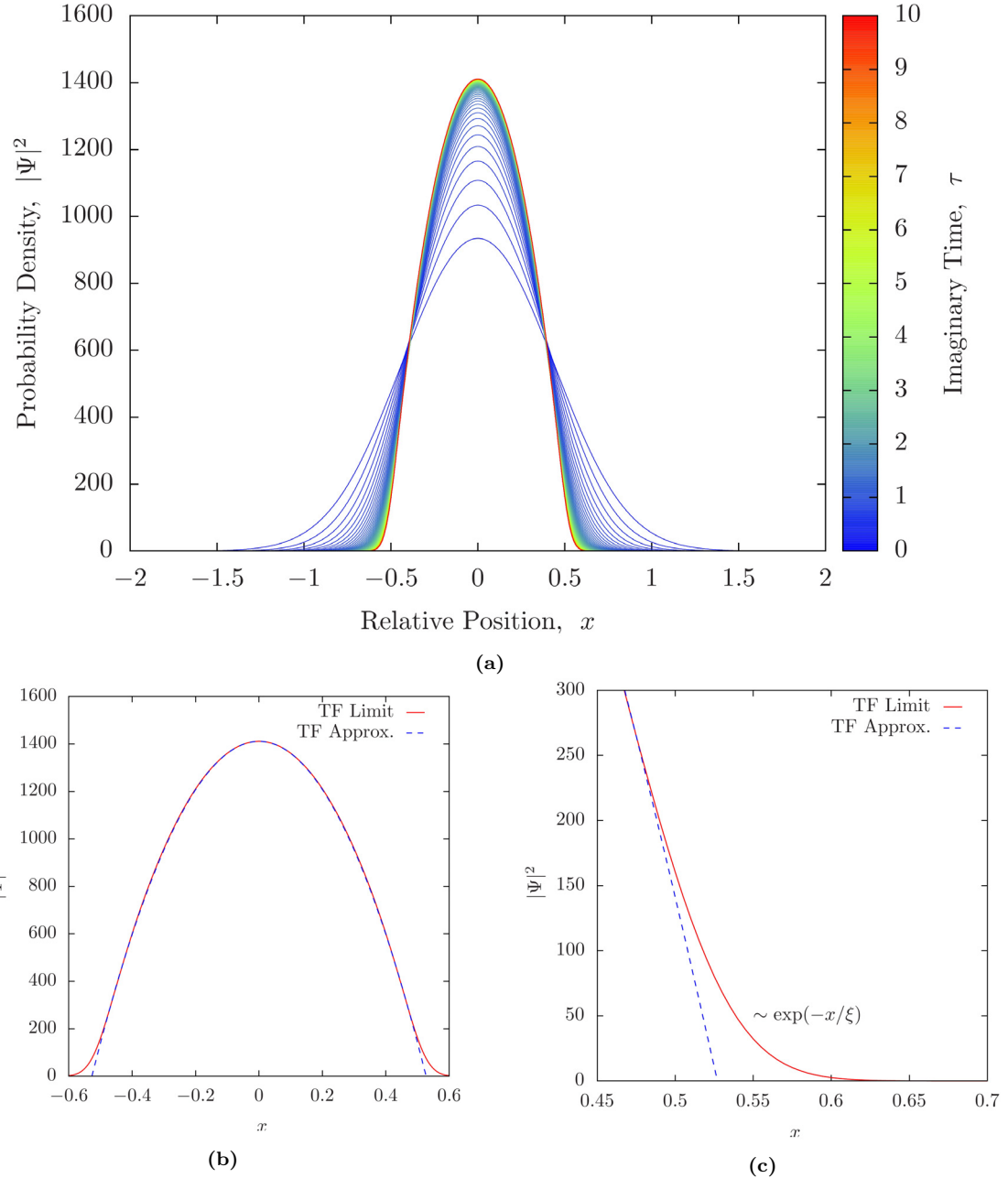


Figure 4.2: (a) The time evolution of the unnormalised probability density, $|\Psi|^2$, in imaginary temporal units of $10^{-3}i$ [d.u.]. The initial graph has the form $|\Psi_0|^2 \propto e^{-2x^2}$ and the interval between each of the 100 curves is 10^3 iterations of a $10^{-7}i$ [d.u.] imaginary time-step. (b) The form of $|\Psi|^2$ after 10^5 iterations of a $10^{-7}i$ [d.u.] imaginary time-step (*i.e.* the last curve from figure 4.2a). Superposed onto this is the Thomas-Fermi parabola approximation (see section 4.2.1). (c) A zoomed-in view of figure 4.2b. The healing length, ξ , is marked accordingly. (a,b,c) The one-dimensional lattice in the x -direction has $n = 4000$ points and so the x -axes, which are defined from -10 to 10, are discretised into intervals of $h = 0.005$. The interaction constant is $g = 1$ [d.u.], the angular frequency is $\omega_x = 100$ [d.u.] and the particle number is $N = 1000$.

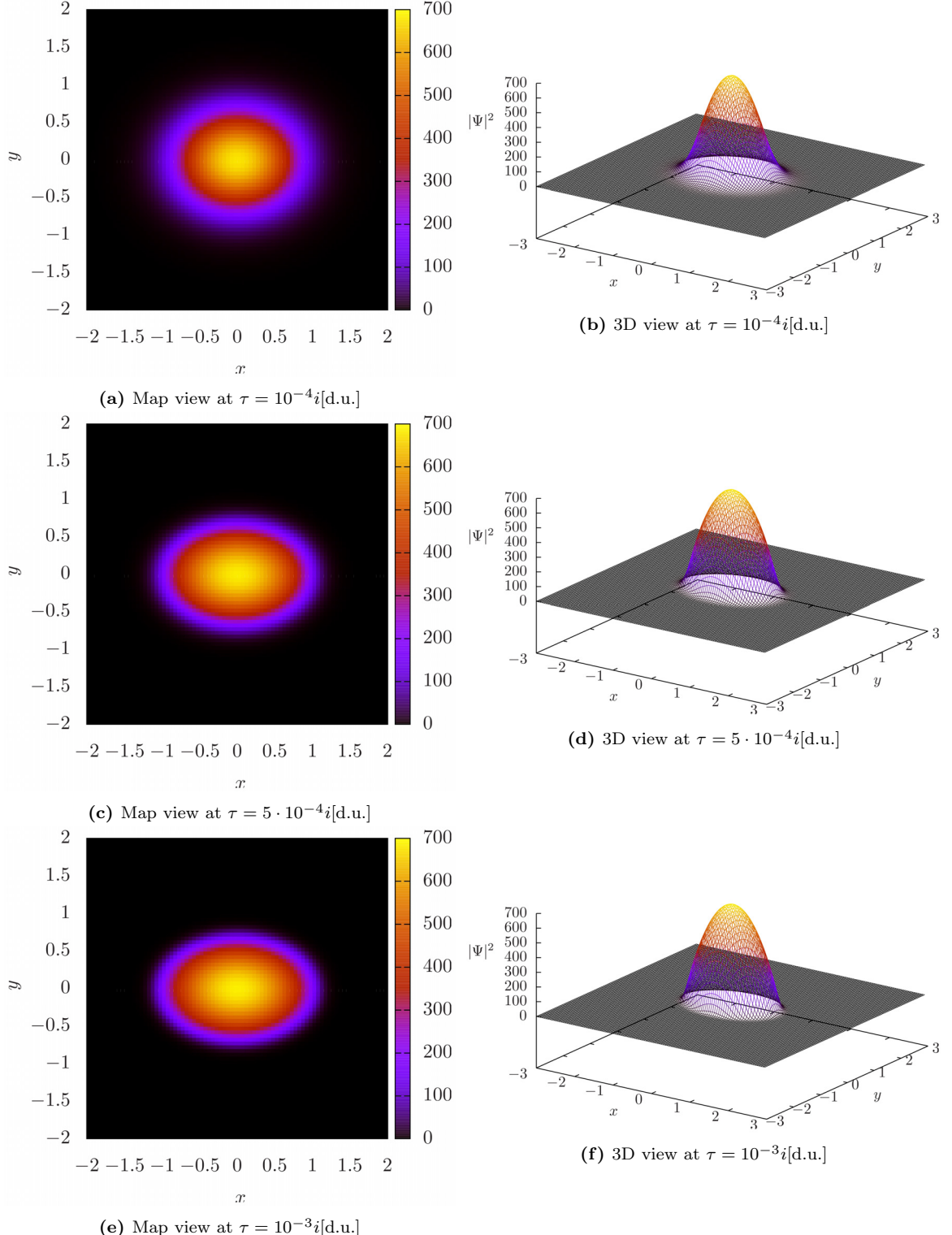


Figure 4.3: The form of the unnormalised probability density, $|\Psi|^2$, subject to an anisotropic potential well, after imaginary time intervals of $10^{-4}i$ [d.u.], $5 \cdot 10^{-4}i$ [d.u.] and $10^{-3}i$ [d.u.], respectively. The initial form of the wavefunction was $|\Psi_0|^2 \propto e^{-2(x^2+y^2)}$ and the total imaginary time evolution consisted of 10^4 iterations of a $10^{-7}i$ [d.u.] imaginary time-step (see figure D.1 for the isotropic case). The two-dimensional square lattice has $n^2 = 120^2$ points and so the axes in the figure, which are all defined from -3 to 3, are discretised into intervals of $h = 0.05$. The interaction constant is $g = 10$ [d.u.], the angular frequencies are $\omega_x = 100$ [d.u.], $\omega_y = 150$ [d.u.] and the particle number is $N = 1000$.

Inducing Turbulence in the Trapped Bose Condensate

In the previous chapters, we have shown how a condensate wavefunction may be confined by an oscillating potential and brought to its ground state. We have also shown how we can simulate the evolution of wavefunctions. With these techniques alone, we already have the tools needed to compute the expansion of Bose-Einstein condensates. However, now we need to consider the last feature of our simulation: turbulence. Naturally, there are many different methods that one could employ to induce turbulence in a condensate. As stated before in chapter 1, the method employed by *Bagnato et al.* involved tilting the axis of anti-Helmholtz coils relative to the long axis of the ellipsoid, in order to induce unstable density fluctuations and bring the condensate into the turbulent regime [2]. This is a common way to induce turbulence in condensates experimentally but in actual fact, the methods employed are arbitrary to a certain extent. This is because the final aim of this procedure is to induce quantum vortices in the condensate, the methods that one chooses to achieve this are, in the most part, irrelevant. The experiment under investigation is concerned with the free expansion of a turbulent condensate and not the process by which turbulence is induced. Consequently, turbulence in this simulation is induced somewhat artificially, in that phase rotations are simply imprinted in the condensate during imaginary time propagation. The end result of this, however, is a regular array of quantum vortices, similar to those found in actual experiments [44].

5.1 The Quantum Vortex

As previously alluded, quantum vortices are quantized flow circulations that arise naturally in turbulent superfluids [45]. These phenomena occur as a direct consequence of the properties of a superfluid outlined in section 2.3. For the purposes of our simulations, however, all that we need to be aware of is that they are quantized rotations. For simplicity, we shall introduce these as phase rotations in our condensate. This means that at the point of inception, we will not be able to see the quantum vortices in the density profile of the condensate (*i.e.* it would not be physically observable). Therefore, we will not add the phase rotations at the end of the imaginary time propagation because we need vortices in the density profile before we begin our real-time expansion. Another option would be adding the phase rotations at the beginning of the imaginary time propagation, so that they have plenty of time to develop in the density profile. Unfortunately, this is not a viable solution either, since then the vortices could escape from the cloud. The Thomas-Fermi approximation process evolves the system into its ground state and during the imaginary time evolution the condensate will be approaching its most energetically favourable configuration. This stable ground state configuration naturally does not allow for any arbitrary configuration of vortices. Consequently, the best solution is to introduce the phase rotations near the end of the imaginary time propagation, so that the vortices have enough time to fully develop¹ but not enough time to disrupt the phase or density profiles. Let us first look

¹In this context, ‘fully developed’ implies that the vortex core is at zero density, in so far as the lattice can resolve.

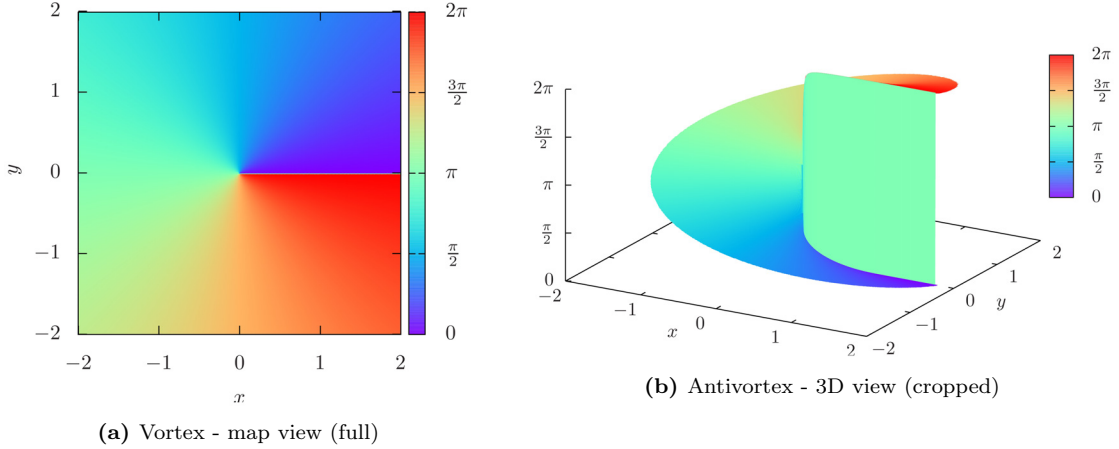


Figure 5.1: (a) Phase plot of a single central vortex at the point of inception. The phase, ϕ , is defined in the range $\phi \in [0, 2\pi]$. (b) Phase, $\phi \in (0, 2\pi]$, of a central antivortex conditionally plotted, when the density exceeds a certain value. Here, the density profile is radially symmetric.

in more detail as to what it means to add a phase rotation in our condensate. Let us consider a real condensate wavefunction, $\Psi(\mathbf{r}, t)$, at some arbitrary point in its imaginary time development into the ground state. Now, let us introduce a phase rotation so that our static wavefunction is multiplied by a phase factor, $e^{i\phi}$, and our new wavefunction has the form given in (2.22), where ϕ now denotes the phase of a single vortex. Initially, this new wavefunction will just have the phase defined on a typical Argand diagram with coordinates centred on where we want the vortex to develop². At inception, the phase profile for a condensate with one central vortex will look like the profile shown in figure 5.1a. As we evolve our condensate wavefunction in accordance with the imaginary time GPE, this phase rotation will start to manifest itself as a radially symmetric dip in the density profile, such as the profile shown in figure 5.2³. Note that imaginary time propagation now has a negligible effect on the phase profile of the system and so, for the case of a central vortex, the phase profile will continue to look like figure 5.1a up to the start of the real-time evolution.

By the end of the imaginary time propagation, the density distribution will have an approximately paraboloidal envelope; however, due to the healing length of the system, it will still have an asymptotic tail to the xy -plane. This effectively means that the bosonic field is spread across the whole grid and so, there will be a phase defined at all points. Since we are only interested in the phase within the bulk of the condensate, we can cut off the asymptotic tail when plotting the phase distribution, as demonstrated for the case of a central antivortex in figure 5.1b.

If we subsequently want to simulate more than one vortex, then we follow a similar procedure. However now, instead of multiplying our wavefunction by one phase factor, we may multiply it by the desired number, such that

$$\Psi = |\Psi| \prod_{m=1}^{N_V} e^{i\phi_m(\mathbf{r}, t)} = |\Psi| \exp \left\{ i \sum_{m=1}^{N_V} \phi_m(\mathbf{r}, t) \right\}, \quad (5.1)$$

where N_V is the desired number of vortices. This shows that for multiple vortices, the phase profile of the complete system will be the sum of the phase profiles of the individual vortices. In practice, each ϕ_m is centred on a different point so that the vortices are distinct.

Let us now turn our attention to the anatomy of a fully developed central vortex, such as the one shown in figure 5.2. As mentioned before, the centre of a vortex is defined as the origin of the phase

²It is arbitrary how we define the phase in an Argand diagram, so for these simulations let us define $\phi \in [0, 2\pi]$.

³The full vortex development is shown in appendix D.2.

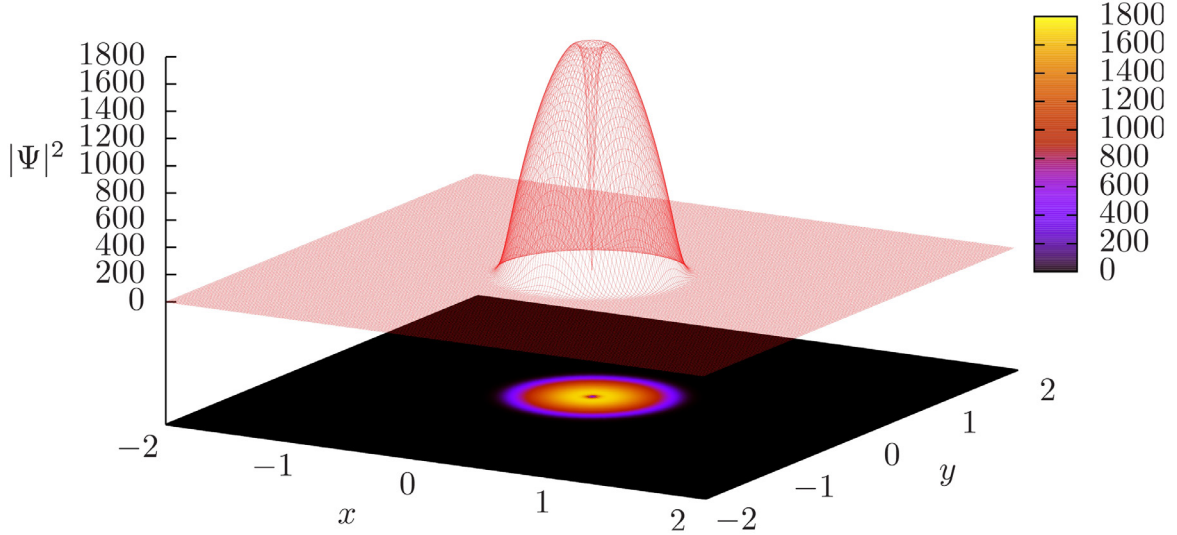


Figure 5.2: The form of a fully developed quantum vortex in the unnormalised probability density distribution, $|\Psi|^2$, subject to an isotropic potential well, after an imaginary time interval of $10^{-2}i[\text{d.u.}]$. The initial form of the wavefunction was $|\Psi_0|^2 \propto e^{-2(x^2+y^2)}$ and the total imaginary time evolution consisted of 10^4 iterations of a $10^{-6}i[\text{d.u.}]$ imaginary time-step, where the phase of the vortex was imprinted 80% of the way through⁴(see figure D.2). The two-dimensional square lattice has $n^2 = 200^2$ points and so the axes in the figure are discretised into intervals of $h = 0.02$. The interaction constant is $g = 1[\text{d.u.}]$, the angular frequencies are $\omega_x = \omega_y = 100[\text{d.u.}]$ and the particle number is $N = 1000$.

rotation and is known as the *vortex core*. Since vortices are experimentally considered in three dimensions, the centre may also be referred to as a *vortex line*. This term originates from the idea that the rotation occurs about a line in three-dimensional space. The simulations carried out in this thesis may be considered as perpendicular cross-sections of such vortex lines. The azimuthal distance between the vortex core and the bulk density of the condensate is known as the *vortex radius* and it is proportional to the healing length mentioned in section 4.6. This implies that vortex characteristics are sensitive to changes in the system parameters; such as changes in the interaction constant, g . [17]

5.2 Trapped Real-Time Evolution of Simple Systems

Now that we know how the quantum vortices are induced in our system, let us look at their real-time behaviour. This section will focus on the *trapped* real-time evolution of systems with small numbers of distinct vortices.

5.2.1 Central Vortex in an Isotropic Potential

The first case to consider, to check that everything is working as expected, is naturally, the central vortex in an isotropic potential. Due to the radial symmetry of this configuration, the system is already in a stable state. Therefore, we would not expect the density profile to change in real time. However, we would expect the phase to start to rotate about the origin. This is indeed what is observed, as shown in figure 5.3. In this figure, the density and phase profiles have not been cropped, so that we can clearly see the numerical effects outside of the bulk condensate boundary. The density profile does not reveal much, as the density is simply very low outside the bulk, as expected. The phase profile, however, shows that there are reflections from the lattice boundary. These reflections are very minor, since the magnitude of the wavefunction near the lattice boundary⁵ is deliberately

⁴This applies to all of the two-dimensional simulations produced in this thesis, unless explicitly stated otherwise.

⁵Note that figure 5.3 shows a zoomed-in section of the full lattice.

made extremely small (*i.e.* $|\Psi|^2 \sim 10^{-50}$ [d.u.]), so the density is simply given by the numerical noise and these artificial effects do not interfere with the physics of the system. As one would expect with a vortex, all the particles are rotating about the vortex core. For simple systems, it is an easy task to analytically examine the rotation of the system.

Let us start by defining a general three-dimensional position vector, $\mathbf{r} \in \mathbb{R}^3$, in ellipsoidal polars, such that

$$\mathbf{r} \equiv \begin{pmatrix} x \\ y \\ z \end{pmatrix} = \begin{pmatrix} ar \sin \theta \cos \phi \\ br \sin \theta \sin \phi \\ cr \cos \theta \end{pmatrix}, \quad (5.2)$$

where $r \in [0, 1]$ is the scaled radial distance, $\theta \in [0, \pi]$ is the polar angle, $\phi \in [0, 2\pi]$ is the azimuthal angle and $a, b, c > 0$ are the characteristic tri-axial ellipsoid axis lengths defined in figure 1.1. Now, evaluating the magnitude of the Jacobian determinant for this general case leaves us with

$$\|\mathbf{J}\| = \begin{vmatrix} \partial_r x & \partial_\theta x & \partial_\phi x \\ \partial_r y & \partial_\theta y & \partial_\phi y \\ \partial_r z & \partial_\theta z & \partial_\phi z \end{vmatrix} = abc \cdot r^2 |\sin \theta|, \quad (5.3)$$

and so the total orbital angular momentum vector for the condensate, \mathbf{L} , may be expressed as

$$\mathbf{L} = \mathbf{r} \times \mathbf{p} = abc \iiint m\rho(\mathbf{r}) (\mathbf{r} \times \mathbf{v}) r^2 |\sin \theta| dr d\theta d\phi, \quad (5.4)$$

where the integration is carried out across the whole condensate, with \mathbf{p} and \mathbf{v} being the linear momentum and velocity vectors of the condensate, respectively. Since we know that the linear velocity vector is azimuthal and the position vector is radial in our two-dimensional set-up, we know that the cross product of the two will be in the positive z -direction for our coordinate system. We may consequently express the condensate position vector as $\mathbf{r} = r\hat{\mathbf{e}}_r$ and the condensate velocity vector as $\mathbf{v} = v\hat{\mathbf{e}}_\phi$, where $\hat{\mathbf{e}}_r$ and $\hat{\mathbf{e}}_\phi$ are the unit vectors in the r and ϕ -directions, respectively. Noting that the Thomas-Fermi density distribution has the form

$$\rho(\mathbf{r}) = \rho_0 \left(1 - \frac{x^2}{a^2} - \frac{y^2}{b^2} - \frac{z^2}{c^2} \right) \quad (5.5)$$

and when integrated yields

$$\int \rho(\mathbf{r}) dr = \frac{8\pi}{15} \rho_0 abc = N, \quad (5.6)$$

we may subsequently evaluate equation (5.4) using the circulation result (2.28) shown in section 2.3.

In this case, the total orbital angular momentum of the condensate is given by

$$\mathbf{L} = N\hbar l \hat{\mathbf{e}}_z, \quad (5.7)$$

where $l \in \mathbb{Z}$ is the orbital angular momentum quantum number (see appendix A.6 for a full derivation). This shows that the magnitude of the orbital angular momentum per particle is quantized into multiples of \hbar . This follows directly from the concept of quantized rotations discussed earlier. The orbital angular momentum of a single boson, \mathbf{L}_B , may therefore (on average) be given by

$$\mathbf{L}_B = m_B(\mathbf{r} \times \mathbf{v}_B) = \hbar l \hat{\mathbf{e}}_z \quad \Rightarrow \quad \mathbf{v}_B = \frac{\hbar l}{m_B r} \hat{\mathbf{e}}_\phi, \quad (5.8)$$

in cylindrical polars, where \mathbf{v}_B is the linear velocity vector of the boson and m_B is the boson mass. This shows that the azimuthal velocity of the bosons is inversely proportional to their distance away from the vortex core: $v_B \propto 1/r$. [1]

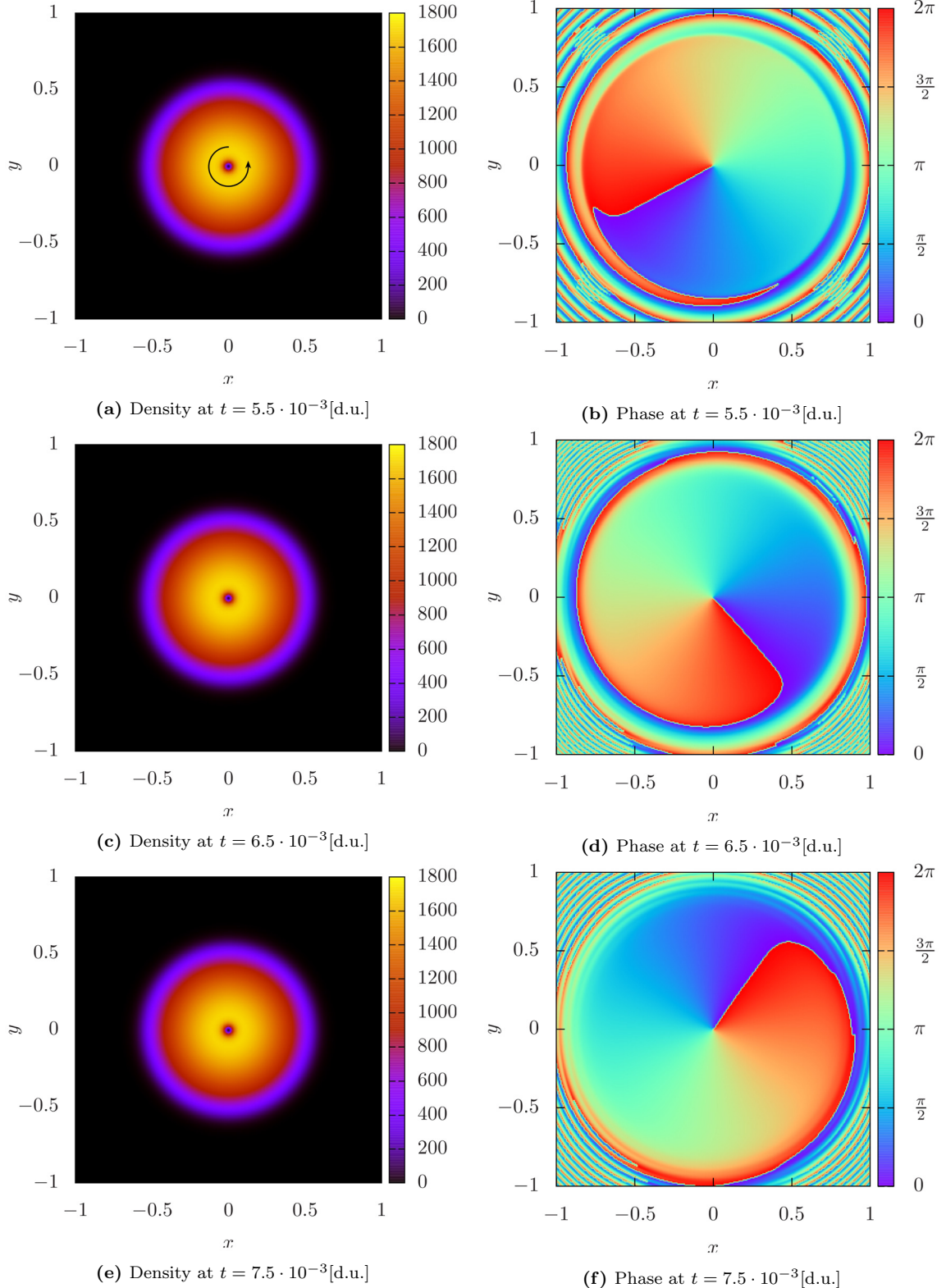


Figure 5.3: Density and phase plots of the real-time evolution of a central vortex in the unnormalised probability density distribution, $|\Psi|^2$, subject to an isotropic potential, in time intervals of 10^{-3} [d.u.]. The total real-time evolution consisted of 10^3 iterations of a 10^{-5} [d.u.] time-step. The square lattice has $n^2 = 200^2$ points and so the axes, which are all defined from -2 to 2, are discretised into intervals of $h = 0.02$. $\{g = 1\text{[d.u.]}, \omega_x = \omega_y = 100\text{[d.u.]}, N = 1000\}$

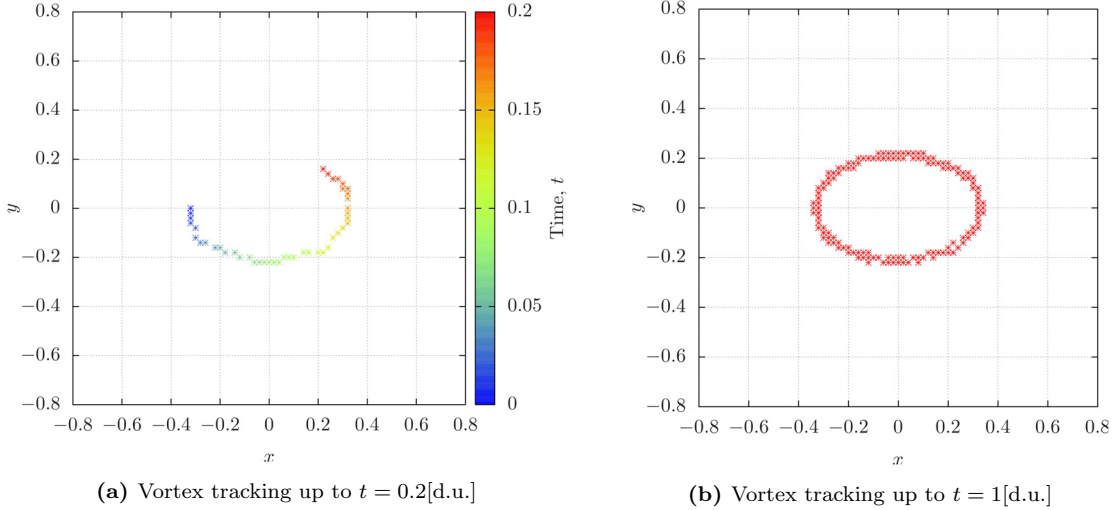


Figure 5.4: Offset vortex tracking plots, in temporal units of 1[d.u.] (for figure 5.5). The total real-time evolution consisted of (a) $2 \cdot 10^4$ iterations and (b) 10^5 iterations of a $10^{-5}[\text{d.u.}]$ time-step. The square lattice has $n^2 = 200^2$ points and so the axes, which are all defined from -2 to 2, are discretised into intervals of $h = 0.02$. $\{g = 1[\text{d.u.}], \omega_x = 100[\text{d.u.}], \omega_y = 150[\text{d.u.}], N = 1000\}$

5.2.2 Offset Vortex in an Anisotropic Potential

The next, more interesting, case to consider is that of an offset vortex in an anisotropic potential. In this situation, the vortex core is positioned so that it is displaced in the negative x -direction and then the system is left to evolve in real time, as before. Figures 5.4 and 5.5 show that the phase of the vortex still rotates about the core; however, on this occasion, the vortex core additionally rotates about the origin of the condensate, in order to conserve orbital angular momentum. Figure 5.4b shows the complete elliptical trajectory traced out by the core⁶. As for the central vortex, it is possible to analyse the rotation of the system. From the vortex motion, we can see that the region within this ellipse is irrotational, such that $\nabla \times \mathbf{v} = \mathbf{0}$ [1]. Therefore, the total rotation of the ground state condensate comes from the region outside of this ellipse and within the Thomas-Fermi radii. The orbital angular momentum of the system is then given by

$$\mathbf{L} = N\hbar l \left(1 - \frac{5}{2}d^3 + \frac{3}{2}d^5\right) \hat{\mathbf{e}}_z, \quad (5.9)$$

where d is the separation between the vortex core and the condensate centre, in terms of the Thomas-Fermi radius. The derivation of this result is similar to that shown in section 5.2.1 for the case of a central vortex; except, on this occasion, the circulation is multiplied by a factor of $\Theta(r - d)$ to account for the fact that the inner ellipse is irrotational⁷ (see appendix A.7 for a full derivation). As for the rotation of the actual vortex, this may be explained using the concept of the field velocity. As shown in section 2.3, the velocity of the bosonic field is proportional to the gradient of the phase. The phase plots of figure 5.5 show that the regions of the condensate further away from the vortex have a mellower phase gradient than the closer regions. For example, notice the large blue area on the left side of the condensate in figure 5.5f. This implies that the velocity of the field is slower further away from the vortex, which results in a non-uniform velocity field. Consequently, the vortex will move in accordance with this velocity gradient. The elliptical symmetry of the trap results in the elliptical trajectory of the vortex core. Therefore, by extension of this argument, if the trap were isotropic, so that the condensate were circular, then the offset vortex trajectory would also be circular. [1]

⁶For more information about the vortex tracking algorithm used to produce these type of plots, refer to appendix B.1.

⁷Here, Θ denotes the Heaviside step function.

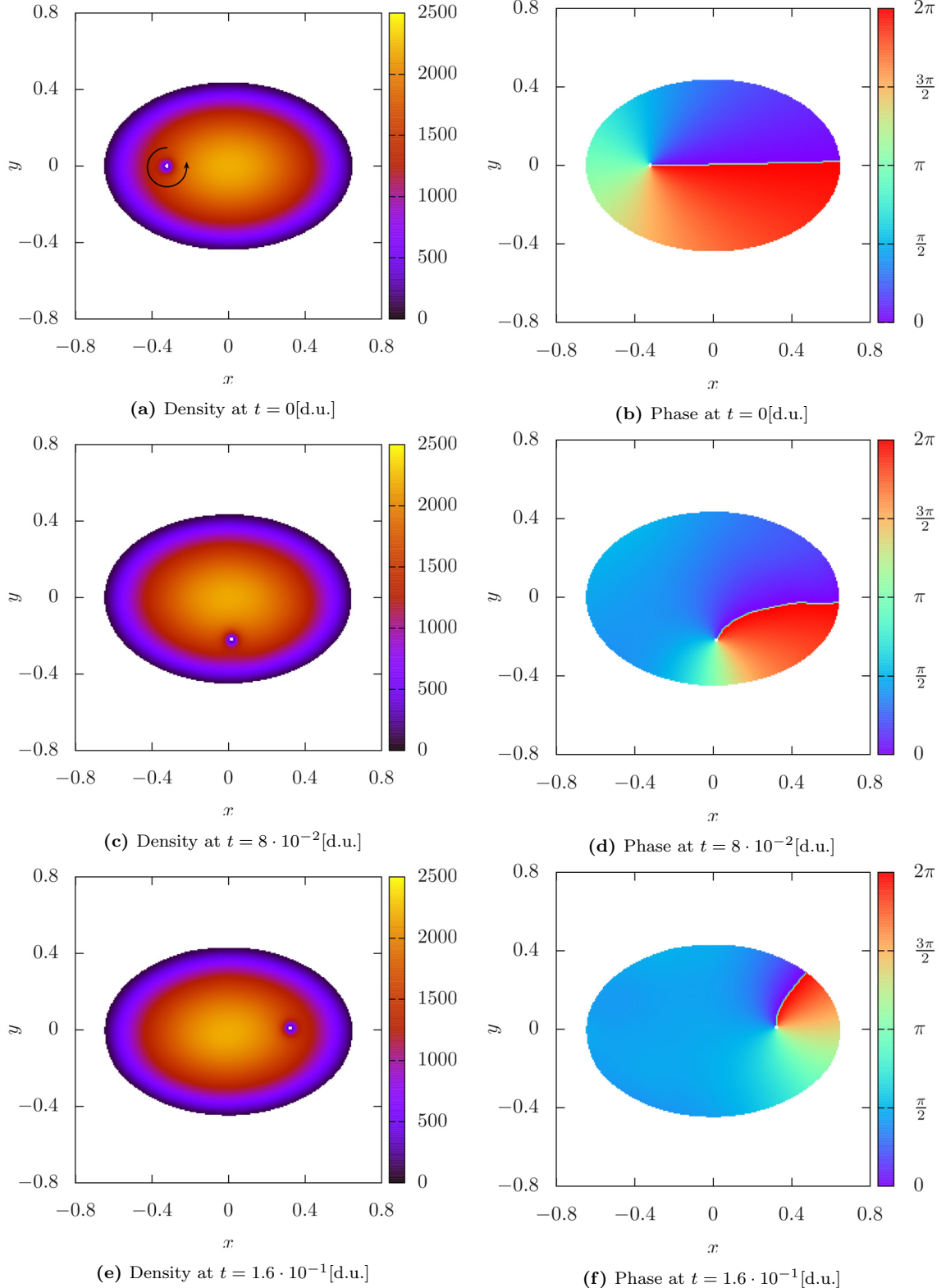


Figure 5.5: Density and phase plots of the real-time evolution of an offset vortex in the unnormalised probability density distribution, $|\Psi|^2$, subject to an anisotropic potential, in time intervals of $8 \cdot 10^{-2}$ [d.u.]. The total real-time evolution consisted of $2 \cdot 10^4$ iterations of a 10^{-5} [d.u.] time-step. The square lattice has $n^2 = 600^2$ points and so the axes, which are all defined from -2 to 2, are discretised into intervals of $h = 1/150$. $\{|\Psi|^2 > 100\text{[d.u.]}, g = 1\text{[d.u.]}, \omega_x = 100\text{[d.u.]}, \omega_y = 150\text{[d.u.]}, N = 1000\}$

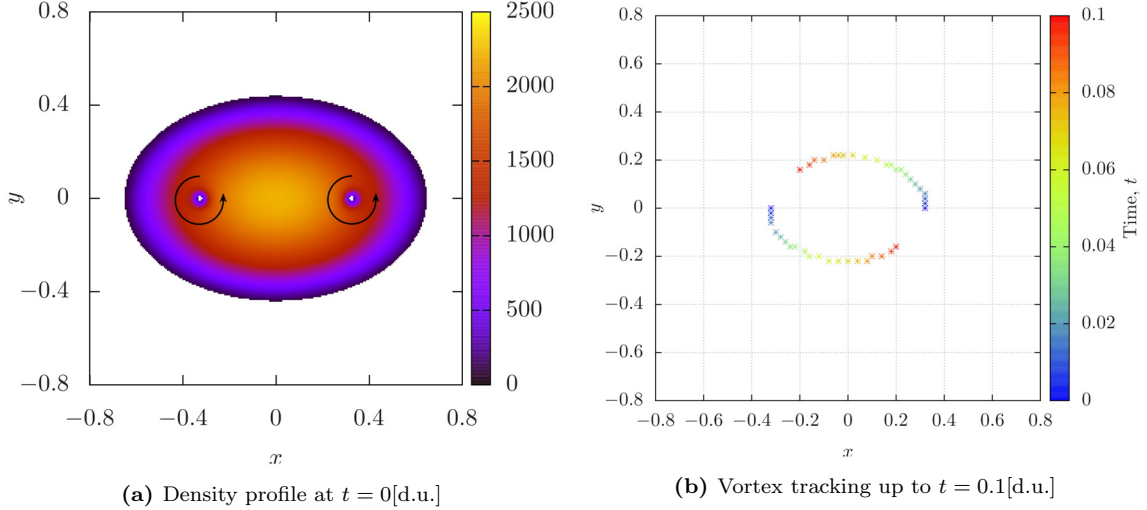


Figure 5.6: (a) Density plot of a pair of identical vortices in the unnormalised probability density distribution, $|\Psi|^2$, subject to an anisotropic potential. The square lattice has $n^2 = 600^2$ points and so the axes, which are all defined from -2 to 2, are discretised into intervals of $h = 1/150$. $\{|\Psi|^2 > 100[\text{d.u.}]\}$ (b) Vortex-vortex pair tracking plot, in temporal units of 1[d.u.] (see figures D.3 and D.4). The total real-time evolution consisted of 10^4 iterations of a $10^{-5}[\text{d.u.}]$ time-step. The square lattice has $n^2 = 200^2$ points and so the axes, which are all defined from -2 to 2, are discretised into intervals of $h = 0.02$. (a,b) $\{g = 1[\text{d.u.}], \omega_x = 100[\text{d.u.}], \omega_y = 150[\text{d.u.}], N = 1000\}$

5.2.3 Vortex Pair Interaction in an Anisotropic Potential

Vortex-Vortex Pair

Now, let us extend our investigations to systems with more than one vortex. Let us start by considering two identical vortices positioned along the x -axis with equal distances away from the condensate centre, as shown in figure 5.6a. The separation from the condensate centre, as well as all the other system parameters, are carried over from the case of the offset vortex in the previous section, to allow for easy comparison. For the offset vortex, we saw that the vortex core followed an elliptical trajectory about the condensate origin. Therefore, for two offset vortices, we would expect a similar sort of behaviour from both, albeit with slightly faster angular velocities. This is indeed the behaviour that is observed, as shown in figure 5.6. Notice that the lower offset vortex ends up at a position of $x \approx 0.2h^{-1}[\text{d.u.}]$ after a time of $t = 0.1[\text{d.u.}]$ in figure 5.6b⁸, whereas the same offset vortex only reaches a position of $x \approx 0.1h^{-1}[\text{d.u.}]$ in the same time, with the absence of the second vortex, in figure 5.4a. This shows that the offset vortices rotate faster when in a vortex-vortex pair configuration. This is to be expected, since we know that the phase profiles of the vortices add linearly and so the phase gradients for each of the vortices is increased. This behaviour could also be intuitively predicted from knowledge of binary orbits in classical mechanics or coupled charges in electrodynamics.

⁸In this context, h denotes the discrete interval length of our spatial grid and is not to be confused with the Planck constant.

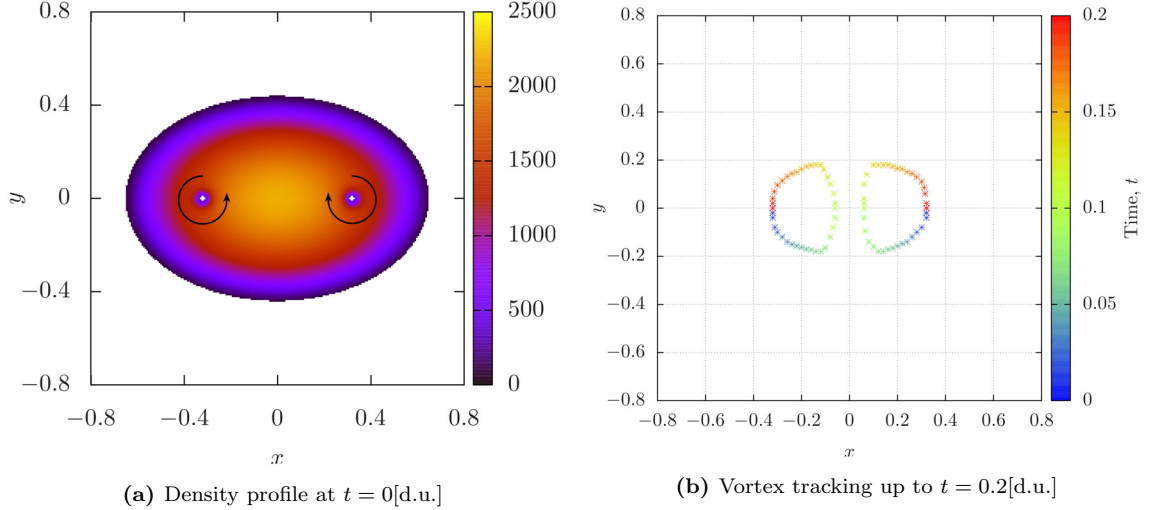


Figure 5.7: (a) Density plot of a vortex-antivortex pair in the unnormalised probability density distribution, $|\Psi|^2$, subject to an anisotropic potential. The square lattice has $n^2 = 600^2$ points and so the axes, which are all defined from -2 to 2, are discretised into intervals of $h = 1/150$. $\{|\Psi|^2 > 100[\text{d.u.}]\}$ (b) Vortex-antivortex pair tracking plot, in temporal units of 1[d.u.] (see figures D.5 and D.6). The total real-time evolution consisted of $2 \cdot 10^4$ iterations of a $10^{-5}[\text{d.u.}]$ time-step. The square lattice has $n^2 = 200^2$ points and so the axes, which are all defined from -2 to 2, are discretised into intervals of $h = 0.02$. (a,b) $\{g = 1[\text{d.u.}], \omega_x = 100[\text{d.u.}], \omega_y = 150[\text{d.u.}], N = 1000\}$

Vortex-Antivortex Pair

To complement the previous section on vortex-vortex pair interaction, it is logical to next consider the dynamics of a vortex-antivortex pair configuration. As before, all the system parameters are kept the same, to allow for a direct comparison. In this system, we replace the right vortex with its equivalent antivortex counterpart, as shown in figure 5.7. Notice that the initial density profile shown in figure 5.7a is indistinguishable from the initial profile of the corresponding vortex-vortex configuration, in figure 5.6a. The vortices have therefore been labeled with arrows, so that it is clear which way they are rotating. This is also clear in the phase plots shown in appendix D.6. On this occasion, the interaction between the vortices is very apparent, as shown in the vortex trajectories in figure 5.7b. Now, due to the ‘mirrored’ rotations of the two vortices, they start by both following the bottom elliptical path. However, when the vortices become sufficiently close to each other, their paths deviate vertically in the positive y -direction. Again, this behaviour is easiest to understand by looking at the phase plots in appendix D.6. The linear velocity is proportional to the phase gradient and so one needs to look at the phase function directly between the two vortices to explain their interaction. For example, when the vortices are at their closest approach (slightly before the image shown in appendix D.6d), the phase directly between the two vortices, along the x -axis, is constant. Therefore, there is no horizontal velocity component at this point. As a result of this phase interaction, we observe the two ‘D-shaped’ trajectories that are symmetrical about the y -axis. Furthermore, we could extend this analysis to look at the three-body problem, where we could also draw many parallels with celestial mechanics. If we then went on to look at a four vortex configuration, we would notice the vortex trajectories’ sensitive dependence on initial conditions and the manifestation of chaotic motion (this is beyond the scope of this thesis) [46].

5.3 Macroscopic Density Fluctuation in an Isotropic Potential

The previous sections in this chapter have mainly focused on simple systems of sparsely populated, distinct quantum vortices. This gives us some intuition for how these vortices move and interact with one another. Let us now turn our attention to a more complex system. By choosing appropriate starting conditions for our Bose gas, it is possible to invoke macroscopic density fluctuations in the condensate, as shown in figure 5.8. This is an interesting phenomenon on many fronts, not least of which because it demonstrates the behaviour of a highly unstable vortex configuration (see appendices D.7 and D.8 for the full development).

First of all, it is interesting to note that this is the first example of *imaginary time readjustment* for the vortices, in this thesis. The initial state (shown in appendix D.7a) was generated by imprinting eight randomly distributed⁹ quantum vortices with extremely small separations around the origin (at the usual point in the imaginary time propagation). In other words, as the vortices form in the density profile, their radii overlap. The positioning of the vortices is irrelevant in the turbulence induction, due to their extreme proximity to one another. As one would expect, this is a highly unstable inception for the vortices. So much so, that during the final 20% of the imaginary time propagation, the vortices readjust themselves into a more energetically stable configuration (shown in appendix D.7a). As explained before, the process of imaginary time propagation moves a system towards its lowest energy state. Therefore, if we deliberately induce a highly unstable vortex configuration during this process, the propagation will begin to rectify this and the vortices will all move into a more energetically favourable configuration. In this case, the more favourable configuration is a radially symmetric, equally-spaced ring of the eight vortices.

The subsequent real-time evolution of this system is shown overleaf. Note that although the vortices have significantly readjusted during imaginary time, they have not yet reached a completely stable configuration. Notice the initial configuration has a high density bump at the centre. Over time, this central region undergoes a damped macroscopic density oscillation, as shown in the density plots in figure 5.8. As before, these density phenomena may be explained by looking at the total phase of the system. The phase in this central region is never rotating which implies that this is not a quantum supervortex. However, note the phase gradient for the central region in figure 5.8b. The phase is high at the origin and then falls with radial distance in a pseudo-Gaussian style. This implies that, initially, there is a phase gradient, and equivalently, a particle flux out of this central region. If we now look at the subsequent density plot (figure 5.8c), then we can see that these particles have moved to form a radial density ripple¹⁰. This ripple then continues to move radially outwards, as shown in the figures. As the number of particles in this central region reduces, this phase gradient (or particle flux) draws in fewer and fewer particles, since there are fewer in the vicinity of the origin. This, in turn, results in the observed damped macroscopic density oscillation.

It is also interesting to note the effect that this radially oscillating particle flux has on the vortex ring. Notice that as the particles are moving out from the centre, the vortices in the ring are stretched radially outwards. By contrast, as the particles flow into the central region, the vortices are squashed inwards. These sorts of oscillating deformations are typical of systems trying to reach equilibrium in a harmonic trapping potential. As the real-time evolution continues, these damped flow oscillations will eventually settle and the density distribution will reach an unstable quasi-stationary state. As suggested by the density profile progression (especially the profile shown in appendix D.7e), the final pseudostable ring configuration of the vortices will most probably have a larger mean separation than the starting ring.

⁹It is arbitrary where the vortices are positioned, so long as they are extremely close to one another and the geometry of the set-up is rendered negligible.

¹⁰Note that the density scale in the second density plot (figure 5.8c) is higher than the scale in the first plot (figure 5.8a).

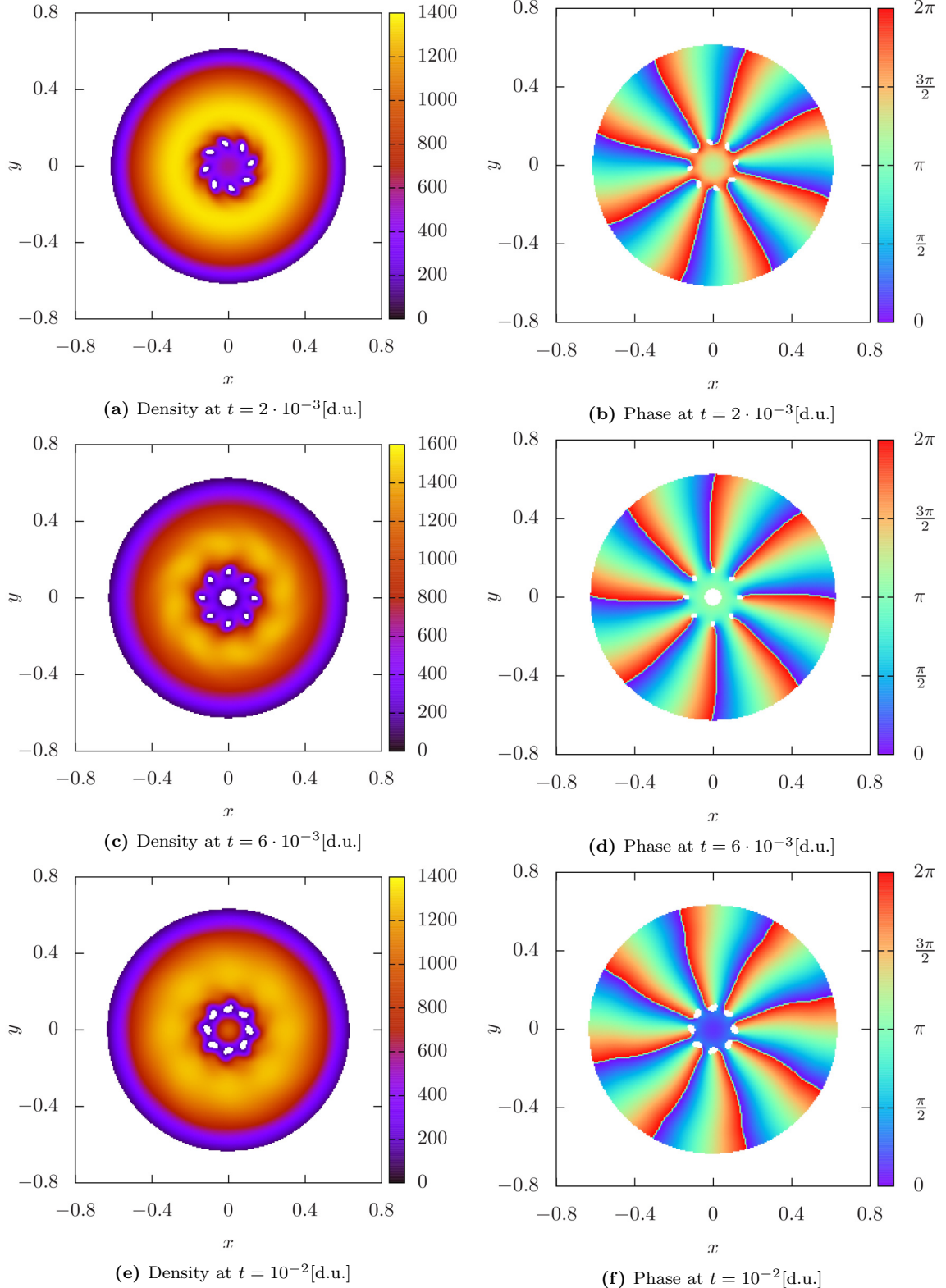


Figure 5.8: Density and phase plots of the evolution of a macroscopic density fluctuation in the unnormalised probability density distribution, $|\Psi|^2$, subject to an isotropic potential, in time intervals of $4 \cdot 10^{-3}$ [d.u.]. The total real-time evolution consisted of 10^3 iterations of a 10^{-5} [d.u.] time-step (see figures D.7 and D.8). The square lattice has $n^2 = 600^2$ points and so the axes, which are all defined from -2 to 2, are discretised into intervals of $h = 1/150$. $\{|\Psi|^2 > 100$ [d.u.], $g = 1$ [d.u.], $\omega_x = \omega_y = 100$ [d.u.], $N = 1000\}$

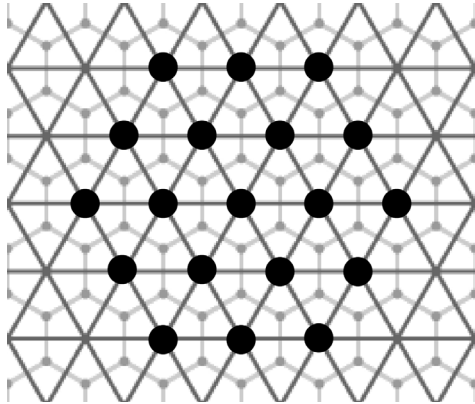


Figure 5.9: Abrikosov lattice of 19 points (as used in figure 5.11).

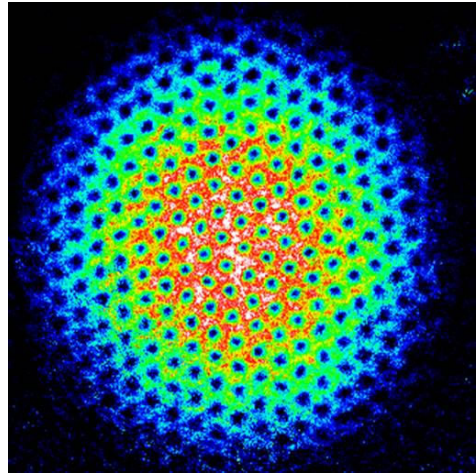


Figure 5.10: False-colour photograph of the experimentally observed density distribution of a turbulent Bose-Einstein condensate with an Abrikosov lattice of over 300 quantum vortices. [49]

5.4 The Abrikosov Lattice

In this section, let us consider the most important and most common quantum vortex configuration: the Abrikosov lattice¹¹ [48]. The Abrikosov lattice is a regular hexagonal¹² lattice of quantum vortices. From geometry, we know that a regular hexagonal lattice may be constructed from the mid-points of tightly-packed circles in a two-dimensional plane. This implies that the separation between neighbouring points in a regular hexagonal lattice is always equal. By extension, we can conclude that an Abrikosov lattice of quantum vortices is the most energetically favourable turbulent state, since all the vortices are the same distance from one another. This explains why these lattice configurations are common in experiments.

Let us now construct an Abrikosov lattice of nineteen quantum vortices, so that we can examine the real-time behaviour. Let us position the vortices in the configuration shown in figure 5.9. Normally, in experiments, one would expect a much greater number of vortices in the lattice (as shown in figure 5.10); however, for the purposes of this investigation, a smaller lattice is quicker to program and should yield equivalent results. Figure 5.11 shows the anatomy of the fully developed turbulent state. Note that the two-dimensional density map shown in figure 5.11a has the same vortex geometry as the lattice in figure 5.9. This is also reflected in the phase plot, figure 5.11b. Notice that the phase always wraps around by 2π around the vortex cores. This is a unique way of identifying the vortices in more complex systems. The three-dimensional density mesh plot in figure 5.11c clearly shows that all of the vortices are fully developed. Note the paraboloidal, Thomas-Fermi envelope of the density distribution in this figure. Although the vortices greatly distort the shape of the density profile in this case, the Bose gas has still been propagated through the same period of imaginary time, as in all the previous cases that we have investigated. The phase rotations were also all imprinted at the same instant in imaginary time. Therefore, the configuration shown here has been given just as much of an opportunity to develop into a stable configuration as all of the other systems. Note that the healing length depicted in this three-dimensional plot is of the order of the one shown in figure 5.2.

¹¹The Abrikosov lattice is named after the Russian theoretical physicist, Alexei Abrikosov. Abrikosov was jointly awarded the Nobel Prize in Physics in 2003 “for pioneering contributions to the theory of superconductors and superfluids” [47].

¹²Note that a regular hexagonal lattice is equivalent to a equilateral triangular lattice, as shown in figure 5.9.

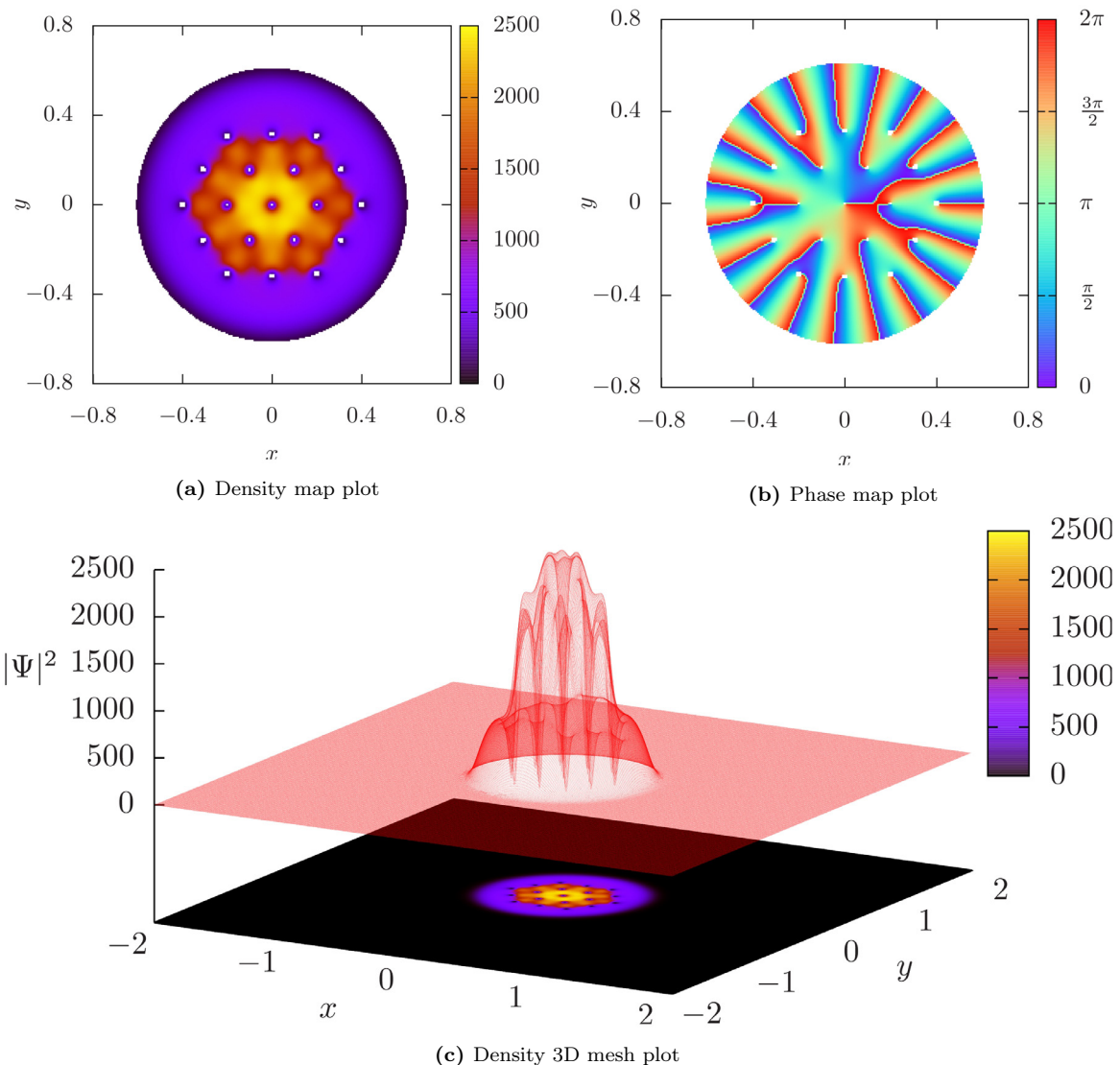


Figure 5.11: The form of a fully developed 19 vortex Abrikosov lattice in the unnormalised probability density distribution, $|\Psi|^2$, subject to an isotropic potential, after imaginary time propagation. The square lattice has $n^2 = 600^2$ points and so the axes, which are all defined from -2 to 2, are discretised into intervals of $h = 1/150$. $\{g = 1[\text{d.u.}], \omega_x = \omega_y = 100[\text{d.u.}], N = 1000, (\mathbf{a}, \mathbf{b}) |\Psi|^2 > 100[\text{d.u.}]\}$

5.5 Trapped Real-Time Evolution of an Abrikosov Lattice

Let us now take the initial configuration shown in figure 5.11 and look at its trapped real-time evolution (figure 5.12). Theoretically speaking, if we start with an energetically stable lattice of quantum vortices in a ground state condensate, then we would not expect much to happen during trapped real-time evolution. All that would be expected is the rotation of the condensate and the vortex lattice through the system's continuum of degenerate rotational eigenstates. However, as depicted in figure 5.12, an unanticipated phenomenon occurs at the beginning. Shortly after the trap is switched off, the condensate expands to take the shape of the hexagonal lattice and then contracts back down to another Abrikosov configuration. This is due to the fact that the condensate is *not* a perfect ground state at $t = 0$ and additionally, the mean separation of the vortices is not optimal. At the beginning of the real-time evolution, the condensate consequently oscillates to readjust itself. This expansion-contraction oscillation continues until the condensate reaches a stable configuration, after which, the expected behaviour of a trapped Abrikosov lattice ensues.

5.6 Trapped Real-Time Evolution of Anisotropic Vortex Lattices

Isotropic examples of Abrikosov lattice configurations are indeed instructive to examine, however the condensates used by *Bagnato et al.* in their experiments were ellipsoidal and the turbulent states were not well defined. This section, therefore, focuses on the elliptically-trapped, real-time evolution of turbulent condensates with anisotropic vortex lattices.

5.6.1 Vortex Lattice in an Anisotropic Potential

First of all, let us look at the initial configuration of nineteen identical vortices shown in figure 5.13a. The initial and final states of the real-time evolution are shown in figure 5.13 (see appendices D.9 and D.10 for the full development). Here, we have used a face-centred cubic (fcc) lattice of vortices to match the anisotropy of the condensate. Notice that during the real-time evolution, the vortex lattice rotates anticlockwise along with the condensate, due to the matching orientation of all the vortices¹³. However, the vortex lattice rotates further than the condensate bulk, due to the restoring potential from the magnetic trap. Note also that, as a result of this trap resistance, the bulk boundary of the condensate deforms slightly, as shown in figure 5.13c.

5.6.2 Vortex-Antivortex Lattice in an Anisotropic Potential

Complementing this study with the vortex-antivortex lattice case, we notice a very different behaviour (see figure 5.14). Here, we have arranged the vortices in the condensate so that they are pairwise oppositely-oriented along the horizontal rows. This implies that along lines of constant y , no two neighbouring vortices have the same orientation. Notice that in this case, as with the macroscopic density fluctuation simulation in section 5.3, we see an example of imaginary time readjustment. The vortices and antivortices have partially grouped themselves, as shown in figure 5.14a. Due to the horizontal vortex-antivortex pairs along the fcc lattice structure, this ‘grouping’ manifests itself as the arrow-like arrangement shown in the figure. Furthermore, due to the conflicting internal vortex rotations, the condensate does not rotate in this case. Instead, the shape of the bulk condensate deforms slightly as vortices within deform and merge with each other (see appendices D.11 and D.12 for the detailed development). It is impossible to determine the exact vortex configuration of the turbulent condensates used in the experiments of *Bagnato et al.*. However, such vortex-antivortex lattice configurations are highly unlikely to occur from the experimental procedure [43] and so, for the remainder of this report, let us focus our attention on equally-oriented vortex lattices.

¹³The same rotation effect is observed in the trapped Abrikosov lattice evolution, shown in figure 5.11.

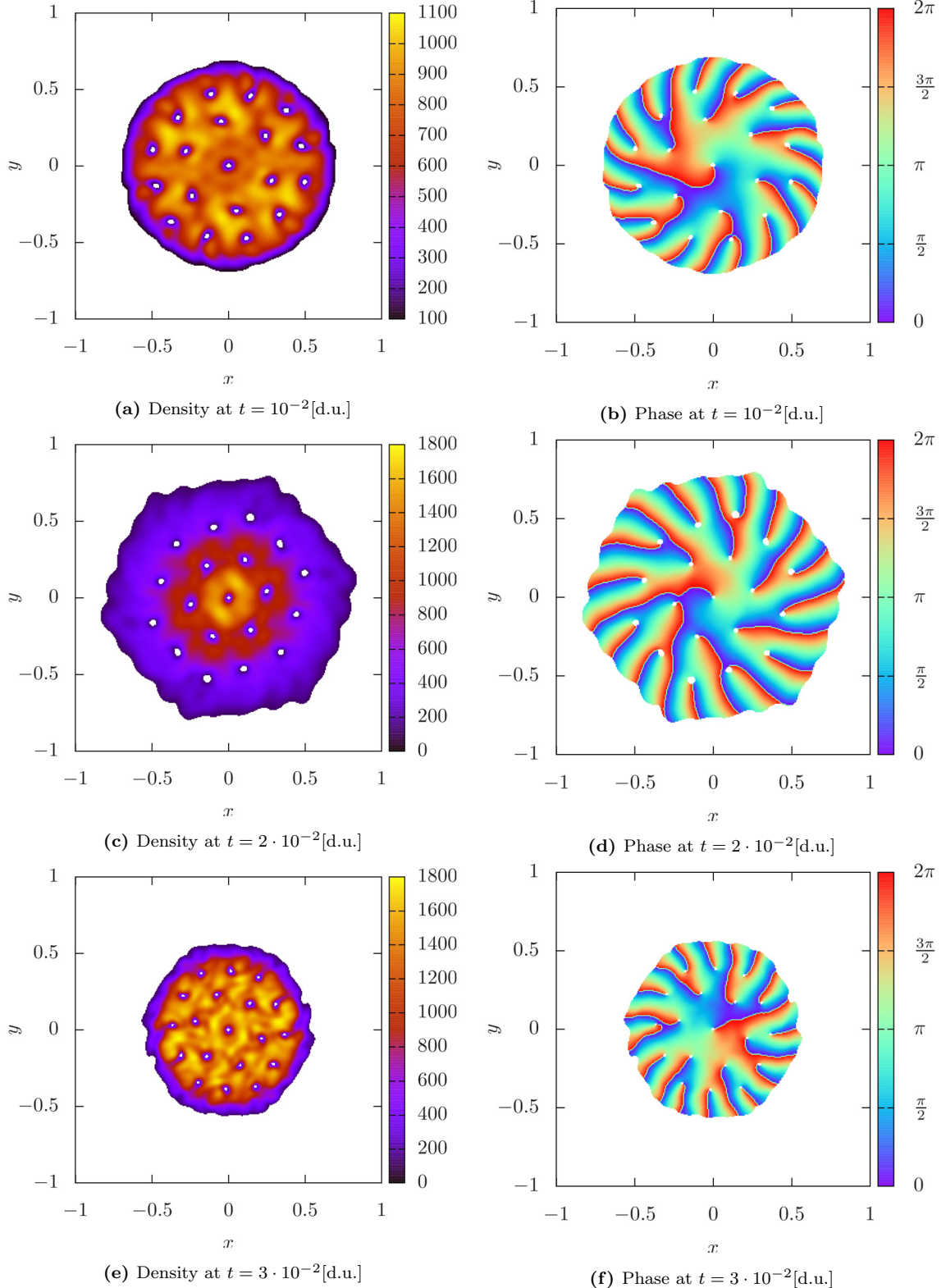


Figure 5.12: Density and phase plots of the real-time evolution of a 19 vortex Abrikosov lattice in the unnormalised probability density distribution, $|\Psi|^2$, subject to an isotropic potential, in time intervals of 10^{-2} [d.u.]. The total real-time evolution consisted of $3 \cdot 10^3$ iterations of a 10^{-5} [d.u.] time-step (the $t = 0$ plot is shown in figure 5.11). The square lattice has $n^2 = 600^2$ points and so the axes, which are all defined from -2 to 2, are discretised into intervals of $h = 1/150$. $\{|\Psi|^2 > 100\text{[d.u.]}, g = 1\text{[d.u.]}, \omega_x = \omega_y = 100\text{[d.u.]}, N = 1000\}$

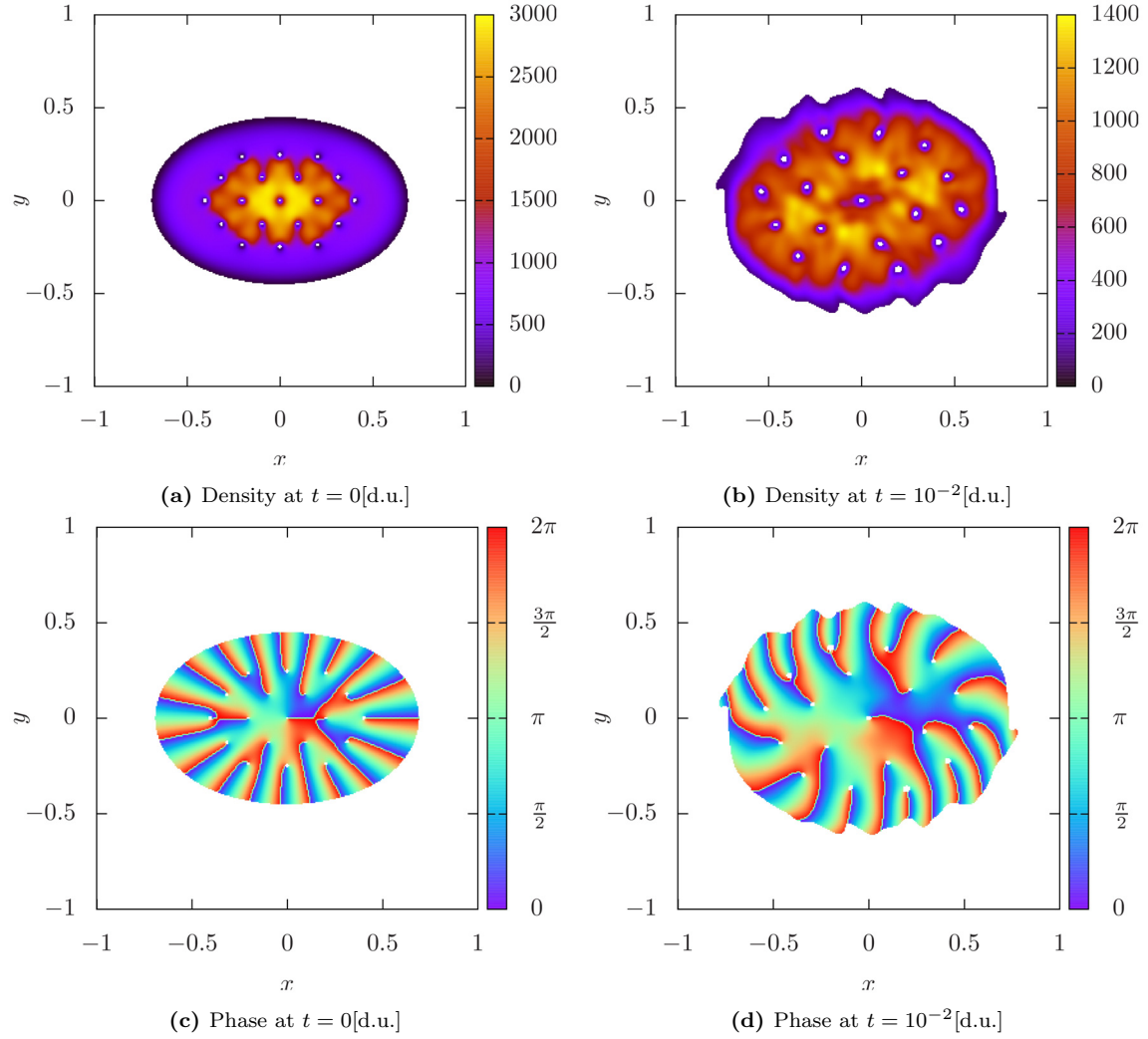


Figure 5.13: Density and phase plots of the real-time evolution of an fcc lattice of 19 identical vortices in the unnormalised probability density distribution, $|\Psi|^2$, subject to an anisotropic potential, in time intervals of 10^{-2} [d.u.]. The total real-time evolution consisted of 10^3 iterations of a 10^{-5} [d.u.] time-step (see figures D.9 and D.10). The square lattice has $n^2 = 600^2$ points and so the axes, which are all defined from -2 to 2, are discretised into intervals of $h = 1/150$. $\{|\Psi|^2 > 100\text{[d.u.]}, g = 1\text{[d.u.]}, \omega_x = 100\text{[d.u.]}, \omega_y = 150\text{[d.u.]}, N = 1000\}$

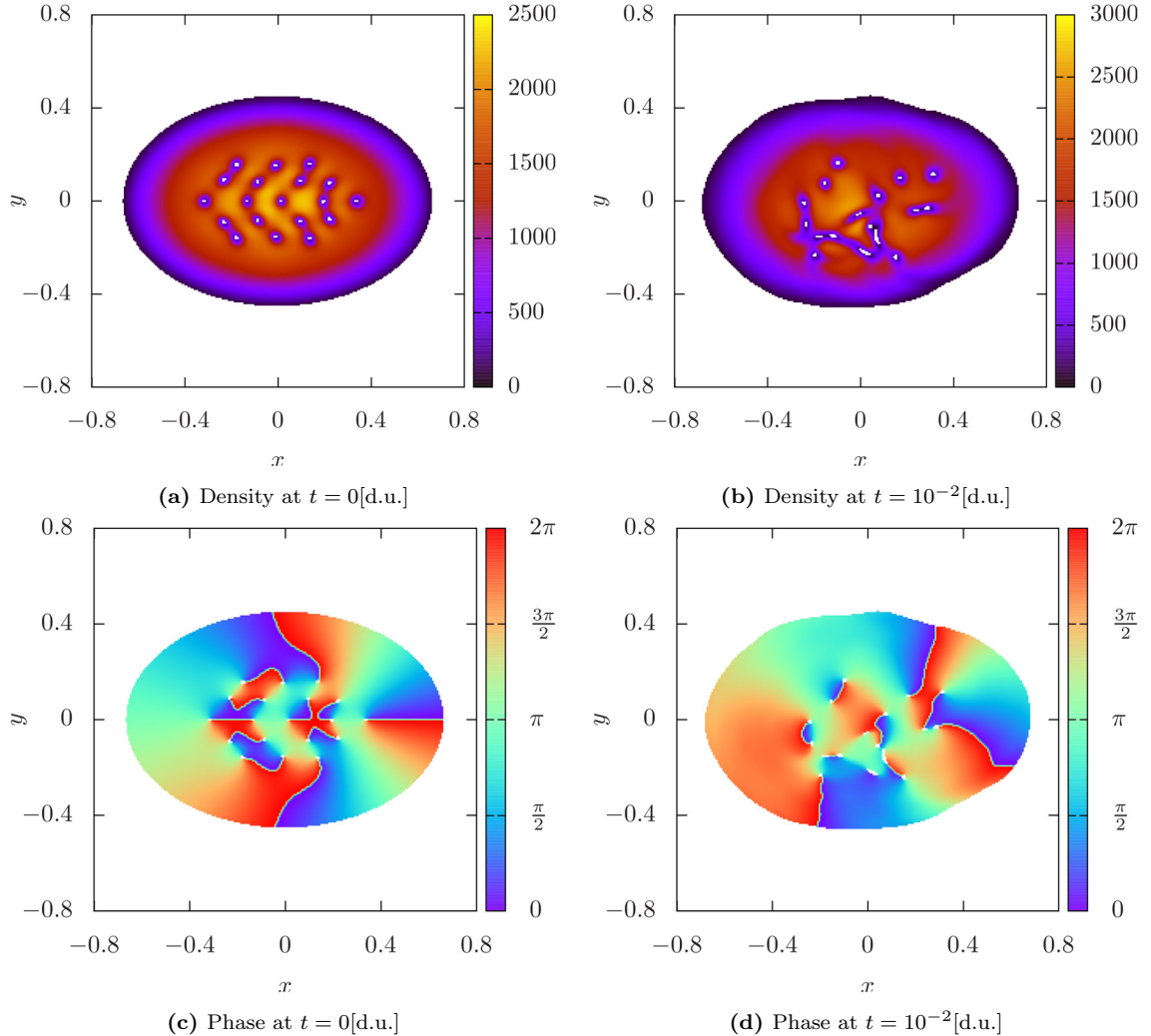


Figure 5.14: Density and phase plots of the real-time evolution of an fcc vortex-antivortex lattice in the unnormalised probability density distribution, $|\Psi|^2$, subject to an anisotropic potential, in time intervals of 10^{-2} [d.u.]. The total real-time evolution consisted of 10^3 iterations of a 10^{-5} [d.u.] time-step (see figures D.11 and D.12). The square lattice has $n^2 = 600^2$ points and so the axes, which are all defined from -2 to 2, are discretised into intervals of $h = 1/150$. $\{|\Psi|^2 > 100\text{[d.u.]}, g = 1\text{[d.u.]}, \omega_x = 100\text{[d.u.]}, \omega_y = 150\text{[d.u.]}, N = 1000\}$

Two-Dimensional Expansion Dynamics

So far, we have discussed how it is possible to simulate the cooling and trapping of a gas as well as the turbulence induction. We have seen how we can use imaginary time propagation to evolve a system into its ground state and we have shown how symmetric phase rotations mimic the behaviour of quantum vortices. Once we have our trapped turbulent Bose-Einstein condensate, all that is left to do is to turn off the trap and observe the free expansion. Unfortunately, due to numerical considerations, this stage is not as easy in practice as it sounds in theory. The main problem that we face, is the fact that we are trying to simulate expansion on a finite lattice. Naturally, as the condensate expands, there will come a point when the condensate wavefunction hits the lattice border. As mentioned before with imaginary time propagation, this can lead to reflections, interference and discontinuities in the density and phase profiles. However, with real-time expansion, this is a much bigger issue because the whole condensate is spreading. Before, we imposed boundary conditions on the lattice border to take care of the unwanted ripple effects. In this situation, however, boundary conditions alone are not enough to resolve the issue. To solve this problem we could do one of two things: either we could use a very large lattice size with a high resolution so that our condensate has enough room to expand, or we could carry out our simulations in an expanding coordinate system. The prior option, although easier to implement, is not viable because the computation times required would be inordinately large. It would also be a very inefficient process because the computer would have to calculate a lot of unnecessary lattice points early on in the simulation. Instead, we shall use an expanding reference frame to solve this problem. The aim of this chapter is to introduce the concept of an expanding coordinate system and to transform the time-dependent GPE to this expanding frame. Following on from this, we will then investigate the free expansion of two-dimensional condensates in a variety of turbulent states.

6.1 The Expanding Coordinate System

The main aim of the expanding coordinate system is to have a lattice that expands at the same rate as the condensate. This implies that the distance between the lattice points (*i.e.* our lattice constants) will now be functions of time:

$$\begin{aligned} h_x(t) &= \lambda_x(t)h_x(0), \\ h_y(t) &= \lambda_y(t)h_y(0). \end{aligned} \tag{6.1}$$

Here, $\lambda_x(t)$ and $\lambda_y(t)$ are strictly increasing monotonic functions that determine the rate of coordinate expansion. For our derivation, however, let us consider a more general case.

Let us consider the coordinate transformation from $\mathbf{x} \rightarrow \mathbf{x}'$ due to an increasing monotonic expansion matrix, $\Lambda(t)$, at some later time $t = t'$, such that

$$\mathbf{x}' = \Lambda(t')\mathbf{x}, \tag{6.2}$$

where $\Lambda(t)$ denotes an invertible diagonal expansion matrix given by

$$\Lambda(t) \equiv \begin{pmatrix} \lambda_x(t) & 0 & \cdots & 0 \\ 0 & \lambda_y(t) & \cdots & 0 \\ \vdots & \vdots & \ddots & \vdots \\ 0 & 0 & \cdots & \lambda_D(t) \end{pmatrix}. \quad (6.3)$$

In this derivation, the coordinate systems represent general orthogonal curvilinear coordinate systems in D dimensions. We also need to bear in mind that the initial condition on our expansion factor demands that $\Lambda(0) = \mathbf{I}$, since our two coordinate systems are trivially identical at $t = 0$.

The next step in our transformation is to convert the time-dependent GPE. In order to do this, we need to examine how the wavefunction and its derivatives transform. The transformation of the wavefunction itself is trivial and is given by

$$\Psi'(\mathbf{x}', t) = \Psi(\mathbf{x}, t). \quad (6.4)$$

The time-derivative transformation, however, is slightly more involved. For clarity, let us now just consider the expansion of one axis; for instance, the x -axis. Note that this equally applies to any axis, since we are dealing with orthogonal coordinates. The time-derivative transform may now be evaluated as follows:

$$\frac{\partial \Psi(x, t)}{\partial t} = \frac{\partial \Psi'(\lambda_x(t)x, t)}{\partial t} + \frac{\partial \Psi'(\lambda_x(t)x, t)}{\partial \lambda_x} \frac{d\lambda_x}{dt}. \quad (6.5)$$

Here, we have used the product rule to expand out the time-derivative in the expanding frame. The derivative on the left of equation (6.5) is simply concerned with the inherent time dependence of the wavefunction, whereas the time-derivative in the expanding frame has to also take into account the time dependence of the coordinate system. Continuing this evaluation yields

$$\begin{aligned} \partial_t \Psi(x, t) &= \partial_t \Psi'(x', t) + \partial_{\lambda_x} \Psi'(x', t) \dot{\lambda}_x \\ &= \partial_t \Psi'(x', t) + \frac{\partial \Psi'(x', t)}{\partial x'} \frac{\partial x'}{\partial \lambda_x} \dot{\lambda}_x \\ &= \partial_t \Psi'(x', t) + \dot{\lambda}_x x \frac{\partial \Psi(x, t)}{\partial x} \frac{\partial x}{\partial x'} \\ &= \partial_t \Psi'(x', t) + \frac{\dot{\lambda}_x}{\lambda_x} x \frac{\partial \Psi(x, t)}{\partial x} \\ \Rightarrow \partial_t \Psi'(x', t) &= \partial_t \Psi(x, t) - \frac{\dot{\lambda}_x}{\lambda_x} x \partial_x \Psi(x, t). \end{aligned} \quad (6.6)$$

If we generalise this equation back into an arbitrary number of spatial dimensions, then we arrive at

$$\frac{\partial \Psi'(\mathbf{x}', t)}{\partial t} = \frac{\partial \Psi(\mathbf{x}, t)}{\partial t} - (\dot{\Lambda} \Lambda^{-1} \mathbf{x}) \cdot \nabla \Psi(\mathbf{x}, t). \quad (6.7)$$

Now, if we perform a similar transformation for the spatial derivative in one dimension, then we obtain

$$\begin{aligned} \frac{\partial \Psi(x, t)}{\partial x} &= \frac{\partial \Psi'(x', t)}{\partial x} \\ &= \frac{\partial \Psi'(x', t)}{\partial x'} \frac{\partial x'}{\partial x} \\ &= \lambda_x \partial_{x'} \Psi'(x', t) \\ \Rightarrow \partial_{x'} \Psi'(x', t) &= \frac{\partial_x \Psi(x, t)}{\lambda_x}. \end{aligned} \quad (6.8)$$

Applying the spatial derivative twice and converting back into D dimensions then yields

$$\begin{aligned}\nabla'^2\Psi'(\mathbf{x}',t) &= \frac{\partial_x^2\Psi(\mathbf{x},t)}{\lambda_x^2} + \frac{\partial_y^2\Psi(\mathbf{x},t)}{\lambda_y^2} + \dots \\ &= (\boldsymbol{\Lambda}^{-2}\mathbf{1}) \cdot \nabla^2\Psi(\mathbf{x},t),\end{aligned}\quad (6.9)$$

where $\mathbf{1} = \sum_{i=1}^D \hat{\mathbf{e}}_i$ is a D -dimensional vector of all ones. Last of all, we note that the external potential function in the GPE may trivially transform as

$$V'(\mathbf{x}',t) = V(\mathbf{x},t). \quad (6.10)$$

At this point, we can use the results from (6.4), (6.7), (6.9) and (6.10) to rewrite our standard time-dependent GPE (2.21) in an expanding frame. Normally, we would now re-derive the equation, as before, however we may use our result from (2.21) to, instead, apply a direct transformation. Rewriting the standard GPE in terms of the new coordinate system yields

$$\left[-\frac{\hbar^2}{2m} \nabla'^2 + V'(\mathbf{x}',t) + g|\Psi'(\mathbf{x}',t)|^2 \right] \Psi'(\mathbf{x}',t) = i\hbar \frac{\partial\Psi'(\mathbf{x}',t)}{\partial t}, \quad (6.11)$$

which after the substitutions and rearrangement becomes

$$\left[-\frac{\hbar^2}{2m} \{ \boldsymbol{\Lambda}^{-2}(t)\mathbf{1} \} \cdot \nabla^2 + V(\mathbf{x},t) + g|\Psi(\mathbf{x},t)|^2 + i\hbar \{ \dot{\boldsymbol{\Lambda}}(t)\boldsymbol{\Lambda}^{-1}(t)\mathbf{x} \} \cdot \nabla \right] \Psi(\mathbf{x},t) = i\hbar \frac{\partial\Psi(\mathbf{x},t)}{\partial t}.$$

This is the final result for the time-dependent GPE in an expanding reference frame¹. In a more compact form it may be expressed as

$$\left[-\frac{\hbar^2}{2m} (\boldsymbol{\Lambda}^{-2}\mathbf{1}) \cdot \nabla^2 + V + g|\Psi|^2 + i\hbar(\dot{\boldsymbol{\Lambda}}\boldsymbol{\Lambda}^{-1}\mathbf{x}) \cdot \nabla \right] \Psi = i\hbar\partial_t\Psi$$

(6.12)

Before we proceed, it is important to check the most important properties of this expanding space. As shown in appendix A.8, the norms are equivalent in the stationary and expanding frames, such that $\langle \Psi(\mathbf{x},t) | \Psi(\mathbf{x},t) \rangle \equiv \langle \Psi'(\mathbf{x}',t) | \Psi'(\mathbf{x}',t) \rangle$. Furthermore, appendix A.9 shows that the particle number is always conserved, and so $\partial_t N = \partial_t \langle \Psi | \Psi \rangle = \partial_t \langle \Psi' | \Psi' \rangle = 0$ [51]. Therefore, we have now set-up a new framework in which to perform our calculations. The physics, in this situation, is naturally frame independent. However, the adaptive expanding reference frame drastically reduces computation times².

Now, all that is left, is to choose a suitable expansion matrix for our frame. Based on the theoretical analysis of expanding condensates carried out in section 2.4.2, it is reasonable for us to choose the dispersion relation for Gaussian-like condensates (2.44) as our expansion function. In two dimensions, our expansion matrix therefore takes the form:

$$\boldsymbol{\Lambda}_{2D}(t) \equiv \begin{pmatrix} \sqrt{1+\omega_x^2 t^2} & 0 \\ 0 & \sqrt{1+\omega_y^2 t^2} \end{pmatrix} \quad \text{with} \quad \dot{\boldsymbol{\Lambda}}_{2D}(t) \equiv \begin{pmatrix} \frac{\omega_x^2 t}{\sqrt{1+\omega_x^2 t^2}} & 0 \\ 0 & \frac{\omega_y^2 t}{\sqrt{1+\omega_y^2 t^2}} \end{pmatrix}. \quad (6.13)$$

In practice, our condensate is not of a Gaussian form when it starts its real-time expansion, but rather takes the approximate form of a Thomas-Fermi paraboloid. However, the dispersion relations for these two radially symmetric functions are sufficiently similar for this matrix to work very well (as demonstrated by the numerical results). [1] [51]

¹Note that, due to the product of \mathbf{x} and $\nabla\Psi$ in equation (6.12), we cannot use spectral integration schemes, such as methods involving the Baker-Campbell-Hausdorff formula, to solve the differential equation [50].

²Naturally, evolving a system in an expanding frame, starting from the same initial grid, will be slower than evolving a system in a fixed grid. However, in a fixed system, a very large grid would be needed for accurate long-time expansions. This would be far slower than the equivalent accurate expanding frame evolution.

6.2 Isotropic Central Vortex Free Expansion

Now, as for trapped systems, let us start by looking at the case of a central vortex. In this scenario, the condensate was confined by an isotropic potential during imaginary time propagation; in the same trap configuration that was used in section 5.2.1. After this, the trap is suddenly switched off so that we can observe the free expansion (shown in figure 6.1)³.

Note that the free expansion is carried out in an expanding reference frame, as with all the simulations in this chapter. The density plots have not been cropped in this figure, so that it is clear to see the grid that the computer is actually evaluating. Since the expansion of the condensate is isotropic, the x and y -axes also expand at the same rate. Note that the 600×600 grid represents an approximately $4^2 h^{-2} [\text{d.u.}]$ area of real space in figure 6.1a, whereas the same 600×600 grid represents an area of almost $6^2 h^{-2} [\text{d.u.}]$ by figure 6.1e. Since the coordinates adapt to the size of the condensate, the actual resolution of the condensate remains approximately constant.

Judging by the density plots alone, the free expansion of a central vortex looks very similar to the corresponding trapped real-time evolution (shown in figure 5.3). Naturally, the whole condensate is expanding in this case; however, other than this, the vortex configuration is still stable and radially symmetric. The phase plots, on the other hand, look very different from before. The phase plots in figure 6.1 show a spiraling branch cut, whereas the phase plots for the trapped case (in figure 5.3) showed a straight rotating branch cut. The same rotating phase defect is still in play in both cases. In order to make sense of these plots, it is helpful to imagine what would happen to the trapped phase plots, if they were not confined. As soon as the condensate starts to expand, the phase of the outer ring of the condensate will be slightly shifted with respect to the phase of the inner ring because it is not under the direct influence of the vortex. If one looks at a zoomed-in view of the centre of the phase plots for the expanding condensate, then the similarity to the trapped phase plots is clear. There is still a straight rotator at the centre of each of the expanding phase plots, only in this case, the end of the rotator leaves a ‘phase trail’ behind, within the bulk condensate, as it rotates.

6.3 Free Expansion of Turbulent Anisotropic Condensates

Next, let us look at a more complex system and consider the free counterpart to the fcc vortex lattice evolution, discussed in section 5.6.1. This set-up is now comparable to the one used experimentally. The initial and final states of the free expansion are shown in figure 6.2. As before, the density plots have not been cropped, so as to clearly show the expanding grid. Note that in this case, the aspect ratio of the condensate changes during free expansion and so the x and y -axes expand at different rates (see appendix D.13). The grid, however, is always represented on an equal-aspect graph so that the shape of the condensate is not deformed. As before with the central vortex, the initial state of the nineteen vortex fcc lattice is the same as the trapped initial state (shown in figure 5.13). The time period is also the same as in the trapped system, allowing for a direct comparison. Notice that during free expansion, the vortices separate out to an approximately Abrikosov lattice configuration and the condensate becomes circular. This aspect ratio evolution then continues, as discussed in section 6.4.3. Looking back at the trapped case, it is apparent that this is what the system is trying to progress towards; however, it is unable, due to the magnetic trap. Since all the vortices are rotating the same way, it is understandable (from the simple systems studied in section 5.2) that the whole vortex lattice will also rotate. In addition, the vortices will naturally try to achieve a constant separation from one another to reach an unstable quasi-stationary state. Due to the parameters of the trap, the aspect ratio⁴ of the initial elliptical condensate in figure 6.2a is 1.5. This evolves to approximately 1 by figure 6.2b. As shown later on, this is the first section of an aspect ratio inversion and may be explained from the physics of the situation.

³Note that the plots in this chapter are cropped above different $|\Psi|^2$ values, so as to emphasise the form of the bulk condensate boundary. This is indicated in the corresponding figure captions.

⁴In two dimensions, the aspect ratio of an ellipse is defined as the length of the major axis divided by the length of the minor axis. Consequently, an aspect ratio of one implies a perfect circle.

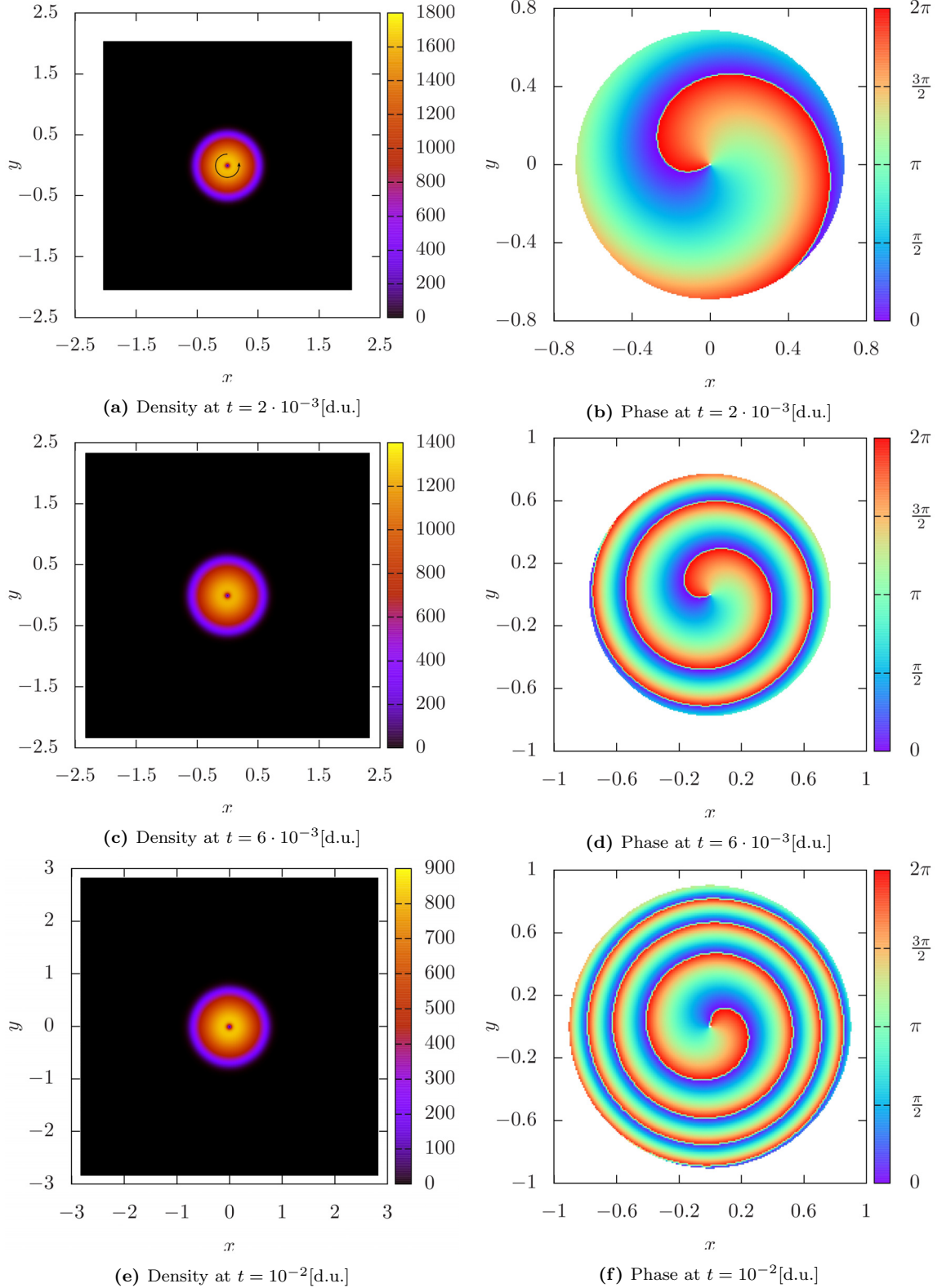


Figure 6.1: Density and phase plots of the real-time expansion of a central vortex in the unnormalised probability density distribution, $|\Psi|^2$, in time intervals of $4 \cdot 10^{-3}$ [d.u.]. The total real-time evolution consisted of 10^3 iterations of a 10^{-5} [d.u.] time-step. Initially, the square lattice had $n^2 = 600^2$ points and so the axes are discretised into intervals of $h = 1/150$. $\{|\Psi|^2 > 1$ [d.u.], $g = 1$ [d.u.], $\omega_x = \omega_y = 100$ [d.u.], $N = 1000\}$

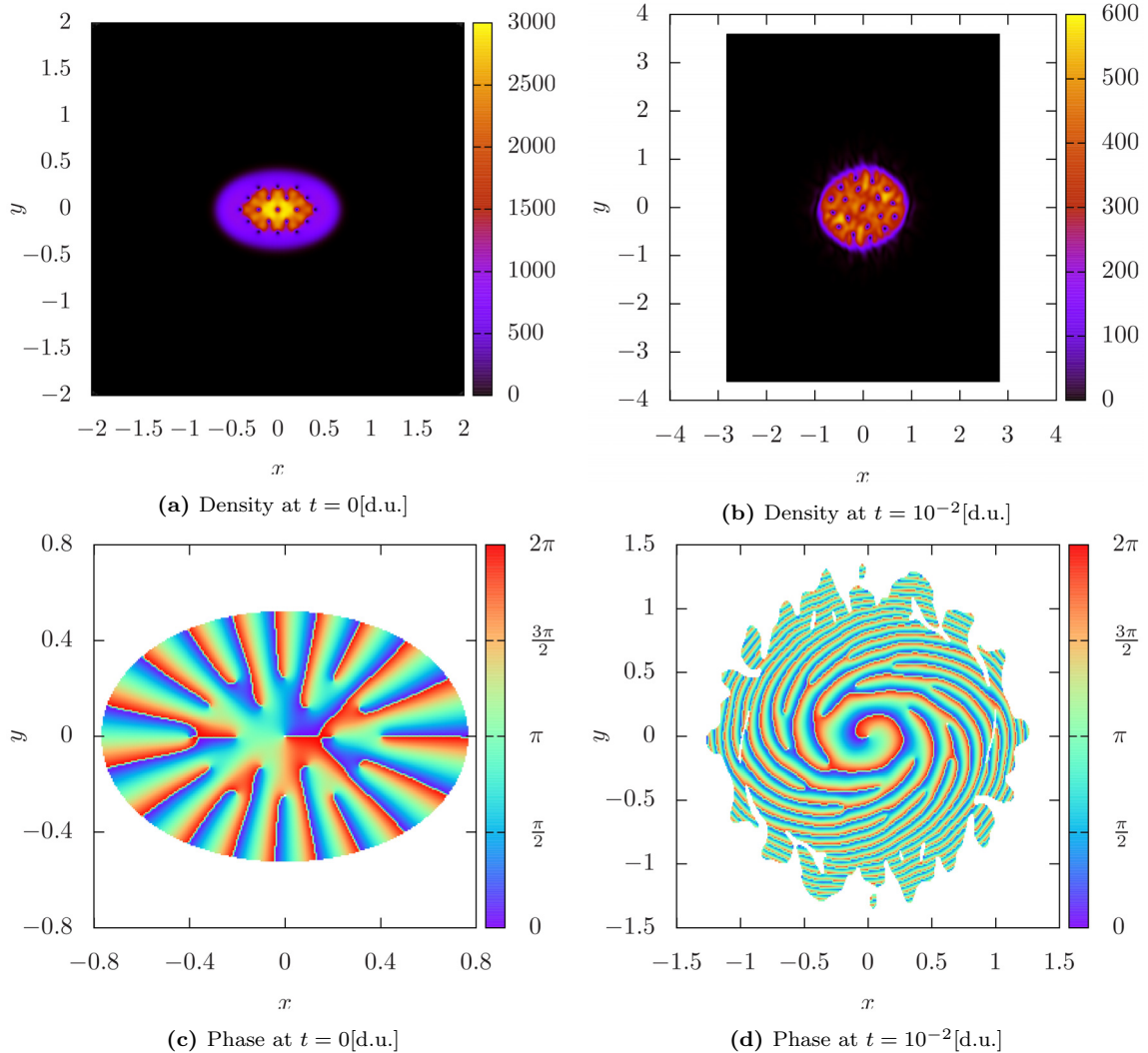


Figure 6.2: Density and phase plots of the real-time expansion of an fcc lattice of 19 identical vortices in the unnormalised probability density distribution, $|\Psi|^2$, in time intervals of 10^{-2} [d.u.]. The total real-time evolution consisted of 10^3 iterations of a 10^{-5} [d.u.] time-step (see figures D.13 and D.14). Initially, the square lattice had $n^2 = 600^2$ points and so the axes are discretised into intervals of $h = 1/150$. $\{|\Psi|^2 > 1$ [d.u.], $g = 1$ [d.u.], $\omega_x = 100$ [d.u.], $\omega_y = 150$ [d.u.], $N = 1000\}$

6.4 Condensate Vortex Density Relations

From the simulations carried out up to this point, we have seen how elliptically trapped condensates with anisotropic vortex lattices freely expand. Based on our current simulations, we know that this free expansion is not equivalent to the self-similar expansion observed by *Bagnato et al.*. However, we do not know the exact vortex configuration present in the Brazilian experiments. Yet, this point is crucial to reproducing the same aspect ratio evolution. As we have clearly seen, the vortex lattice in a condensate has the potential to have a very strong influence on the condensate's shape (see figure 5.12c for a prime example). We, therefore, need to be very careful when choosing our initial lattice configuration. As discussed earlier, a vortex-antivortex lattice is highly unlikely, due to the way the turbulence was induced in the experiment. Equally-oriented vortex lattices (*i.e.* parallel vortex lines) are far more probable, as discussed in section 2.5. We have also seen that the initial positioning of the phase rotations is fairly arbitrary for these lattices⁵, in terms of the total aspect ratio evolution, so long as the vortices are distinct and fairly evenly distributed. However, there is one variable that is still not properly established: vortex density. In this section, we shall look at the effect of vortex density on the turbulent condensate expansion.

In these simulations, let us compare five different cases. For each case, we shall start with an elliptical condensate (as used in the previous section) with an fcc lattice of equally-oriented quantum vortices. All the system parameters, with the exception of the vortex density, will be kept fixed in these trials. Let us consider the cases of 0, 7, 19, 37 and 61 vortices, respectively. The numbers used for the turbulent cases are a direct result of the concentric ‘rings’ in an fcc lattice⁶, *i.e.* a central vortex with a ring of six vortices around it will make up our seven vortex case, *etc.* This is important as it preserves the overall geometry of the system. See figures 6.3a, 6.3c and 6.3e for the $t = 0$ configurations of the 19, 37 and 61-lattices, respectively (the initial state of the 7-lattice configuration is shown in appendix D.15a).

6.4.1 Angular Velocity Evolution

For these five systems, we can then evolve them all for the same period of real time. The initial and final states of the 19, 37 and 61-lattice configurations are shown in figure 6.3 and the full evolutions for all the systems are shown in the corresponding appendices. The first striking feature to notice is the varying degree of lattice rotation. Comparing the initial and final states, it is clear to see that *the higher the vortex density, the faster the rotation of the condensate*. This is to be expected due to the equally-oriented nature of the lattice. Furthermore, this behaviour was hinted at in the comparison of the offset vortex and offset vortex pair, studied in sections 5.2.2 and 5.2.3. The black lines drawn on the final state plots show how far the, initially horizontal, rows of vortices in the lattices have rotated; the lines are extended to the edge of the graphs (with grid lines) to allow for easy comparison.

6.4.2 Vortex Mean Separation Evolution

The second feature to note, as was noted for all the fcc lattice real-time evolutions, is the evolution of the mean vortex separation. Due to the fcc construction at the beginning, the vortices do not start out in the most energetically favourable configuration; some vortices are closer than others and so the mean separation is not constant. Consequently, during real-time free expansion, the vortex lattice readjusts itself so that all the vortices gradually become equidistant and the lattice tends towards an Abrikosov arrangement. This is particularly clear for systems with high vortex densities, such as in the juxtaposition of figures 6.3e and 6.3f for the 61-lattice case. By comparing the end states of the different vortex density configurations, we can see that *the higher the vortex density, the faster the vortex separations tend to a constant value*. This is also expected, since at higher vortex densities, the vortex interactions are stronger.

⁵This is due to the continual vortex readjustments.

⁶The number of points within concentric rings on a two-dimensional fcc lattice is given by the quadratic sequence: 1, 7, 19, 37, 61, 91, 127, 169, 217, 271.... The second difference of this sequence is 6 and the n^{th} -term is given by $a_n = 3n^2 - 3n + 1$, where $n \in \mathbb{N}$.

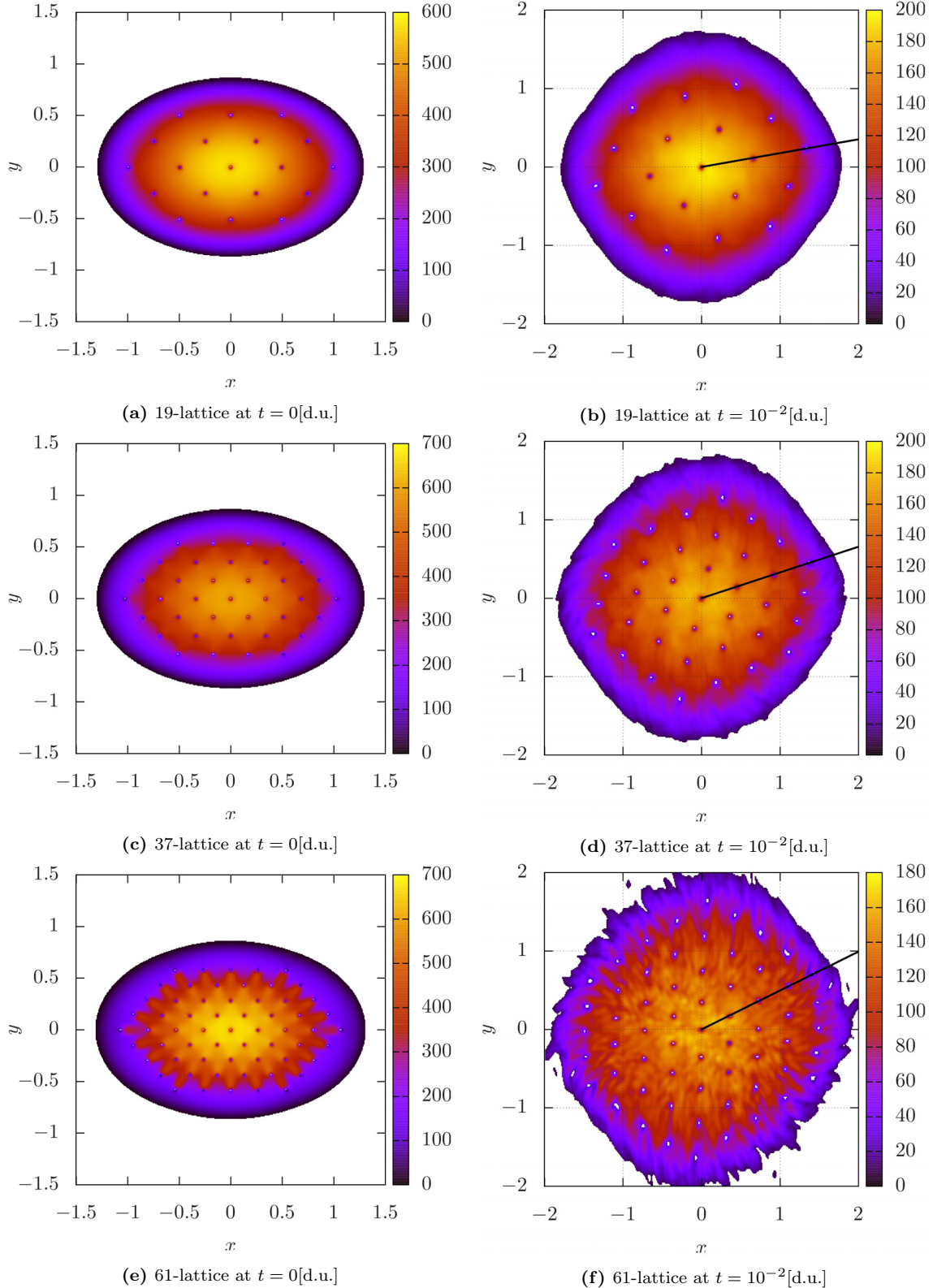


Figure 6.3: Density plots of the vortex lattice rotation of fcc lattices of identical vortices with varying vortex densities in the unnormalised probability density distribution, $|\Psi|^2$, in time intervals of 10^{-2} [d.u.]. The total real-time evolution consisted of 10^3 iterations of a 10^{-5} [d.u.] time-step ((a,b) see figures D.17 and D.18, (c,d) see figures D.19 and D.20, (e,f) see figures D.21 and D.22). Initially, the square lattice had $n^2 = 1000^2$ points and so the axes, which were defined from -4 to 4, are discretised into intervals of $h = 1/125$. $\{|\Psi|^2 > 10\text{[d.u.]}, g = 15\text{[d.u.]}, \omega_x = 100\text{[d.u.]}, \omega_y = 150\text{[d.u.]}, N = 1000\}$

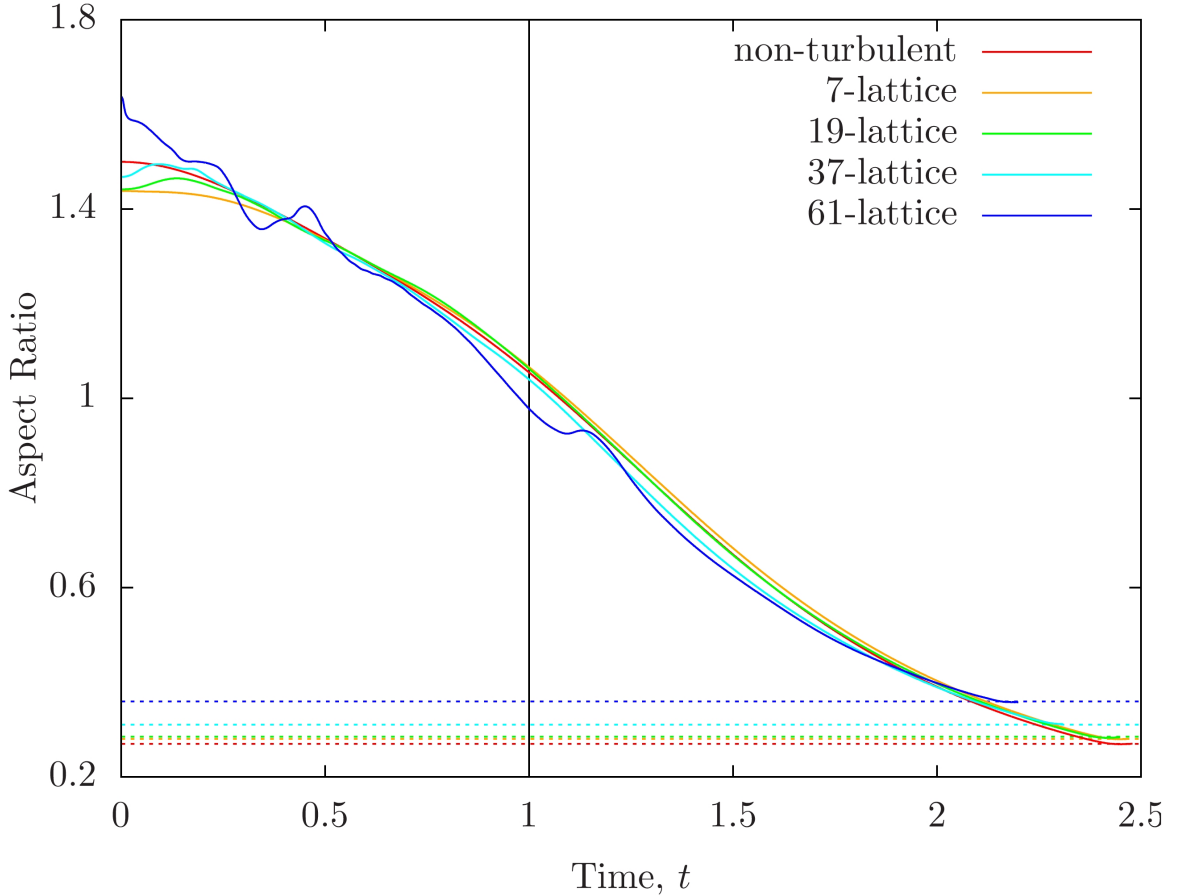


Figure 6.4: The aspect ratio evolution of freely expanding, turbulent anisotropic condensates with varying vortex densities, in temporal units of 10^{-2} [d.u.]. The 19, 37 and 61-lattice graphs correspond to the density plots shown in figure 6.3, and the 7-lattice graph corresponds to the plots shown in appendix D.15. The black line in the figure indicates the point up to which the density plots are shown. The dashed lines indicate the final aspect ratio limits for the corresponding condensates.

6.4.3 Aspect Ratio Evolution

For our final analysis, let us go back to the question posed at the beginning of this thesis. In 2009, *Bagnato et al.* carried out experiments which showed the self-similar expansion of turbulent elliptical condensates. This implies that the aspect ratio was approximately constant under free expansion, which contrasts the normal inversion observed for non-turbulent BECs⁷. In order to reconcile this issue, let us now look in detail at the aspect ratio evolution for the turbulent condensates used in our vortex density trials⁸ (see figure 6.4).

As seen for the non-turbulent case, we observe an aspect ratio inversion when we release our elliptical condensate from the trap, with an initial ratio⁹ of 1.5 and a final ratio of approximately 0.270. However, if we increase the enstrophy of the condensate, then the final aspect ratio limit increases. For the 7, 19, 37 and 61-lattice cases, the final ratios are approximately 0.280, 0.285, 0.310 and 0.359, respectively. Therefore, we can see that the increase in the final limit is non-linear, partly due to the

⁷In fact, aspect ratio inversion is so synonymous with Bose-Einstein condensation, that many experimentalists test for condensates, in trapped anisotropic Bose gases, by observing their free expansion and checking for this ratio inversion [43].

⁸For a numerical discussion of how the aspect ratio was computed, and consequently, an explanation for the fluctuations in the higher vortex density graphs, see appendix B.2.

⁹Note that the initial aspect ratio varies slightly for the different cases, due to the minor influence of the vortex lattice on the initial shape of the condensate.

non-linearity of our vortex density steps. This pattern shows that *as the vortex density increases, the observed free expansion is increasingly self-similar*. Given that in experiments, the number of vortices in a condensate may be very high ($\sim 10^3$) along with the corresponding vortex density [4], the simulations shown here do potentially agree with the experimental results of *Bagnato et al.* [2].

It is now important to assess the validity of this conclusion. In this section, we have carried out trials for five different vortex densities and in all cases, we have found that as we increase the vortex density, the final aspect ratio limit increases. Although there are fluctuations in our aspect ratio graphs, due to the numerical methods (see appendix B.2), the final limits of the graphs are constant and distinct. Naturally, five data points in this region is statistically inadequate to draw extrapolations up to vortex densities an order of magnitude higher. However, the general trend is beginning to emerge. As shown in figure 6.3e, given the healing length used in these trials, there is still the potential to add many more vortices to the system. We would then expect the final ratio limit to gradually increase, until it eventually reaches or exceeds one, and verifies the observed non-inversion.

From a theoretical standpoint, we now need to check these results against the equations derived by *Fetter et al.* (2.51), presented in section 2.5. The solutions to these equations for the given theoretical parameters [4] (plotted in figure 2.2a) show that for turbulent condensates, the final aspect ratio will gradually tend to a value close to one, hence reproducing the non-inversion. The form of this curve is similar to those computed from the simulations. However, in the theoretical model, the curves for the non-turbulent and turbulent cases do not overlap during free expansion. In fact, according to the theory, there is a distinct shift of the curve in relation to the vortex density; whereas in the simulations, the aspect ratio curves only separate out once a final ratio limit has been reached. Since the vortex density steps are comparatively small for the trials in this section, it is possible that this slight shift is present but concealed, due to the inaccuracy of the numerical methods¹⁰. However, currently, even in the stable regions of the data, there is no discernible trend in curve shifts as a function of vortex density.

The data presented in this section is insufficient to definitively confirm or refute the experimental observations of *Bagnato et al.*. However, a distinct trend is observed in the simulations, which agrees with the theory presented by *Fetter et al.*, in that the final aspect ratio limit increases with condensate vortex density. Continuing this trend for the appropriate system parameters may then reproduce the experimental results.

¹⁰Note that all the fluctuations seen in the curves in figure 6.4 are a direct result of the shortcomings of the numerical algorithm.

Conclusion

The main aim of this thesis was to study the experiments of *Bagnato et al.* in order to verify the self-similar expansion of turbulent ellipsoidal condensates; however, many other note-worthy conclusions were drawn along the way. There are numerous factors to consider when simulating the expansion of turbulent Bose-Einstein condensates and naturally, condensate simulations are never perfect, as there will always be inherent theoretical and numerical errors. Building on the work carried out by Pascal Weckesser [1] and Andreas Leonhardt [51], we have chosen to approach this problem by modeling the experimental condensates on two-dimensional elliptical condensates with anisotropic fcc lattices of equally-oriented quantum vortices. This decision was based on numerical considerations, as well as the arguments of *Fetter et al.* presented in section 2.5.

Using this model, we have seen that condensates with equally-oriented vortex lattices rotate during free expansion and that the higher the vortex density within the condensate, the faster the observed rotation. This is a direct consequence of the matching phase addition. Intuitively, if all the vortices are rotating in the same direction, then the rotations will all compliment one another and so, with an increasing number of identical vortices, the angular velocity of the condensate increases.

We have also shown that when starting with an anisotropic vortex lattice, the lattice will tend towards an Abrikosov configuration during free expansion, so that the mean separation of the vortices tends to a constant value. This is a result of the turbulent initial state progression towards a more energetically favourable configuration. Furthermore, the higher the vortex density, the faster the vortex lattice will tend towards this configuration, due to the stronger vortex interactions at smaller separations.

Most importantly, we have shown that for turbulent condensates with small numbers of vortices, there is still an aspect ratio inversion during free expansion; however, the expansion becomes increasingly self-similar, the higher the vortex density, provided that the number of vortices is sufficiently large. Extrapolating this pattern could reproduce the results of *Bagnato et al.*. However, since the exact number of vortices and the vortex density present in the experiments is unknown¹, it is not possible to say for certain whether this simulation completely agrees with the experiment. Nevertheless, it is very probable that the experimental condensates had a far larger number of vortices with a much higher vortex density, which would be in agreement with the simulations.

The crucial next step for this project is to solve the dynamical equations derived by *Fetter et al.* (2.51) for the system parameters used in this thesis. If an agreement between the theory and the computer model is found, then this would further support the validity of the simulations. In addition, the RK4 algorithm could be replaced by a semi-implicit scheme and the finite differences by a Fourier-based algorithm, to improve stability and speed up the computation [50] [52]. Finally, with a reliable theoretical model and an improved simulation, it would then be possible to quickly find the parameters under which the experimental results are reproduced, and confidently verify the observed phenomenon.

¹Future work on this project could include calculating theoretical estimates for these quantities.

A

Derivations and Additional Working

Contents

A.1	Derivation of the Velocity-Phase Relation	65
A.2	Evaluation of a Generalised 1D Infinite Gaussian Integral	66
A.3	Proof that a Gaussian Wavepacket is a Minimum Uncertainty State . .	67
A.4	Solving the TDSE using Plancherel's Theorem	68
A.5	Derivation of the RK4 Algorithm	69
A.6	Derivation of L for the Trapped Central Vortex BEC	70
A.7	Derivation of L for the Trapped Offset Vortex BEC	71
A.8	Proof of Equivalent Norms in Expanding and Stationary Frames . . .	71
A.9	Proof of Conservation of Particle Number in Expanding Coordinates .	72

A.1 Derivation of the Velocity-Phase Relation [1]

This derivation follows directly from the discussion in section 2.3.

Starting from the quantum mechanical probability current density, $\mathbf{j} = \rho\mathbf{v}$, we may isolate the velocity vector, so that

$$\begin{aligned}\rho\mathbf{v} &= -\frac{i\hbar}{2m} (\Psi^*\nabla\Psi - \Psi\nabla\Psi^*) \\ &= \rho\frac{\hbar}{2im} \left(\frac{\Psi^*\nabla\Psi - \Psi\nabla\Psi^*}{|\Psi|^2} \right).\end{aligned}\tag{A.1}$$

Now, we can extract the velocity term and using the functional form of the wavefunction defined in equation (2.22), we may apply the product rule to arrive at the result:

$$\begin{aligned}\mathbf{v} &= \frac{\hbar}{2im} \left[\frac{|\Psi|e^{-i\phi}\nabla|\Psi|e^{i\phi} - |\Psi|e^{i\phi}\nabla|\Psi|e^{-i\phi}}{|\Psi|^2} \right] \\ &= \frac{\hbar}{2im} [e^{-i\phi}(\nabla e^{i\phi} + (i\nabla\phi)e^{i\phi}) - e^{i\phi}(\nabla e^{-i\phi} - (i\nabla\phi)e^{-i\phi})] \\ &= \frac{\hbar}{m}\nabla\phi \blacksquare\end{aligned}\tag{A.2}$$

A.2 Evaluation of a Generalised 1D Infinite Gaussian Integral

Gaussian integrals are very common in Physics and often rearranging a problem into this form is the key to arriving at a solution. Here is a simple evaluation of a generalised one-dimensional infinite Gaussian integral:

$$\begin{aligned}
I &= \int_{-\infty}^{\infty} ae^{-b(x+c)^2} dx \\
I^2 &= a^2 \int_{-\infty}^{\infty} e^{-b(x+c)^2} dx \int_{-\infty}^{\infty} e^{-b(y+c)^2} dy \\
&= a^2 \int_{-\infty}^{\infty} e^{-b\tilde{x}^2} d\tilde{x} \int_{-\infty}^{\infty} e^{-b\tilde{y}^2} d\tilde{y} \\
&= a^2 \int_{-\infty}^{\infty} \int_{-\infty}^{\infty} e^{-b(\tilde{x}^2 + \tilde{y}^2)} d\tilde{x} d\tilde{y} \\
&= a^2 \int_0^{2\pi} \int_0^{\infty} e^{-br^2} r dr d\theta \\
&= 2\pi a^2 \int_0^{\infty} r e^{-br^2} dr \\
&= 2\pi a^2 \left(-\frac{1}{2b} \int_0^{-\infty} e^u du \right) \\
&= \frac{\pi a^2}{b} \int_{-\infty}^0 e^u du \\
&= \frac{\pi a^2}{b} [e^0 - e^{-\infty}] \\
&= \frac{\pi a^2}{b} \\
\Rightarrow I &= a \sqrt{\frac{\pi}{b}} \blacksquare
\end{aligned} \tag{A.3}$$

where a , b and c are constants. Note that in the third line, we used the substitutions $\tilde{x} \equiv x + c$ and $\tilde{y} \equiv y + c$. Subsequently, in the seventh line, we substituted $u \equiv -br^2$.

For a rigorous proof, one would have to use general limits of integration and then take the limit as they go to infinity, whilst making sure that the integrand is absolutely convergent [53].

A.3 Proof that a Gaussian Wavepacket is a Minimum Uncertainty State

Let us start with a simple normalised Gaussian wavefunction given by¹

$$\psi(x) = \left(\frac{2}{\pi}\right)^{\frac{1}{4}} e^{-x^2}. \quad (\text{A.4})$$

The mean-squared uncertainty in position is given by

$$\begin{aligned} (\Delta x)^2 &= \langle x^2 \rangle - \langle x \rangle^2 \\ &= \int_{-\infty}^{\infty} \psi \hat{x}^2 \psi^* dx - \left(\int_{-\infty}^{\infty} \psi \hat{x} \psi^* dx \right)^2 \\ &= \sqrt{\frac{2}{\pi}} \int_{-\infty}^{\infty} x^2 e^{-2x^2} dx - \left(\sqrt{\frac{2}{\pi}} \underbrace{\int_{-\infty}^{\infty} x e^{-2x^2} dx}_{=0} \right)^2 \\ &= \sqrt{\frac{2}{\pi}} \underbrace{\left[-\frac{x}{4} e^{-2x^2} \right]_{-\infty}^{\infty}}_{=0} + \sqrt{\frac{2}{\pi}} \int_{-\infty}^{\infty} \frac{e^{-2x^2}}{4} dx \\ &= \frac{1}{4}, \end{aligned} \quad (\text{A.5})$$

and the mean-squared uncertainty in momentum is

$$\begin{aligned} (\Delta p)^2 &= \langle p^2 \rangle - \langle p \rangle^2 \\ &= \int_{-\infty}^{\infty} \psi \hat{p}^2 \psi^* dx - \left(\int_{-\infty}^{\infty} \psi \hat{p} \psi^* dx \right)^2 \\ &= -\hbar^2 \sqrt{\frac{2}{\pi}} \int_{-\infty}^{\infty} e^{-x^2} \frac{\partial^2}{\partial x^2} e^{-x^2} dx - \left(i\hbar \sqrt{\frac{2}{\pi}} \int_{-\infty}^{\infty} e^{-x^2} \frac{\partial}{\partial x} e^{-x^2} dx \right)^2 \\ &= 2\hbar^2 \sqrt{\frac{2}{\pi}} \int_{-\infty}^{\infty} e^{-2x^2} dx - 4\hbar^2 \sqrt{\frac{2}{\pi}} \int_{-\infty}^{\infty} x^2 e^{-2x^2} dx - \left(-2i\hbar \sqrt{\frac{2}{\pi}} \underbrace{\int_{-\infty}^{\infty} x e^{-2x^2} dx}_{=0} \right)^2 \\ &= 2\hbar^2 - \hbar^2 \\ &= \hbar^2. \end{aligned} \quad (\text{A.6})$$

Hence,

$$\Delta x \Delta p = \frac{\hbar}{2} \blacksquare \quad (\text{A.7})$$

¹Note that this derivation would equally apply to any normalised Gaussian wavefunction [42].

A.4 Solving the TDSE using Plancherel's Theorem [39]

This derivation follows directly from the discussion in section 3.1.5.

Since we know the initial wavefunction, we can find $\hat{\psi}(k)$ via Plancherel's theorem:

$$\begin{aligned}
 \hat{\psi}(k) &= \frac{1}{\sqrt{2\pi}} \int_{-\infty}^{\infty} \psi(x, 0) e^{-ikx} dx \\
 &= \frac{1}{\sqrt{2\pi}} \left(\frac{2}{\pi} \right)^{\frac{1}{4}} \int_{-\infty}^{\infty} e^{-(x^2 + ikx)} dx \\
 &= \frac{1}{\sqrt{2\pi}} \left(\frac{2}{\pi} \right)^{\frac{1}{4}} \int_{-\infty}^{\infty} e^{-[(x + \frac{ik}{2})^2 + \frac{k^2}{4}]} dx \\
 &= \frac{e^{-\frac{k^2}{4}}}{\sqrt{2\pi}} \left(\frac{2}{\pi} \right)^{\frac{1}{4}} \int_{-\infty}^{\infty} e^{-(x + \frac{ik}{2})^2} dx \\
 &= \left(\frac{1}{2\pi} \right)^{\frac{1}{4}} e^{-\frac{k^2}{4}}.
 \end{aligned} \tag{A.8}$$

Now, if we substitute this result back into equation (3.25) then we obtain

$$\begin{aligned}
 \psi(x, t) &= \frac{1}{\sqrt{2\pi}} \left(\frac{2}{\pi} \right)^{\frac{1}{4}} \int_{-\infty}^{\infty} e^{-\frac{k^2}{4}} e^{-\frac{i\hbar k^2 t}{2m}} e^{ikx} dk \\
 &\propto \int_{-\infty}^{\infty} \exp \left\{ - \left[\left(\frac{1}{4} + \frac{i\hbar t}{2m} \right) k^2 - ixk \right] \right\} dk \\
 &\propto \int_{-\infty}^{\infty} \exp \left\{ - \left(\frac{1}{4} + \frac{i\hbar t}{2m} \right) \left[k^2 - \frac{ix}{\frac{1}{4} + \frac{i\hbar t}{2m}} k \right] \right\} dk \\
 &\propto \exp \left(\frac{1}{4} + \frac{i\hbar t}{2m} \right) \int_{-\infty}^{\infty} \exp \left\{ - \left[k - \frac{ix}{2(\frac{1}{4} + \frac{i\hbar t}{2m})} \right]^2 - \left(\frac{x}{2(\frac{1}{4} + \frac{i\hbar t}{2m})} \right)^2 \right\} dk \\
 &\propto \exp \left\{ \left(\frac{1}{4} + \frac{i\hbar t}{2m} \right) - \left(\frac{x}{2(\frac{1}{4} + \frac{i\hbar t}{2m})} \right)^2 \right\} \int_{-\infty}^{\infty} \exp \left\{ - \left[k - \frac{ix}{2(\frac{1}{4} + \frac{i\hbar t}{2m})} \right]^2 \right\} dk \\
 &= \left(\frac{2}{\pi} \right)^{\frac{1}{4}} \frac{e^{-x^2/(1+2i\hbar t/m)}}{\sqrt{1+2i\hbar t/m}},
 \end{aligned} \tag{A.9}$$

where we have used the fact that the energy of a wave expressed as a function of its wavenumber is $E = \hbar^2 k^2 / 2m$. Using this result, we can finally calculate the probability density function:

$$\begin{aligned}
 |\psi(x, t)|^2 &= \sqrt{\frac{2}{\pi}} \frac{e^{-2x^2/[1+(2\hbar t/m)^2]}}{\sqrt{1+(2\hbar t/m)^2}} \\
 &= \sqrt{\frac{2}{\pi}} \omega e^{-2\omega^2 x^2}
 \end{aligned} \tag{A.10}$$

where

$$\omega \equiv \frac{1}{\sqrt{1+(2\hbar t/m)^2}} \blacksquare$$

A.5 Derivation of the RK4 Algorithm [54]

Generalising the problem outlined in section 3.1.4, we know that the effective ODE that needs to be solved has the form:

$$\dot{\psi}(t) = f[\psi(t)]. \quad (\text{A.11})$$

If we now Taylor expand the wavefunction for a later time, $t + \delta t$, then we obtain:

$$\psi_{n+1} = \psi_n + \delta t f(\psi_n) + \frac{\delta t^2}{2!} \frac{df(\psi_n)}{dt} + \frac{\delta t^3}{3!} \frac{d^2 f(\psi_n)}{dt^2} + \frac{\delta t^4}{4!} \frac{d^3 f(\psi_n)}{dt^3} + O(\delta t^5), \quad n \in \mathbb{N}. \quad (\text{A.12})$$

Since we are looking for a fourth-order Runge-Kutta approximation for ψ_{n+1} , then we are already expecting a function of the form²

$$\psi_{n+1} = \psi_n + \delta t \left[af(\psi_n) + bf\left(\psi_{n+\frac{1}{2}}^*\right) + cf\left(\psi_{n+\frac{1}{2}}^{**}\right) + df\left(\psi_{n+1}^{***}\right) \right] + O(\delta t^5), \quad (\text{A.13})$$

where

$$\begin{aligned} \psi_{n+\frac{1}{2}}^* &= \psi_n + \frac{\delta t}{2} f(\psi_n), \\ \psi_{n+\frac{1}{2}}^{**} &= \psi_n + \frac{\delta t}{2} f\left(\psi_{n+\frac{1}{2}}^*\right), \\ \psi_{n+1}^{***} &= \psi_n + \delta t f\left(\psi_{n+\frac{1}{2}}^{**}\right) \end{aligned} \quad (\text{A.14})$$

and a, b, c and d are constants to be determined³. Since we know that

$$\begin{aligned} f\left(\psi_{n+\frac{1}{2}}^*\right) &= f\left(\psi_n + \frac{\delta t}{2} f(\psi_n)\right) \\ &= f(\psi_n) + \frac{\delta t}{2} \frac{df(\psi_n)}{dt}, \\ f\left(\psi_{n+\frac{1}{2}}^{**}\right) &= f\left(\psi_n + \frac{\delta t}{2} f\left(\psi_{n+\frac{1}{2}}^*\right)\right) \\ &= f(\psi_n) + \frac{\delta t}{2} \frac{d}{dt} \left[f(\psi_n) + \frac{\delta t}{2} \frac{df(\psi_n)}{dt} \right], \\ f\left(\psi_{n+1}^{***}\right) &= f\left(\psi_n + \delta t f\left(\psi_n + \frac{\delta t}{2} f\left(\psi_{n+\frac{1}{2}}^*\right)\right)\right) \\ &= f(\psi_n) + \delta t \frac{d}{dt} \left\{ f(\psi_n) + \frac{\delta t}{2} \frac{d}{dt} \left[f(\psi_n) + \frac{\delta t}{2} \frac{df(\psi_n)}{dt} \right] \right\}, \end{aligned} \quad (\text{A.15})$$

we can substitute this into our original Runge-Kutta form (A.13) to obtain:

$$\begin{aligned} \psi_{n+1} &= \psi_n + \delta t [af(\psi_n) \\ &\quad + b\left(f(\psi_n) + \frac{\delta t}{2} \frac{df(\psi_n)}{dt}\right) \\ &\quad + c\left(f(\psi_n) + \frac{\delta t}{2} \frac{d}{dt} \left[f(\psi_n) + \frac{\delta t}{2} \frac{df(\psi_n)}{dt} \right]\right) \\ &\quad + d\left(f(\psi_n) + \delta t \frac{d}{dt} \left\{ f(\psi_n) + \frac{\delta t}{2} \frac{d}{dt} \left[f(\psi_n) + \frac{\delta t}{2} \frac{df(\psi_n)}{dt} \right] \right\}\right)] + O(\delta t^5). \end{aligned} \quad (\text{A.16})$$

²In a rigorous derivation one would not assume this. To carry out the full derivation, one would need to label all prefactors as undetermined coefficients and consequently, end up with 12 simultaneous equations in 12 unknowns, instead of the 4 derived here [37]. For this step, we are using our knowledge of the symmetry of Runge-Kutta algorithms to deduce the inner functions.

³In this context, the * symbol does not denote the complex conjugate. Here, it is simply a way of distinguishing between the different wavefunctions.

If we now compare this equation to our Taylor expansion (A.12), then we obtain the following four simultaneous equations for the undetermined constants:

$$\left\{ \begin{array}{l} \frac{d}{2^2} = \frac{1}{4!} \\ \frac{c}{2^2} + \frac{d}{2} = \frac{1}{3!} \\ \frac{b}{2} + \frac{c}{2} + d = \frac{1}{2!} \\ a + b + c + d = 1. \end{array} \right. \quad (\text{A.17})$$

Solving these equations, we can deduce that $a = d = 1/6$ and $b = c = 1/3$. Therefore, we now arrive at the final iterative formula for the RK4 algorithm:

$$\psi_{n+1} = \psi_n + \frac{\delta t}{6} \left[\underbrace{f(\psi_n)}_{K_1} + 2 \underbrace{f\left(\psi_{n+\frac{1}{2}}^*\right)}_{K_2} + 2 \underbrace{f\left(\psi_{n+\frac{1}{2}}^{**}\right)}_{K_3} + \underbrace{f\left(\psi_{n+1}^{***}\right)}_{K_4} \right] + O(\delta t^5) \blacksquare \quad (\text{A.18})$$

A.6 Derivation of L for the Trapped Central Vortex BEC [1]

This derivation follows directly from the discussion in section 5.2.1.

From the BEC circulation equation (2.28) discussed in section 2.3, we know that

$$\Gamma = \oint \mathbf{v} \cdot d\mathbf{l} = \int_0^{2\pi} vr d\phi = \frac{h}{m} l. \quad (\text{A.19})$$

Following on the general ellipsoidal-condensate orbital angular momentum integral (5.4) and using the Thomas-Fermi density form (5.5), we find that

$$\begin{aligned} \mathbf{L} &= abc \iiint m\rho_0 \left(1 - \frac{x^2}{a^2} - \frac{y^2}{b^2} - \frac{z^2}{c^2}\right) vr \cdot r^2 |\sin \theta| dr d\theta d\phi \hat{\mathbf{e}}_z \\ &= abcm\rho_0 \iiint (1 - r^2) vr^3 |\sin \theta| dr d\theta d\phi \hat{\mathbf{e}}_z \\ &= abcm\rho_0 \int_0^1 r^2 (1 - r^2) dr \int_0^\pi |\sin \theta| d\theta \int_0^{2\pi} vr d\phi \hat{\mathbf{e}}_z \\ &= \frac{8\pi}{15} \rho_0 abc \hbar l \hat{\mathbf{e}}_z \\ &= N\hbar l \hat{\mathbf{e}}_z \blacksquare \end{aligned} \quad (\text{A.20})$$

From the penultimate to the final line, we have applied the Thomas-Fermi particle number relation (5.6).

A.7 Derivation of \mathbf{L} for the Trapped Offset Vortex BEC [1]

This derivation follows directly from the discussion in section 5.2.2.

Since we know that the inner ellipse is irrotational, we may write the circulation for the BEC as

$$\Gamma = \oint \mathbf{v} \cdot d\mathbf{l} = \int_0^{2\pi} vr d\phi = \frac{\hbar}{m} l \Theta(r - d), \quad (\text{A.21})$$

where Θ denotes the Heaviside step function. Following on the general ellipsoidal-condensate orbital angular momentum integral (5.4) and using the same Thomas-Fermi density form (5.5) together with the Thomas-Fermi particle number relation (5.6), we find that

$$\begin{aligned} \mathbf{L} &= abc \iiint m\rho_0 \left(1 - \frac{x^2}{a^2} - \frac{y^2}{b^2} - \frac{z^2}{c^2}\right) vr \cdot r^2 |\sin \theta| dr d\theta d\phi \hat{\mathbf{e}}_z \\ &= abcm\rho_0 \iiint (1 - r^2) vr^3 |\sin \theta| dr d\theta d\phi \hat{\mathbf{e}}_z \\ &= abcm\rho_0 \int_0^1 r^2 (1 - r^2) dr \int_0^\pi |\sin \theta| d\theta \int_0^{2\pi} vr d\phi \hat{\mathbf{e}}_z \\ &= 2abchl\rho_0 \int_d^1 r^2 (1 - r^2) dr \hat{\mathbf{e}}_z \\ &= 4\pi abchl\rho_0 \left[\frac{2}{15} - \frac{d^3}{3} - \frac{d^5}{5}\right] \hat{\mathbf{e}}_z \\ &= \frac{8\pi}{15} \rho_0 abc \hbar l \left(1 - \frac{5}{2}d^3 - \frac{3}{2}d^5\right) \hat{\mathbf{e}}_z \\ &= N\hbar l \left(1 - \frac{5}{2}d^3 - \frac{3}{2}d^5\right) \hat{\mathbf{e}}_z \blacksquare \end{aligned} \quad (\text{A.22})$$

A.8 Proof of Equivalent Norms in Expanding and Stationary Frames [51]

This derivation follows directly from the discussion in section 6.1.

Let us consider the norm in one particular direction, for instance, the x -direction, to make the working clearer.

$$\begin{aligned} \langle \Psi(x, t) | \Psi(x, t) \rangle &= \int \Psi^*(x, t) \Psi(x, t) dx \\ &= \frac{1}{\lambda_x} \int \Psi^*(x'/\lambda_x, t) \Psi(x'/\lambda_x, t) dx' \\ &= \int \Psi'^*(x', t) \Psi'(x', t) dx' \\ \Rightarrow \langle \Psi(x, t) | \Psi(x, t) \rangle &\equiv \langle \Psi'(x', t) | \Psi'(x', t) \rangle \blacksquare \end{aligned} \quad (\text{A.23})$$

Note that this relation equally applies in any direction, as well as over the whole space, due to the orthogonality of the unit vectors.

A.9 Proof of Conservation of Particle Number in Expanding Coordinates [51]

This derivation follows directly from the discussion in section 6.1.

For our fixed coordinate system, we know that our total particle number, N , is given by $N = \langle \Psi | \Psi \rangle$. We also know that the total particle number is conserved, such that $\partial_t \langle \Psi | \Psi \rangle = 0$. We now need to ensure that this is also true in the expanding coordinate system. As before, let us consider the argument in the x -direction, to simplify the algebra. The one-dimensional time-dependent GPE in an expanding frame may, therefore, be written as

$$\begin{aligned} i\hbar \partial_t \Psi &= \left[\underbrace{-\frac{\hbar^2}{2m} \frac{\nabla^2}{\lambda_x} + V + g|\Psi|^2}_{\hat{H}_0} + i\hbar \frac{\dot{\lambda}_x}{\lambda_x} x \nabla \right] \Psi \\ \Rightarrow \partial_t \Psi &= \left[-\frac{i\hat{H}_0}{\hbar} + \frac{\dot{\lambda}_x}{\lambda_x} x \nabla \right] \Psi, \end{aligned} \quad (\text{A.24})$$

where \hat{H}_0 now denotes the expanding frame GPE Hamiltonian without the expansion term. Taking the temporal derivative of the particle number in this frame yields

$$\begin{aligned} \partial_t \langle \Psi' | \Psi' \rangle &= \partial_t \left(\lambda_x^{-1} \int \Psi^* \Psi \, dx' \right) \\ &= -\lambda_x^{-2} \dot{\lambda}_x \int |\Psi|^2 \, dx' + \lambda_x^{-1} \int (\Psi \partial_t \Psi^* + \Psi^* \partial_t \Psi) \, dx' \\ &= -\frac{\dot{\lambda}_x}{\lambda_x} N + \lambda_x^{-1} \int \left(\Psi \left[\frac{i\hat{H}_0}{\hbar} + \frac{\dot{\lambda}_x}{\lambda_x} x \nabla \right] \Psi^* + \Psi^* \left[-\frac{i\hat{H}_0}{\hbar} + \frac{\dot{\lambda}_x}{\lambda_x} x \nabla \right] \Psi \right) \, dx' \\ &= -\frac{\dot{\lambda}_x}{\lambda_x} N + \lambda_x^{-1} \int \frac{i\hbar}{2m} (\Psi^* \nabla^2 \Psi - \Psi \nabla^2 \Psi^*) \, dx' \\ &\quad + \lambda_x^{-1} \int \frac{\dot{\lambda}_x}{\lambda_x} x (\Psi \nabla \Psi^* + \Psi^* \nabla \Psi) \, dx' \\ &= -\frac{\dot{\lambda}_x}{\lambda_x} N + \lambda_x^{-1} \int \underbrace{\nabla \left(-\frac{\hbar}{m} |\Psi|^2 \nabla \phi \right)}_{=0} \, dx' + \lambda_x^{-1} \int \underbrace{\frac{\dot{\lambda}_x}{\lambda_x} (\nabla x)}_{=1} |\Psi|^2 \, dx' \\ &= -\cancel{\frac{\dot{\lambda}_x}{\lambda_x} N} + \cancel{\frac{\dot{\lambda}_x}{\lambda_x} N} \\ &= 0 \blacksquare \end{aligned} \quad (\text{A.25})$$

Here, we have used the product rule again to expand the derivative. The results for the wavefunction transforms were then substituted in and we used the results from appendix A.1 to express one of the integrals in terms of the phase gradient, $\nabla \phi$. Finally, we used the norm condition for the expanding frame to obtain the total particle number, N , and subsequently arrive at the result.

B

Numerical Methods

B.1 The Vortex Tracking Algorithm

The vortex tracking algorithm used in this thesis is somewhat rudimentary, in that it is solely based on probability density. As mentioned before, the unique definition of a vortex core is the origin of the vortex phase rotation. These phase rotations then only manifest themselves as density dips over time. Consequently, any density-based algorithm used to track vortices is crude and unsatisfactory in the long-term. However, for the purposes of tracking vortices in simple systems, such as the cases demonstrated in section 5.2, a purely density-based algorithm works reasonably well. [55]

The algorithm used in this report is designed to track fully-developed, distinct vortices. It works by finding density minima and then checking if these density minima are isolated. Finding the vortices using density alone is problematic in inhomogeneous systems, since most of the region outside of the bulk condensate will have a density lower than or equal to the density of the vortex core. These sorts of problems are then exacerbated by the fact that the density profile is limited to the resolution of the grid. The first step, therefore, in this process, is to conditionally filter the density. We need to select the low-density points, such that the vortex is represented by a single pixel. Naturally, this algorithm only works if the initial position of all the vortices is known. Plotting all the points below this density value will then give the quantum vortex as a single point, along with the whole region outside of the bulk condensate. It is this region that we now need to eliminate. In addition to this low-density criterion, we will consequently check all neighbouring pixels to see if their densities are higher or lower than the central one. If all the neighbouring pixels have a higher density than the central pixel *after the initial density filter has been passed*, then we know that this point is a vortex core. However, this criterion is actually too stringent for the simulations carried out in section 5.2. This is partly due to the fact that the vortex may deform slightly as it moves along, and partly due to the resolution of the grid. Regardless, the vortex that initially occupies one pixel may fluctuate between a one pixel and two pixel state as it progresses. To accommodate for this fluctuation, we can modify our second criterion to checking if all the neighbouring pixels *or all but one* of the neighbouring pixels have higher density values than the central pixel. These two criteria alone work quite well for simple systems, where the vortices are not drastically deformed.

In order to track vortices in more complex systems, such as those in figure 6.3, a more reliable algorithm is needed. As stated before, phase-based/hybrid algorithms, are far superior to purely density-based methods because they can easily be scaled to more complex systems. For example, for each pixel from a density-based preselection, one could look at all the neighbouring pixels and check if the sum of the phase changes around the ring is equal to 2π . If this is fulfilled, then the central pixel would indicate the position of a vortex core. Unfortunately, due to the numerics, this process is not as robust as it sounds and this sum is not always equal to 2π , or a comparable value. In order to address this issue, alternative approaches need to be considered, such as summing the phase jumps around outer rings of pixels or taking the average value of several rings.

B.2 The Aspect Ratio Algorithm

Determining the aspect ratio of an elliptical condensate is, in theory, a simple task. All that needs to be done is a division of the length of the major axis by the length of the minor axis. However, for the turbulent condensates considered in this thesis, there are many numerical issues that need to be taken into account, in order to obtain consistent and reliable results.

The concept behind the algorithm employed in this report is based on numerical integration and nested intervals. From the standard initial conditions used, we know that the major axis lies along the x -axis, whereas the minor axis lies along the y -axis. We start, therefore, at the origin and then numerically integrate the density up to the edge of the computational grid. Then, we use the nested intervals method from the origin out to an increasing value, until we find a value at which this interval contains 90% of the density integrated along that line. The length of this interval effectively gives the length of the principle axis under consideration. It is important to use numerical integration, rather than just a simple density cut-off, so that the aspect ratio value is not limited by the resolution of the density grid. For instance, if the aspect ratios in figure 6.4 were calculated by simply measuring how long the nested interval was before the density dropped below a certain value, then the curves would be jagged and discretised to the resolution of the grid. Integration methods are also superior to straight cut-off methods when dealing with topological defects.

This aspect ratio algorithm works well for condensates with no vortices, as shown by the ‘non-turbulent’ graph in figure 6.4. However, once we have density dips within the bulk condensate, care needs to be taken when interpreting the aspect ratio values. Naturally, with a straight cut-off method, when a quantum vortex passes through one of the principle axes, the algorithm will see this density drop and assume that this is the edge of the bulk condensate. This is clearly an unsatisfactory method when dealing with the aspect ratio evolution of turbulent condensates. The integral method is an improvement on this, in that it does not immediately stop when it encounters a vortex; however, it is still affected. When a vortex passes through one of the principle axes, on this occasion, the value of the density integral will drop undesirably. This will result in ‘90% of the density integral’ yielding a lower value than intended. Therefore, during free expansion, the plot of the aspect ratio evolution for turbulent condensates, using this algorithm, may have slight fluctuations from the true evolution due to these density defects (as seen in figure 6.4). Consequently, the aspect ratio graphs in the figure are more unstable, the higher the number of vortices.

There are many possible ways to combat this problem and in the most part, they hinge on a reliable vortex detection scheme. Once the program can accurately and consistently detect the vortices in the bulk condensate, then the vortex detection algorithm can be coupled with the aspect ratio algorithm to overcome this issue. In this case, the algorithm would be able to identify when a vortex, or multiple vortices, are passing through the principle axes of the ellipse and then, for example, adaptively offset the density integral. This would compensate for the density dips in the integrals and consequently, give more realistic evolution plots.

C

D-Dimensional Bose-Einstein Condensation

The aim of this appendix is to briefly look at the physics of BECs in an arbitrary number of dimensions, $D \in \mathbb{N}$. In this thesis, simulations were discussed in one, two and three dimensions. However, the physics of a condensate differs greatly between these spaces.

C.1 The D -Dimensional Density of States

C.1.1 Massive Particles

For this derivation, let us consider a massive particle confined in a D -dimensional hypercube of length L . From elementary quantum mechanics, we know that the standing wave condition for the n^{th} -mode of a particle in the i -direction is given by $L = n_i \lambda_i / 2$. From the de Broglie relation, we also know that the momentum of the particle is given by $p_i = h/\lambda_i = n_i h / 2L$. Consequently, we can derive the energy of a non-relativistic particle:

$$\begin{aligned} E &= \frac{|\mathbf{p}|^2}{2m} \\ &= \frac{h^2}{8mL^2} \underbrace{\sum_{i=1}^D n_i^2}_{\equiv n^2}. \end{aligned} \tag{C.1}$$

Let us now consider the set of N modes which have an energy less than or equal to the energy of mode n . This corresponds to the positive content of a hypersphere of radius n . Given that the volume of this D -dimensional hypersphere has the form $v_D n^D$, where $v_D = \pi^{D/2} / \Gamma(D/2 + 1)$ is some geometrical constant¹, we can calculate the positive content by dividing this by 2^D . This leads to

$$N = v_D \left(\frac{n}{2}\right)^D \Rightarrow dN = \frac{D}{2^D} v_D n^{D-2} n dn, \tag{C.2}$$

where dN is the number of modes with an energy between E and $E + dE$. Differentiating the equation for E (C.1) leads to

$$dE = \frac{h^2}{4mL^2} n dn \tag{C.3}$$

¹Here, Γ denotes the gamma function and is defined as $\Gamma(z) \equiv \int_0^\infty t^{z-1} e^{-t} dt \quad \forall z \in \mathbb{C}$.

and so combining equations (C.1), (C.2) and (C.3) gives our final expression for the D -dimensional density of states:

$$\begin{aligned} g(E) &\equiv \frac{dN}{dE} \\ &= \frac{4mL^2}{h^2} \frac{D}{2^D} v_D n^{D-2} \\ &= \frac{4mL^2}{h^2} \frac{D}{2^D} v_D \left(\frac{8mL^2 E}{h^2} \right)^{(D-2)/2} \\ &= \frac{Dv_D}{2} (2m)^{D/2} \frac{V_D}{h^D} E^{(D-2)/2}. \end{aligned} \quad (\text{C.4})$$

Here, $V_D = L^D$ is the volume of the D -dimensional hypercube. This expression for $g(E)$ will come in useful when assessing the validity of BECs in D dimensions. [56]

C.1.2 Massless Particles

In the case of massless particles, we have to express their energy relativistically. Therefore, we can deduce that:

$$\begin{aligned} E &= c|\mathbf{p}| \\ &= \frac{ch}{2L} \sum_{i=1}^D n_i. \end{aligned} \quad (\text{C.5})$$

$\underbrace{}_{\equiv n}$

Differentiating this equation yields

$$dE = \frac{ch}{2L} dn \quad (\text{C.6})$$

and combining this with equation (C.2) leads to our final formula for the D -dimensional density of states:

$$\begin{aligned} g(E) &\equiv \frac{dN}{dE} \\ &= \frac{2L}{ch} \frac{D}{2^D} v_D n^{D-1} \\ &= \frac{2L}{ch} \frac{D}{2^D} v_D \left(\frac{2LE}{ch} \right)^{D-1} \\ &= \frac{Dv_D}{c^D} \frac{V_D}{h^D} E^{D-1}. \end{aligned} \quad (\text{C.7})$$

C.2 Massive Boson Condensates

Let us now consider a fluid of massive, non-interacting, identical, spin-0 Bosons. The total number of Bosons in a given state with energy E is given by

$$N = \int_0^\infty \bar{n}(E) dN, \quad (\text{C.8})$$

where the mean occupation number, \bar{n} , follows the Bose-Einstein distribution:

$$\bar{n}(E) = \frac{1}{e^{\beta(E-\mu)} - 1}. \quad (\text{C.9})$$

Here, $\beta \equiv 1/k_B T$ denotes inverse temperature and μ is the chemical potential. If we now convert equation (C.8) into an energy integral and use our expression for the D -dimensional density of states

(C.4), then we can deduce that

$$\begin{aligned}
N &= \int_0^\infty \bar{n}(E)g(E) \, dE \\
&= \frac{Dv_D}{2} (2m)^{D/2} \frac{V_D}{h^D} \int_0^\infty \frac{E^{(D-2)/2}}{e^{\beta(E-\mu)} - 1} \, dE \\
&\propto \int_0^\infty \frac{E^{(D-2)/2}}{e^{\beta(E-\mu)}} \frac{1}{1 - e^{-\beta(E-\mu)}} \, dE \\
&\propto \int_0^\infty \frac{E^{(D-2)/2}}{e^{\beta(E-\mu)}} \sum_{l=0}^\infty e^{-\beta l(E-\mu)} \, dE \\
&\propto \int_0^\infty E^{(D-2)/2} \sum_{l=1}^\infty e^{-\beta l(E-\mu)} \, dE \\
&\propto \int_0^\infty E^{(D-2)/2} \sum_{l=1}^\infty e^{-\beta lE} e^{\beta l\mu} \, dE \\
&\Rightarrow N|_T \propto \sum_{l=1}^\infty \frac{e^{\beta\mu l}}{l^{D/2}}.
\end{aligned} \tag{C.10}$$

For this calculation, we have assumed that $e^{-\beta(E-\mu)} < 1$, which is a valid assumption since the mean occupation number, $\bar{n}(E)$, cannot be negative due to its physical interpretation. Also, notice that the last summation may be written as a generalised Riemann zeta function of the form:

$$g_\nu(z) \equiv \sum_{l=1}^\infty \frac{z^l}{l^\nu} \quad \forall z, \nu \in \mathbb{C} : \Re\{\nu\} > 1. \tag{C.11}$$

If we now look for the condensed state, we know that we obtain a BEC when the number of particles in the ground state is at a maximum. By inspection, we can see that N is maximised when $\mu = 0$. In this case, our generalised Riemann zeta function becomes a regular Riemann zeta function of the form:

$$\zeta(\nu) \equiv \sum_{l=1}^\infty \frac{1}{l^\nu} \quad \forall \nu \in \mathbb{C} : \Re\{\nu\} > 1. \tag{C.12}$$

Consequently, our previous result for the number of particles in the ground state may be used to arrive at the Bose condensate relation,

$$\lim_{\mu \rightarrow 0} \{N|_{T_C}\} \propto \zeta\left(\frac{D}{2}\right)$$

(C.13)

where T_C is the critical temperature. From this, we can see that for $D = 1$, the argument of the Riemann zeta function does not fulfill the condition demanded in (C.12). The zeta function does happen to converge for an argument of $1/2$, however the value is negative and so the solution is not physical. This shows that *one-dimensional BECs do not exist for massive bosons*.

Let us now look at the case for $D = 2$. In this situation, the argument of the zeta function is one, which also does not fulfill the condition demanded in (C.12). In fact, in this case the zeta function is divergent, in that $\zeta(1) \rightarrow \infty$. This solution is also not physical and so we can conclude that *two-dimensional BECs do not exist for massive bosons*².

If we look at $D \geq 3$, however, we can see that the argument of the zeta function will satisfy the condition required. Therefore, we know that N will converge to a positive number and so *massive boson BECs are only possible in three or more spatial dimensions*.

²As mentioned in section 2.2.1, the GPE is a *zero-temperature* model and so it is possible to model massive-particle, two-dimensional BECs, under certain conditions [17]. This does not hold at finite temperatures.

C.3 Massless Boson Condensates

Let us now carry out the same procedure for a condensate made up of massless bosons (e.g. photons). We start, as before, by converting (C.8) into an energy integral:

$$\begin{aligned}
N &= \int_0^\infty \bar{n}(E)g(E) \, dE \\
&= \frac{Dv_D}{c^D} \frac{V_D}{h^D} \int_0^\infty \frac{E^{D-1}}{e^{\beta(E-\mu)} - 1} \, dE \\
&\propto \int_0^\infty \frac{E^{D-1}}{e^{\beta(E-\mu)}} \frac{1}{1 - e^{-\beta(E-\mu)}} \, dE \\
&\propto \int_0^\infty \frac{E^{D-1}}{e^{\beta(E-\mu)}} \sum_{l=0}^\infty e^{-\beta l(E-\mu)} \, dE \\
&\propto \int_0^\infty E^{D-1} \sum_{l=1}^\infty e^{-\beta l(E-\mu)} \, dE \\
&\propto \int_0^\infty E^{D-1} \sum_{l=1}^\infty e^{-\beta lE} e^{\beta l\mu} \, dE \\
\Rightarrow N|_T &\propto \sum_{l=1}^\infty \frac{e^{\beta\mu l}}{l^D}.
\end{aligned} \tag{C.14}$$

Now, we can maximise N to arrive at the relation for condensation:

$$\boxed{\lim_{\mu \rightarrow 0} \{N|_{T_C}\} \propto \zeta(D)} \tag{C.15}$$

From this limit, we can see that for $D = 1$, the zeta function diverges to infinity. Just as before, this means that the solution is not physical and so *one-dimensional BECs do not exist for massless bosons*.

In two dimensions, however, the zeta function is well-defined and gives a positive answer. This is true for all spatial dimensions, such that $D \geq 2$. Therefore we can conclude that, from an idealised statistical mechanical standpoint, *massless boson BECs are only possible in two or more spatial dimensions*.

This appendix briefly demonstrates the care that needs to be taken when discussing Bose-Einstein condensation in the less than three spatial dimensions. Note that all the calculations are carried out for *non-interacting* particles in a *thermodynamic limit*. In reality, there are many other complications to the theory that are not discussed here [17]. [57]

D

Supplementary Figures

Figures

D.1	Form of a 2D Thomas-Fermi Paraboloid	80
D.2	Development of a Quantum Vortex in an Isotropic Potential	81
D.3	Trapped Vortex-Vortex Pair Interaction (Density)	82
D.4	Trapped Vortex-Vortex Pair Interaction (Phase)	83
D.5	Trapped Vortex-Antivortex Pair Interaction (Density)	84
D.6	Trapped Vortex-Antivortex Pair Interaction (Phase)	85
D.7	Macroscopic Density Fluctuation in an Isotropic Potential (Density)	86
D.8	Macroscopic Density Fluctuation in an Isotropic Potential (Phase)	87
D.9	Trapped Anisotropic 19 Vortex Lattice Evolution (Density)	88
D.10	Trapped Anisotropic 19 Vortex Lattice Evolution (Phase)	89
D.11	Trapped Anisotropic 19 Vortex-Antivortex Lattice Evolution (Density)	90
D.12	Trapped Anisotropic 19 Vortex-Antivortex Lattice Evolution (Phase)	91
D.13	Anisotropic 19 Vortex Lattice Free Expansion (Density)	92
D.14	Anisotropic 19 Vortex Lattice Free Expansion (Phase)	93
D.15	Vortex Density Tests - Anisotropic 7 Vortex Lattice (Density)	94
D.16	Vortex Density Tests - Anisotropic 7 Vortex Lattice (Phase)	95
D.17	Vortex Density Tests - Anisotropic 19 Vortex Lattice (Density)	96
D.18	Vortex Density Tests - Anisotropic 19 Vortex Lattice (Phase)	97
D.19	Vortex Density Tests - Anisotropic 37 Vortex Lattice (Density)	98
D.20	Vortex Density Tests - Anisotropic 37 Vortex Lattice (Phase)	99
D.21	Vortex Density Tests - Anisotropic 61 Vortex Lattice (Density)	100
D.22	Vortex Density Tests - Anisotropic 61 Vortex Lattice (Phase)	101

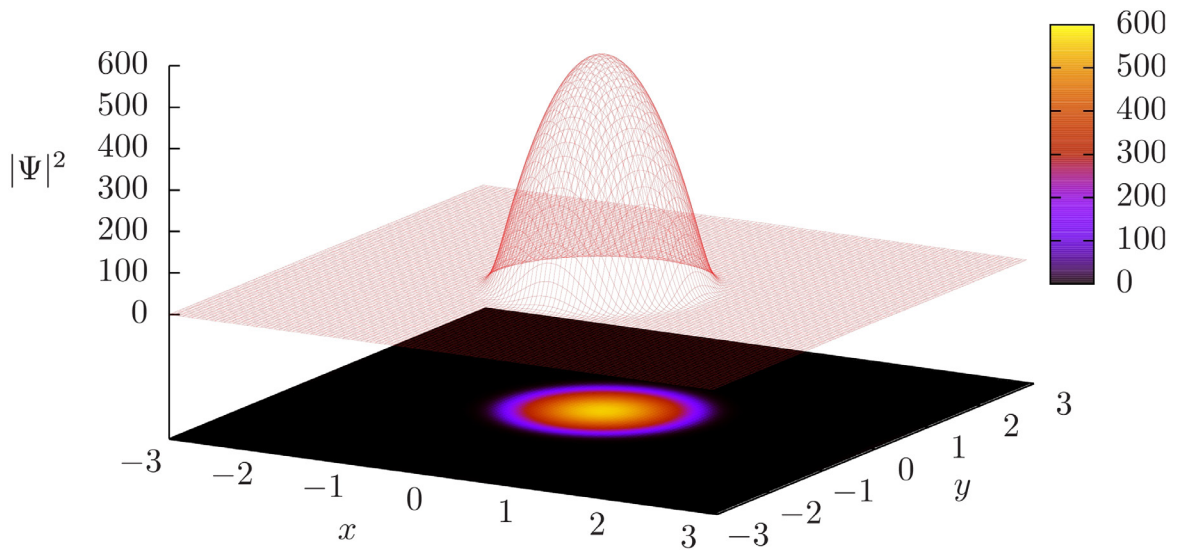


Figure D.1: The form of the unnormalised probability density, $|\Psi|^2$, subject to a uniform potential well, after an imaginary time interval of $10^{-3}i$ [d.u.]. The initial form of the wavefunction was $|\Psi_0|^2 \propto e^{-2(x^2+y^2)}$ and the imaginary time evolution consisted of 10^4 iterations of a $10^{-7}i$ [d.u.] imaginary time-step. The two-dimensional square lattice has $n^2 = 120^2$ points and so the axes in the figure are discretised into intervals of $h = 0.05$. The interaction constant is $g = 10$ [d.u.], the angular frequencies are $\omega_x = \omega_y = 100$ [d.u.] and the particle number is $N = 1000$.

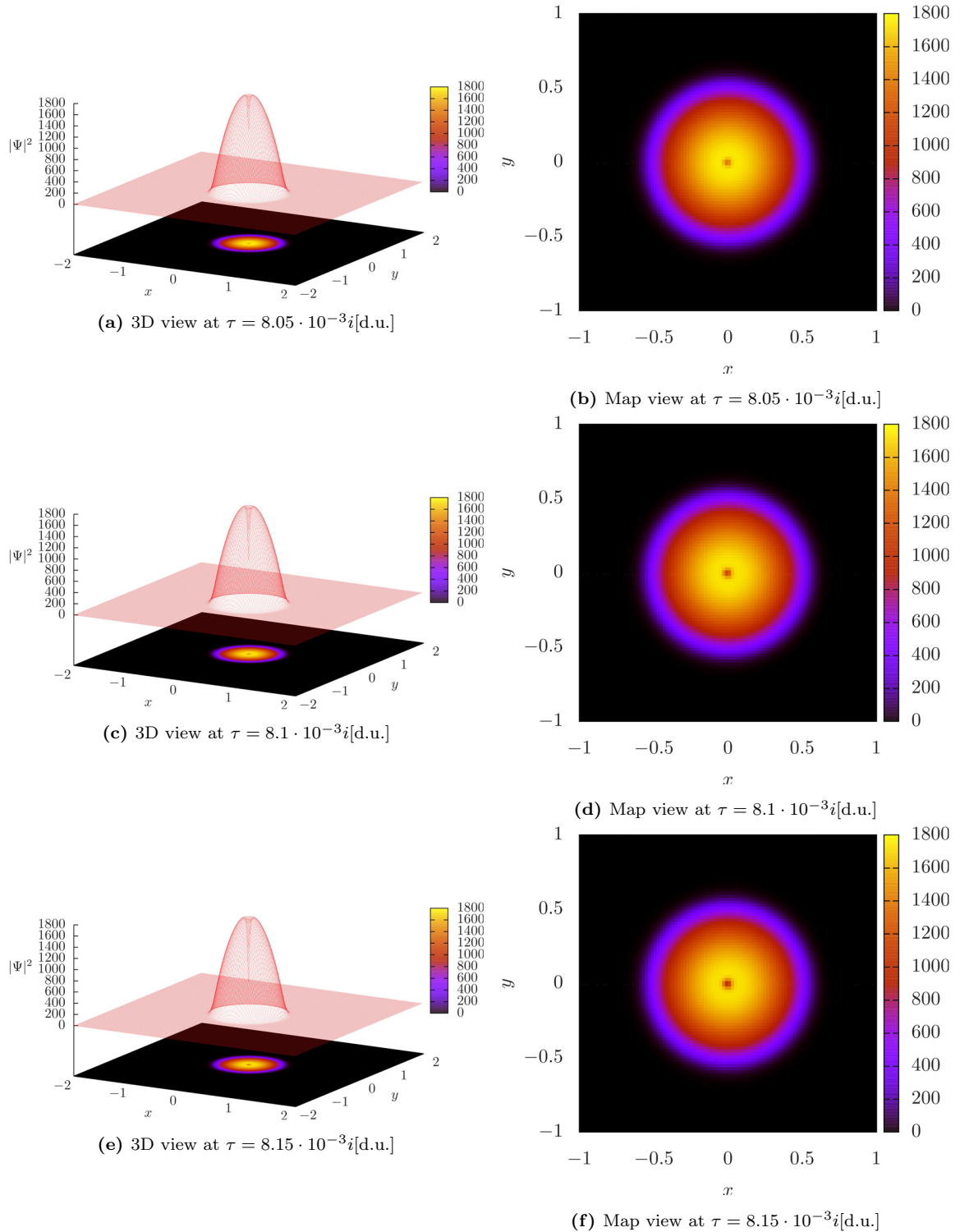


Figure D.2: The development of the quantum vortex in the unnormalised probability density distribution, $|\Psi|^2$, subject to an isotropic potential, after imaginary time intervals of $8.05 \cdot 10^{-3}i$ [d.u.], $8.1 \cdot 10^{-3}i$ [d.u.] and $8.15 \cdot 10^{-3}i$ [d.u.], respectively. The square lattice has $n^2 = 200^2$ points and so the axes, which are all defined from -2 to 2, are discretised into intervals of $h = 0.02$. $\{g = 1\text{[d.u.]}, \omega_x = \omega_y = 100\text{[d.u.]}, N = 1000\}$

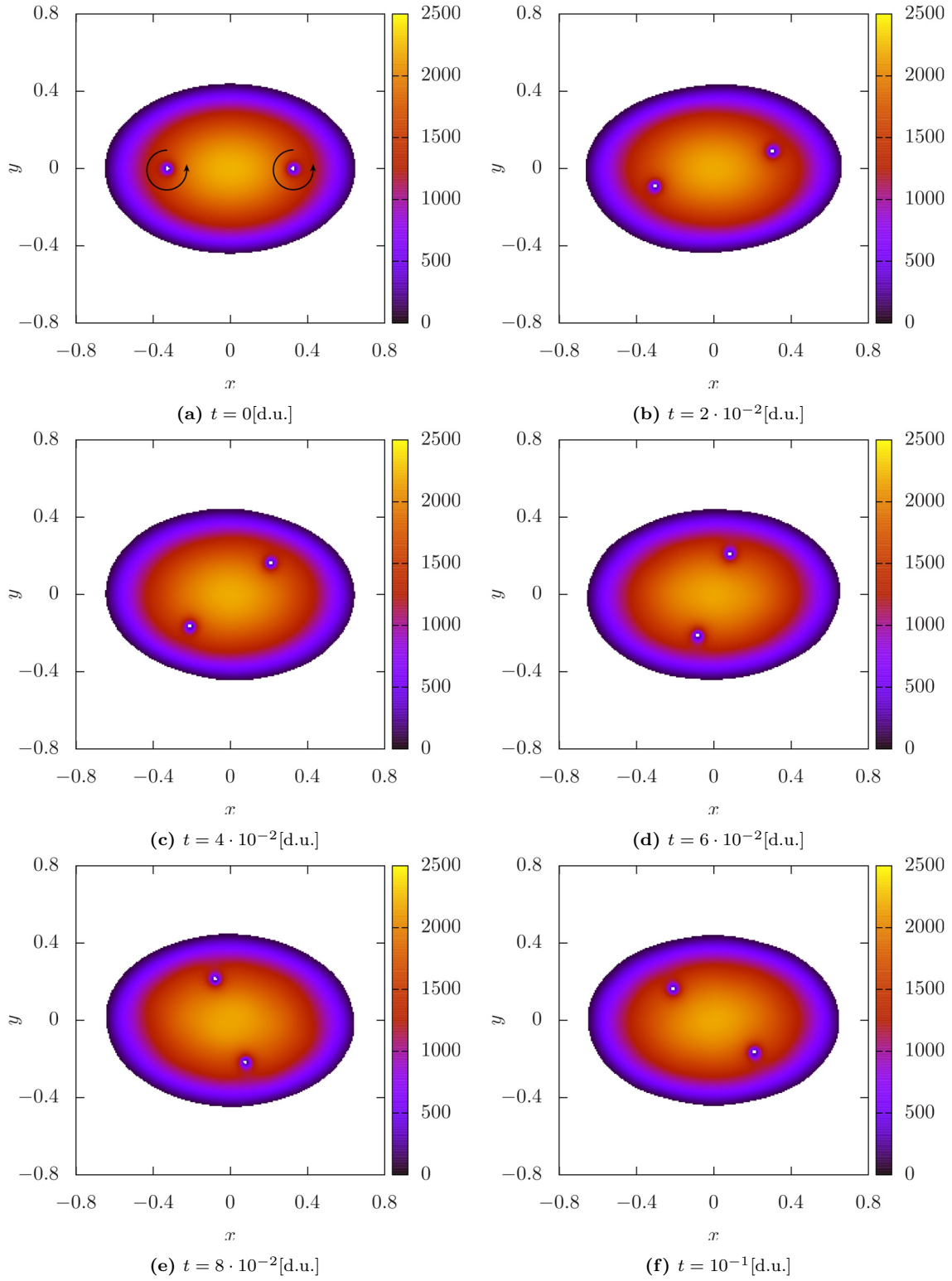


Figure D.3: Density plots of the real-time evolution of a pair of identical vortices in the unnormalised probability density distribution, $|\Psi|^2$, subject to an anisotropic potential, in time intervals of $2 \cdot 10^{-2}$ [d.u.]. The total real-time evolution consisted of 10^4 iterations of a 10^{-5} [d.u.] time-step. The square lattice has $n^2 = 600^2$ points and so the axes, which are all defined from -2 to 2, are discretised into intervals of $h = 1/150$. $\{|\Psi|^2 > 100\text{[d.u.]}, g = 1\text{[d.u.]}, \omega_x = 100\text{[d.u.]}, \omega_y = 150\text{[d.u.]}, N = 1000\}$

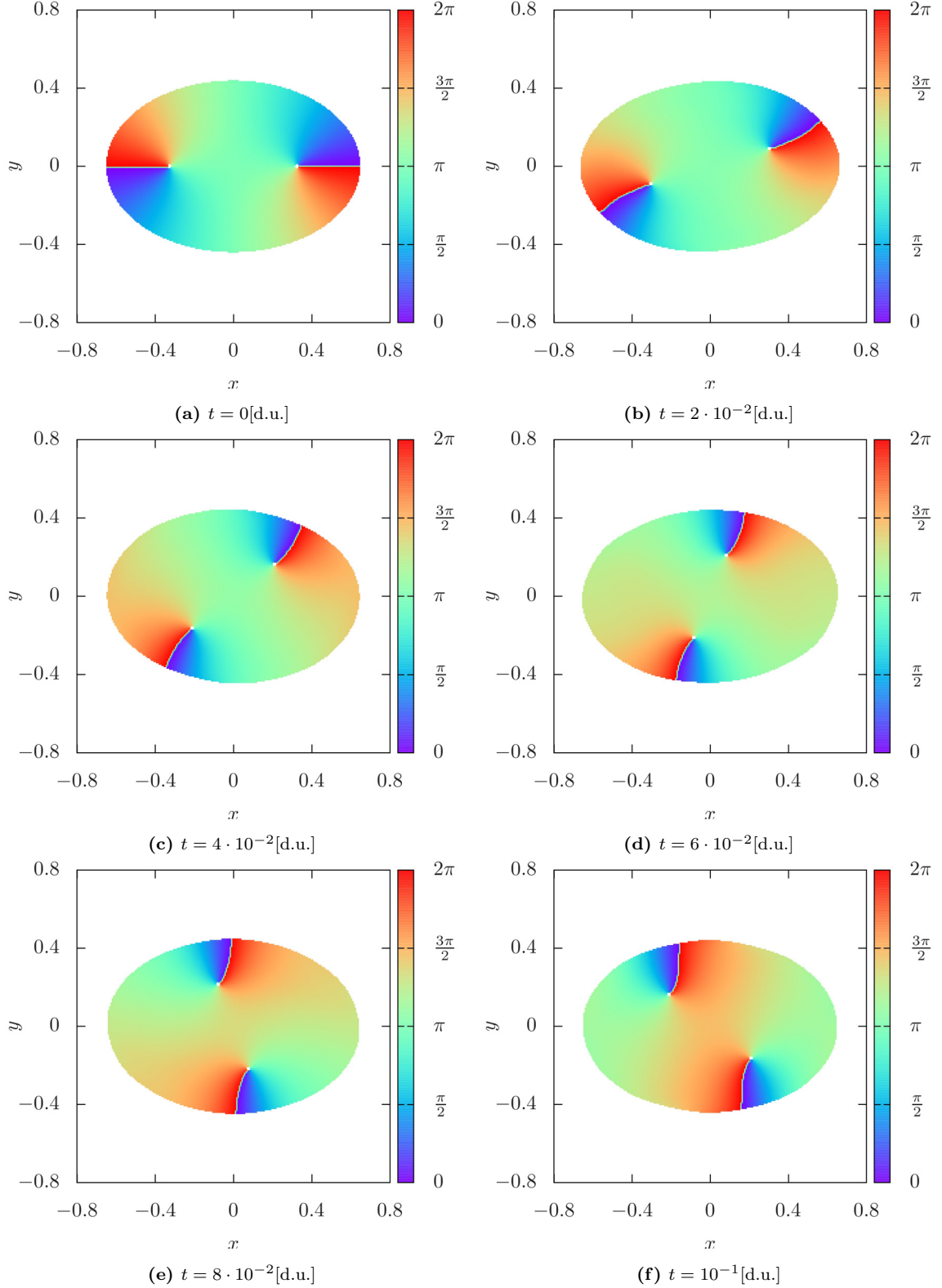


Figure D.4: Phase plots of the real-time evolution of a pair of identical vortices, subject to an anisotropic potential, in time intervals of $2 \cdot 10^{-2}[\text{d.u.}]$. The total real-time evolution consisted of 10^4 iterations of a $10^{-5}[\text{d.u.}]$ time-step. The square lattice has $n^2 = 600^2$ points and so the axes, which are all defined from -2 to 2, are discretised into intervals of $h = 1/150$. $\{|\Psi|^2 > 100[\text{d.u.}]\}$, $g = 1[\text{d.u.}]$, $\omega_x = 100[\text{d.u.}]$, $\omega_y = 150[\text{d.u.}]$, $N = 1000$

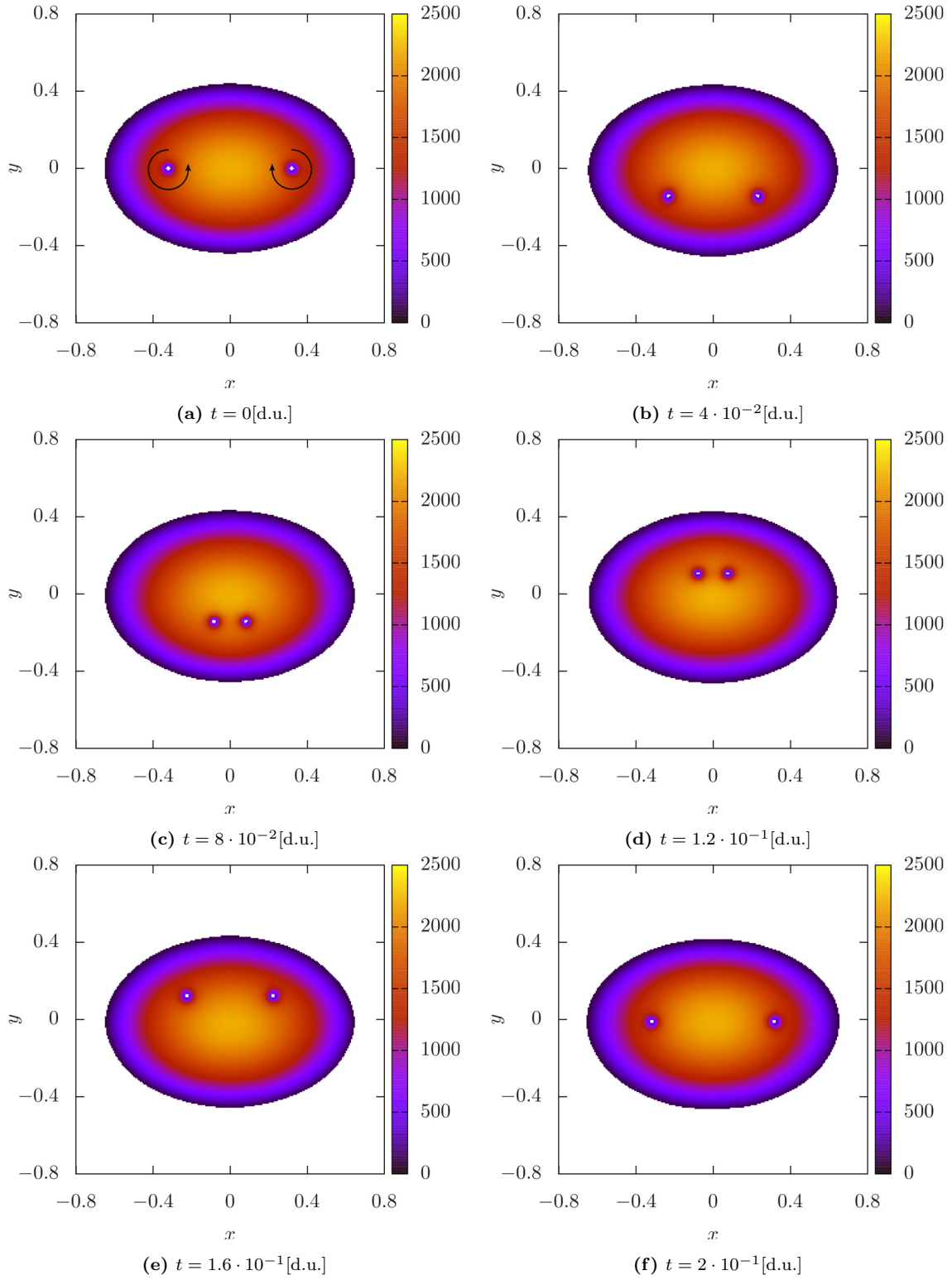


Figure D.5: Density plots of the real-time evolution of a vortex-antivortex pair in the unnormalised probability density distribution, $|\Psi|^2$, subject to an anisotropic potential, in time intervals of $4 \cdot 10^{-2}$ [d.u.]. The total real-time evolution consisted of $2 \cdot 10^4$ iterations of a 10^{-5} [d.u.] time-step. The square lattice has $n^2 = 600^2$ points and so the axes, which are all defined from -2 to 2, are discretised into intervals of $h = 1/150$. $\{|\Psi|^2 > 100\text{[d.u.]}, g = 1\text{[d.u.]}, \omega_x = 100\text{[d.u.]}, \omega_y = 150\text{[d.u.]}, N = 1000\}$

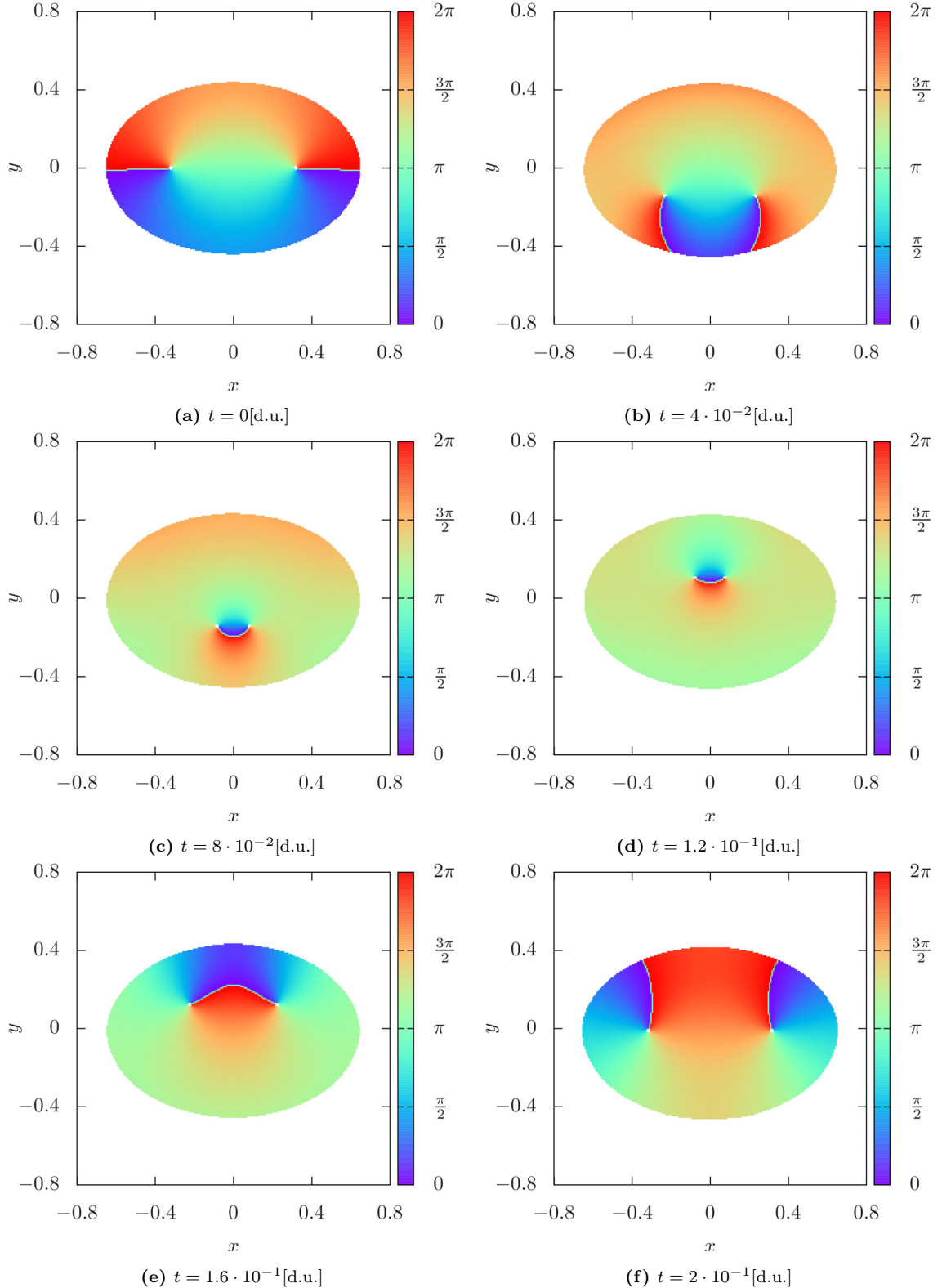


Figure D.6: Phase plots of the real-time evolution of a vortex-antivortex pair, subject to an anisotropic potential, in time intervals of $4 \cdot 10^{-2}$ [d.u.]. The total real-time evolution consisted of $2 \cdot 10^4$ iterations of a 10^{-5} [d.u.] time-step. The square lattice has $n^2 = 600^2$ points and so the axes, which are all defined from -2 to 2, are discretised into intervals of $h = 1/150$. $\{|\Psi|^2 > 100\}$ [d.u.], $g = 1$ [d.u.], $\omega_x = 100$ [d.u.], $\omega_y = 150$ [d.u.], $N = 1000$

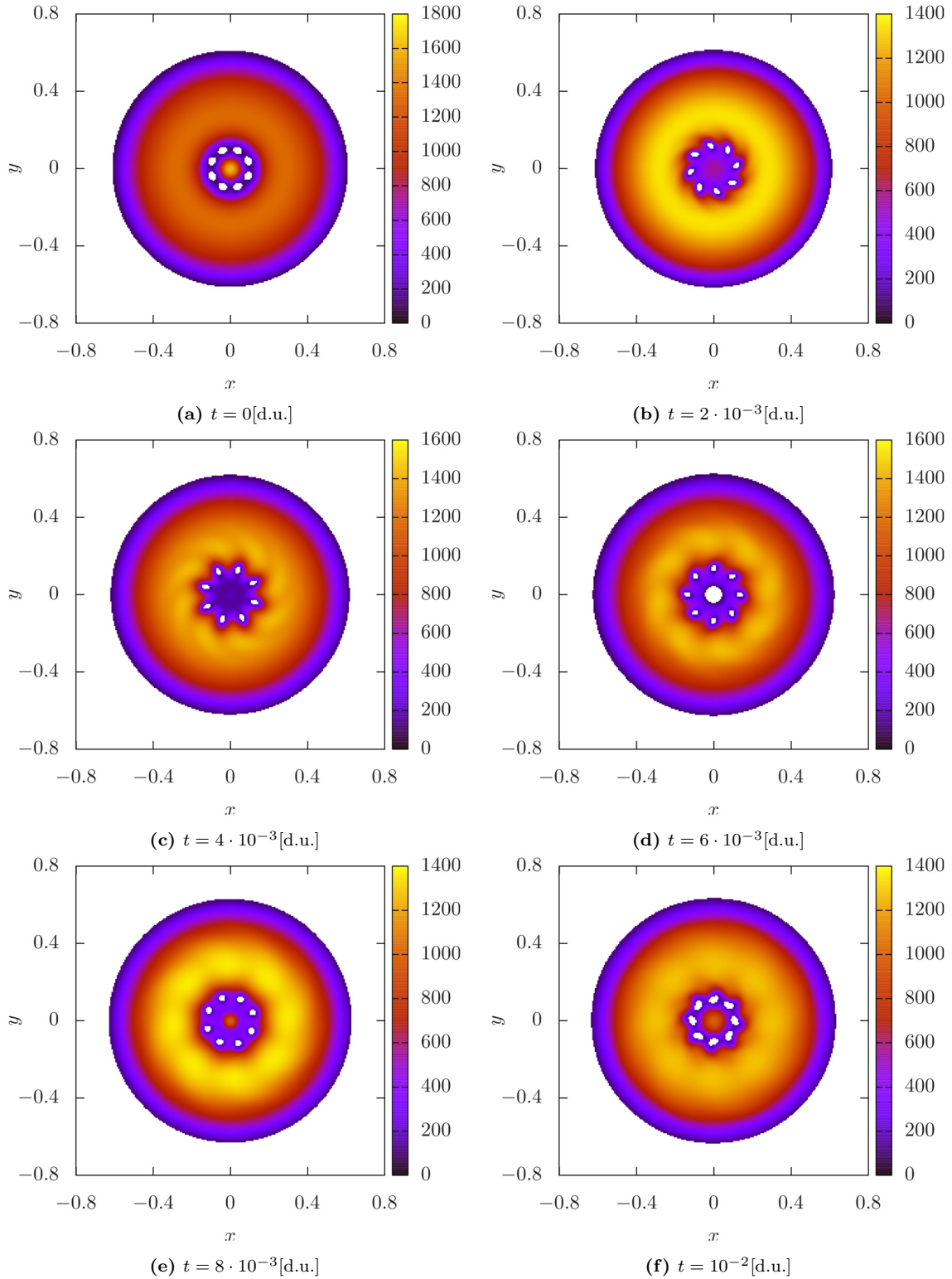


Figure D.7: Density plots of the evolution of a macroscopic density fluctuation in the unnormalised probability density distribution, $|\Psi|^2$, subject to an isotropic potential, in time intervals of $2 \cdot 10^{-3}$ [d.u.]. The total real-time evolution consisted of 10^3 iterations of a 10^{-5} [d.u.] time-step. The square lattice has $n^2 = 600^2$ points and so the axes, which are all defined from -2 to 2, are discretised into intervals of $h = 1/150$. $\{|\Psi|^2 > 100\}$ [d.u.], $g = 1$ [d.u.], $\omega_x = \omega_y = 100$ [d.u.], $N = 1000$

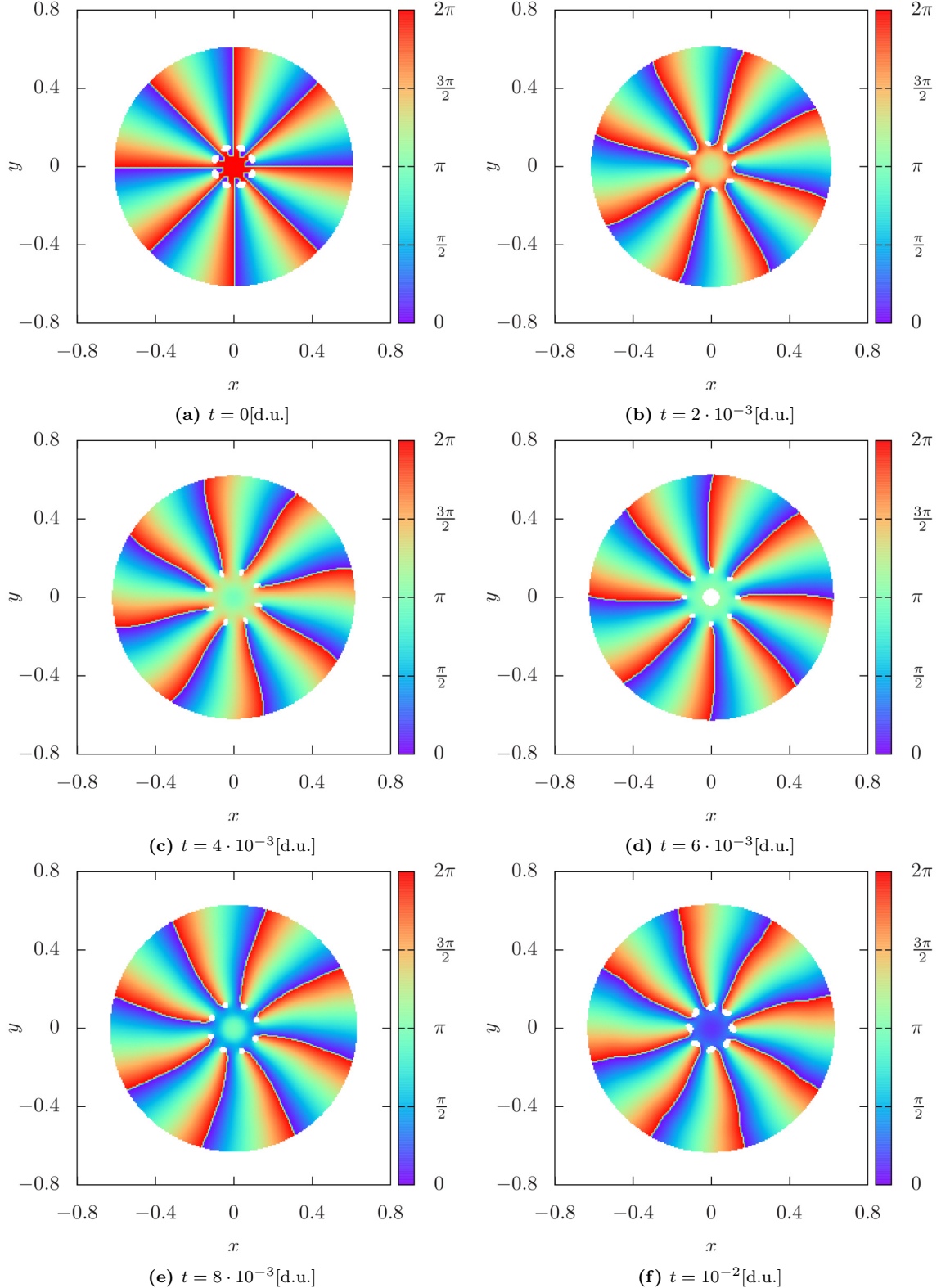


Figure D.8: Phase plots of the evolution of a macroscopic density fluctuation, subject to an isotropic potential, in time intervals of $2 \cdot 10^{-3}$ [d.u.]. The total real-time evolution consisted of 10^3 iterations of a 10^{-5} [d.u.] time-step. The square lattice has $n^2 = 600^2$ points and so the axes, which are all defined from -2 to 2, are discretised into intervals of $h = 1/150$. $\{|\Psi|^2 > 100\text{[d.u.]}, g = 1\text{[d.u.]}, \omega_x = \omega_y = 100\text{[d.u.]}, N = 1000\}$

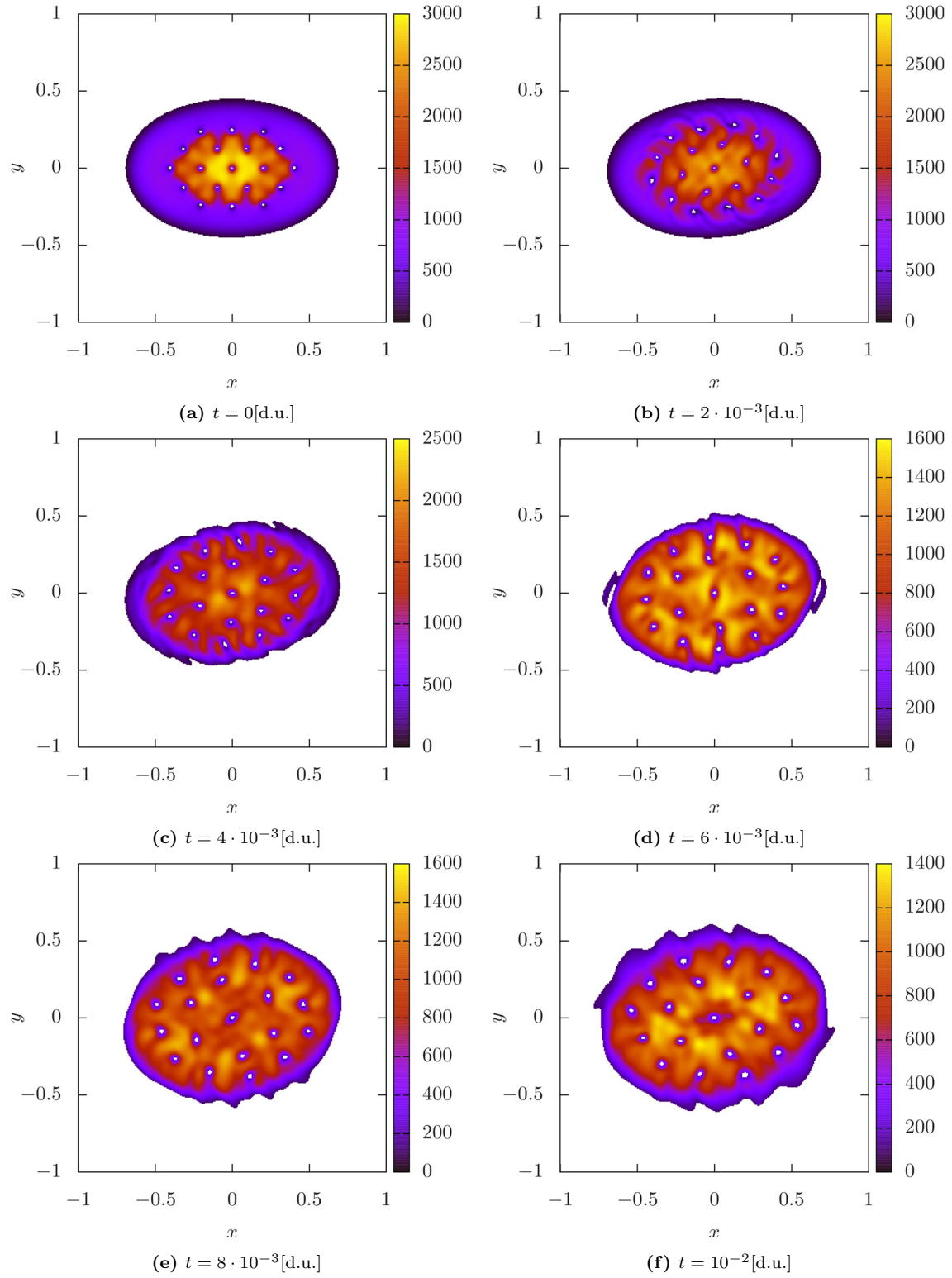


Figure D.9: Density plots of the real-time evolution of an fcc lattice of 19 identical vortices in the unnormalised probability density distribution, $|\Psi|^2$, subject to an anisotropic potential, in time intervals of $2 \cdot 10^{-3}[\text{d.u.}]$. The total real-time evolution consisted of 10^3 iterations of a $10^{-5}[\text{d.u.}]$ time-step. The square lattice has $n^2 = 600^2$ points and so the axes, which are all defined from -2 to 2, are discretised into intervals of $h = 1/150$. $\{|\Psi|^2 > 100[\text{d.u.}], g = 1[\text{d.u.}], \omega_x = 100[\text{d.u.}], \omega_y = 150[\text{d.u.}], N = 1000\}$

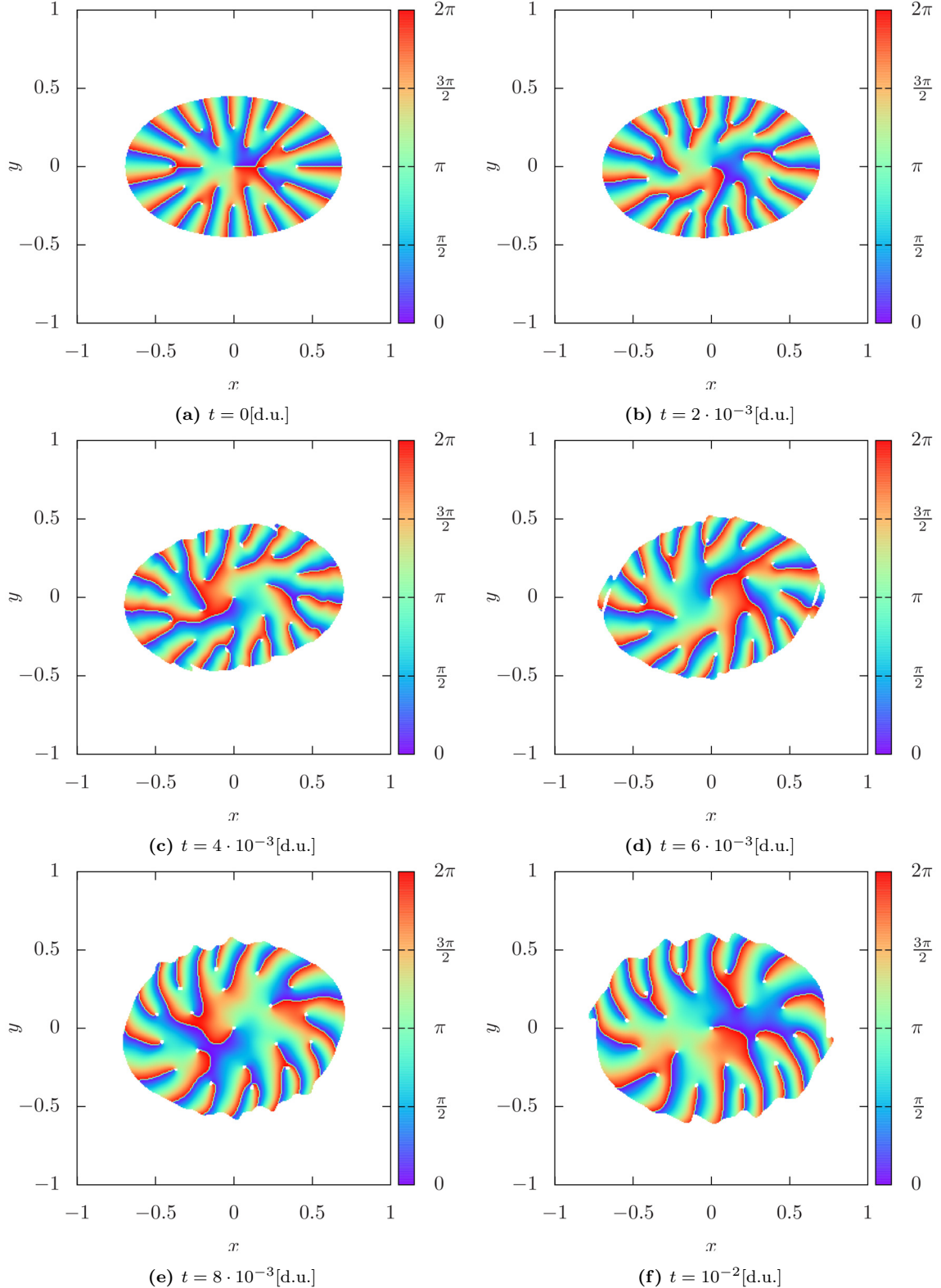


Figure D.10: Phase plots of the real-time evolution of an fcc lattice of 19 identical vortices, subject to an anisotropic potential, in time intervals of $2 \cdot 10^{-3}$ [d.u.]. The total real-time evolution consisted of 10^3 iterations of a 10^{-5} [d.u.] time-step. The square lattice has $n^2 = 600^2$ points and so the axes, which are all defined from -2 to 2, are discretised into intervals of $h = 1/150$. $\{|\Psi|^2 > 100\text{[d.u.]}, g = 1\text{[d.u.]}, \omega_x = 100\text{[d.u.]}, \omega_y = 150\text{[d.u.]}, N = 1000\}$

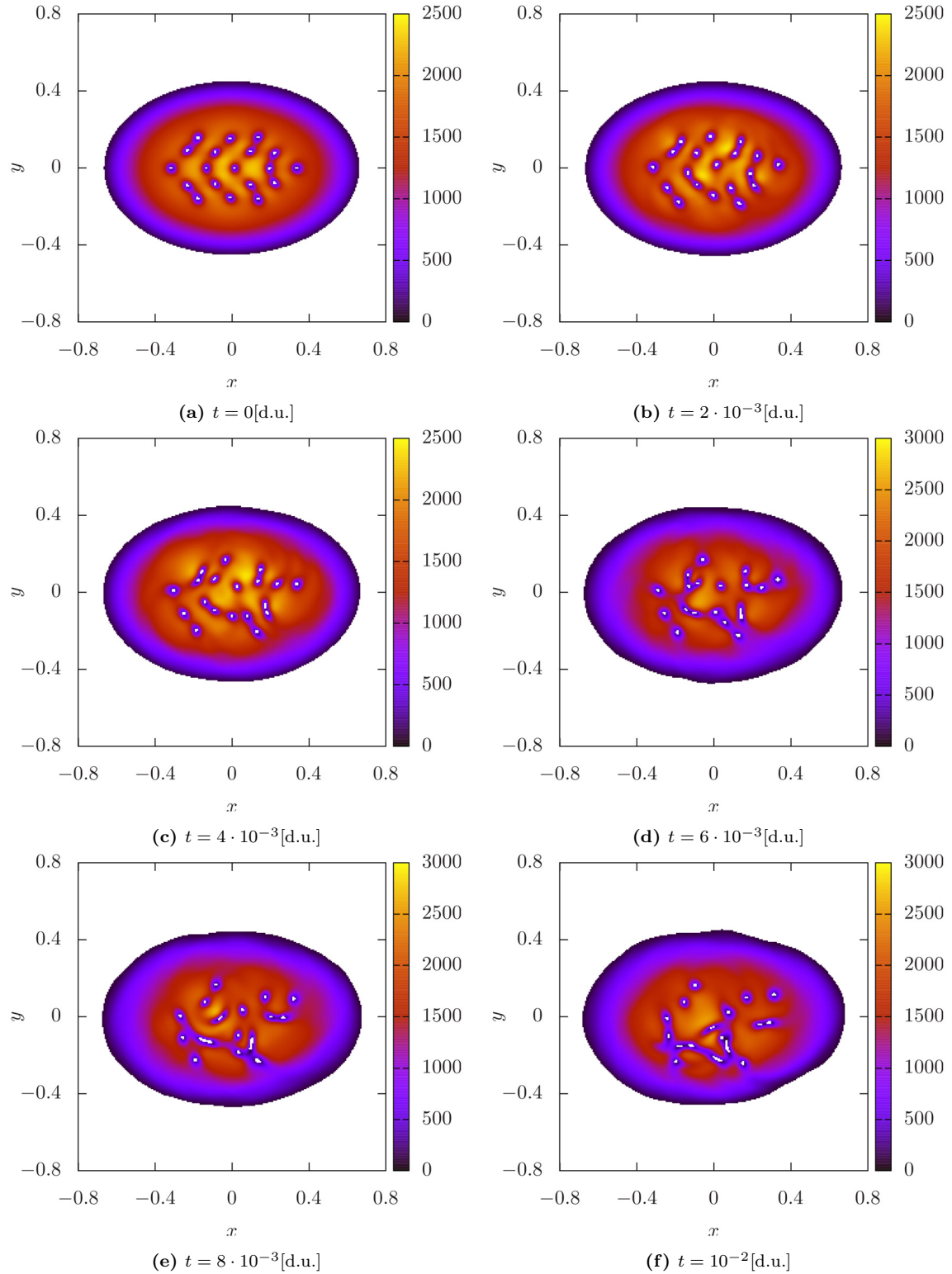


Figure D.11: Density plots of the real-time evolution of an fcc 19 vortex-antivortex lattice in the unnormalised probability density distribution, $|\Psi|^2$, subject to an anisotropic potential, in time intervals of $2 \cdot 10^{-3}$ [d.u.]. The total real-time evolution consisted of 10^3 iterations of a 10^{-5} [d.u.] time-step. The square lattice has $n^2 = 600^2$ points and so the axes, which are all defined from -2 to 2, are discretised into intervals of $h = 1/150$. $\{|\Psi|^2 > 100$ [d.u.], $g = 1$ [d.u.], $\omega_x = 100$ [d.u.], $\omega_y = 150$ [d.u.], $N = 1000\}$

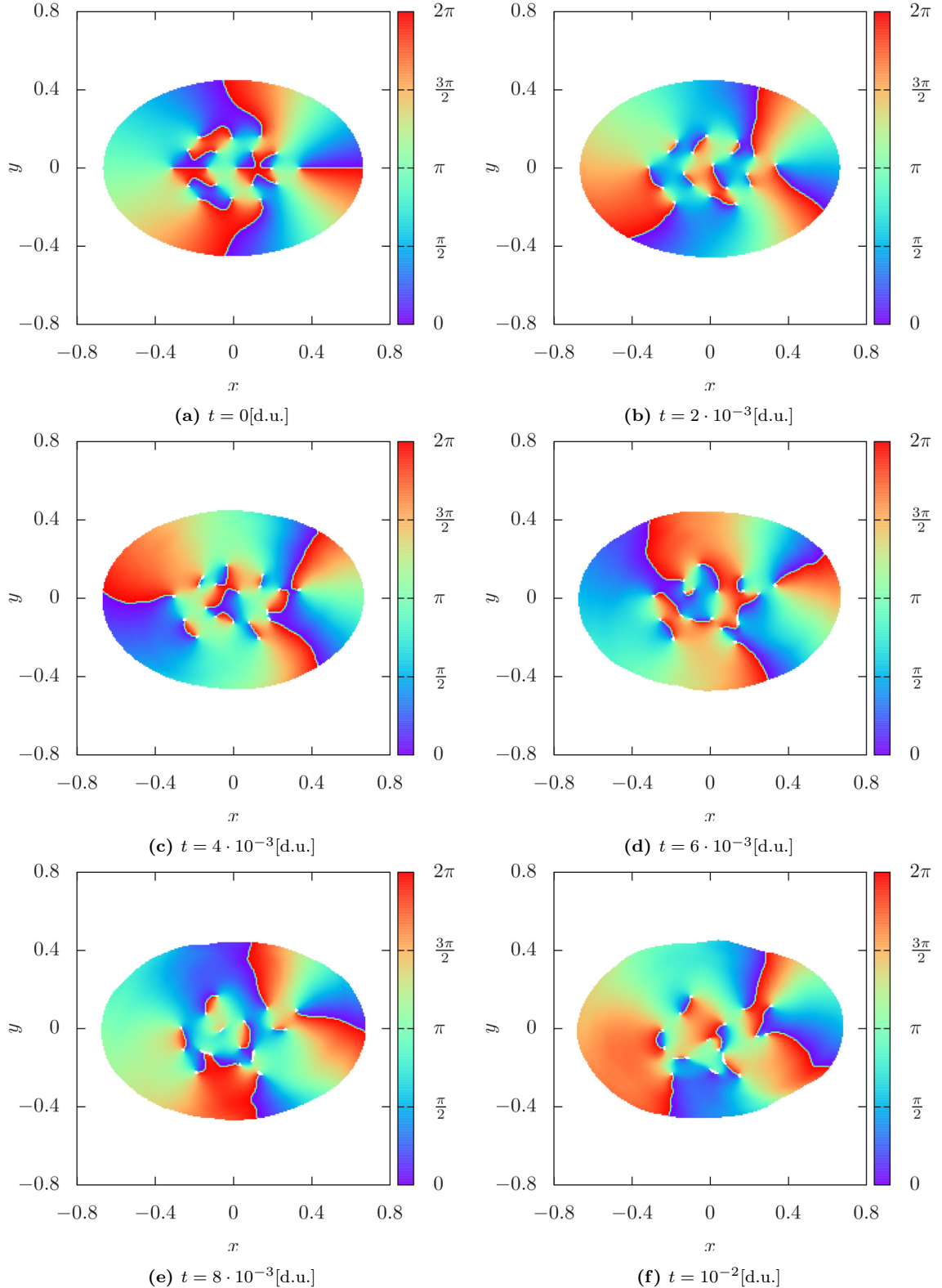


Figure D.12: Phase plots of the real-time evolution of an fcc 19 vortex-antivortex lattice, subject to an anisotropic potential, in time intervals of $2 \cdot 10^{-3}$ [d.u.]. The total real-time evolution consisted of 10^3 iterations of a 10^{-5} [d.u.] time-step. The square lattice has $n^2 = 600^2$ points and so the axes, which are all defined from -2 to 2, are discretised into intervals of $h = 1/150$. $\{|\Psi|^2 > 100\text{[d.u.]}, g = 1\text{[d.u.]}, \omega_x = 100\text{[d.u.]}, \omega_y = 150\text{[d.u.]}, N = 1000\}$

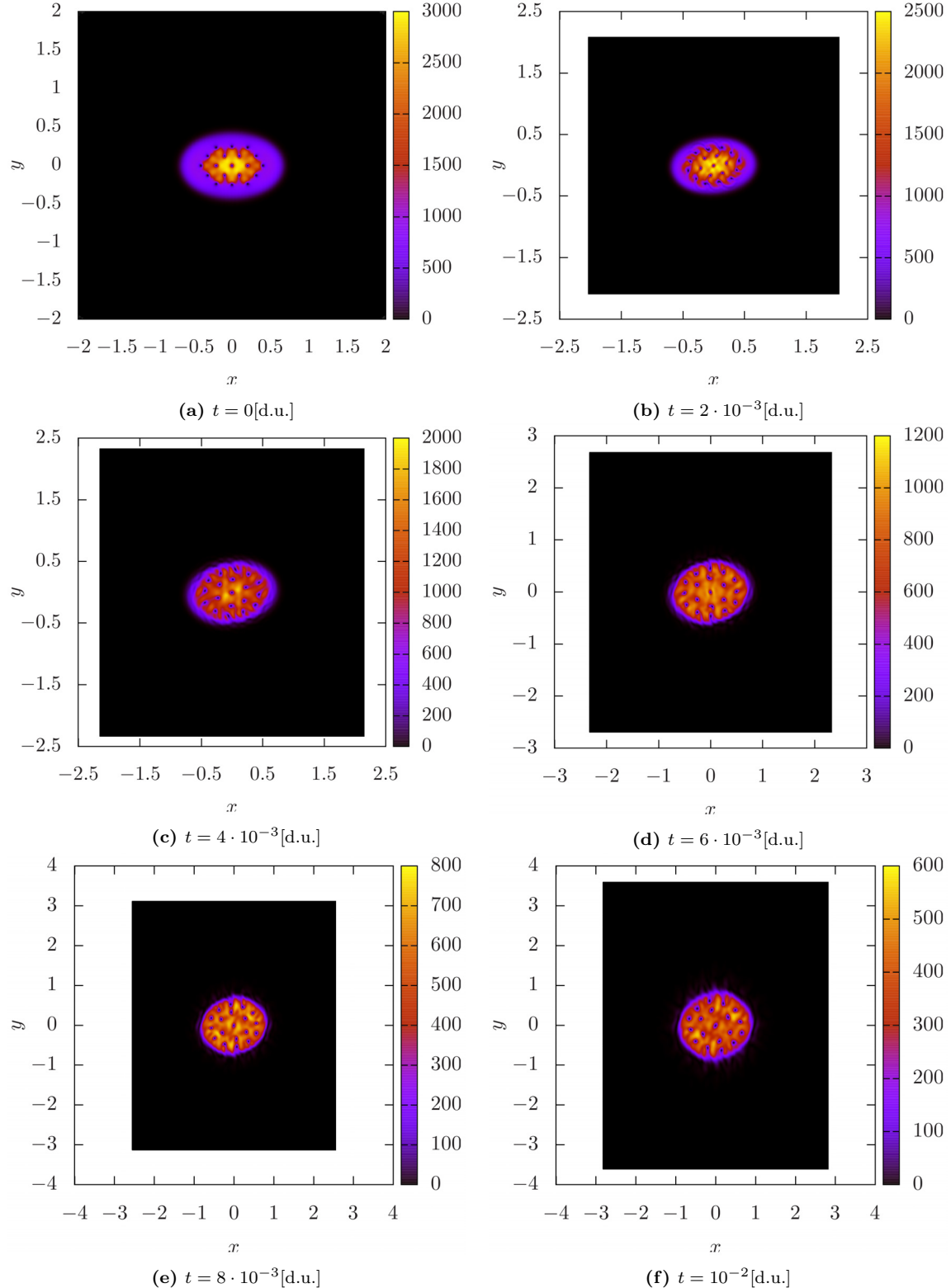


Figure D.13: Density plots of the real-time expansion of an fcc lattice of 19 identical vortices in the unnormalised probability density distribution, $|\Psi|^2$, in time intervals of $2 \cdot 10^{-3}[\text{d.u.}]$. The total real-time evolution consisted of 10^3 iterations of a $10^{-5}[\text{d.u.}]$ time-step. Initially, the square lattice had $n^2 = 600^2$ points and so the axes are discretised into intervals of $h = 1/150$. $\{|\Psi|^2 > 1[\text{d.u.}], g = 1[\text{d.u.}], \omega_x = 100[\text{d.u.}], \omega_y = 150[\text{d.u.}], N = 1000\}$

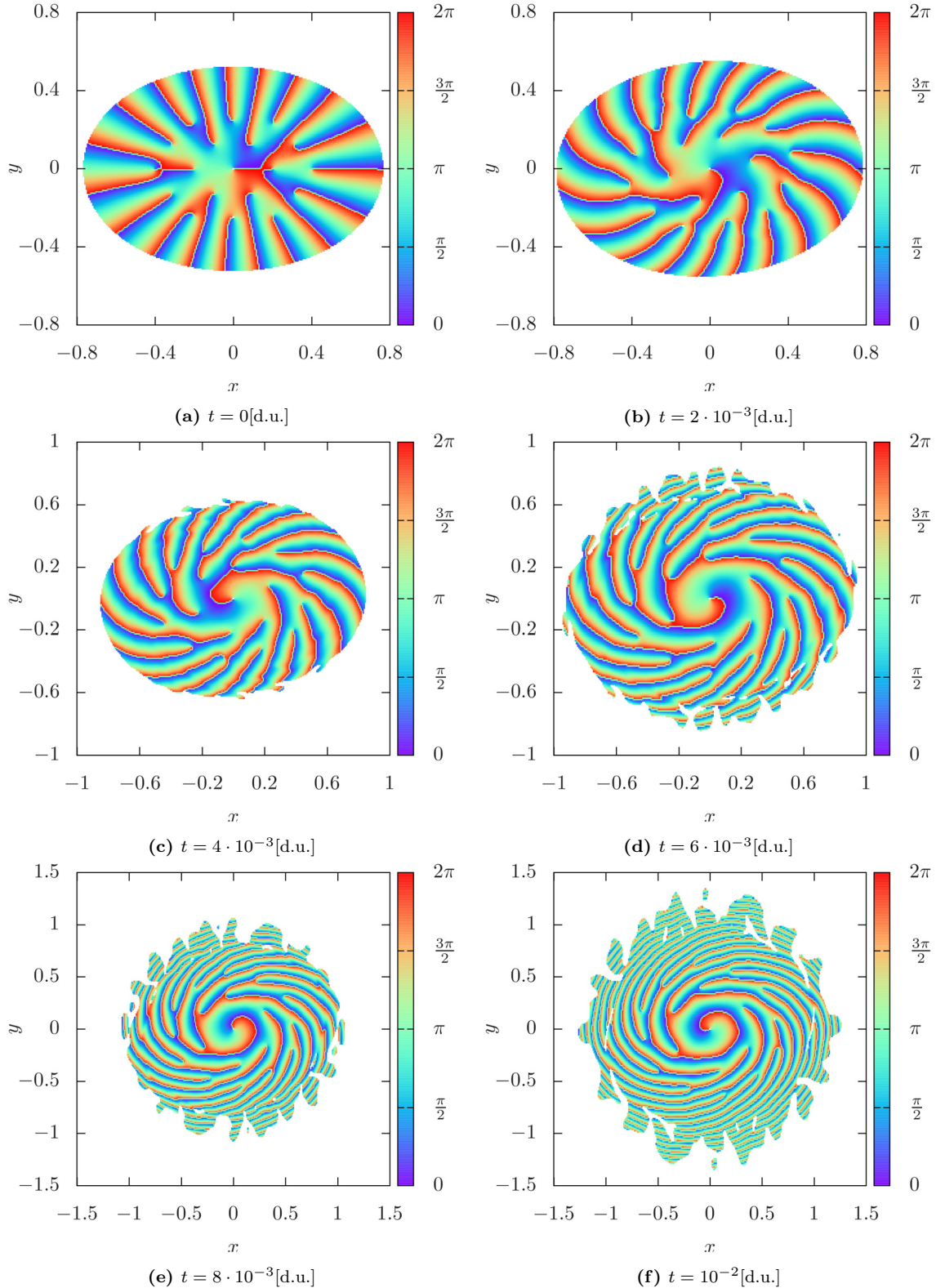


Figure D.14: Phase plots of the real-time expansion of an fcc lattice of 19 identical vortices, in time intervals of $2 \cdot 10^{-3}[\text{d.u.}]$. The total real-time evolution consisted of 10^3 iterations of a $10^{-5}[\text{d.u.}]$ time-step. Initially, the square lattice had $n^2 = 600^2$ points and so the axes are discretised into intervals of $h = 1/150$. $\{|\Psi|^2 > 1[\text{d.u.}], g = 1[\text{d.u.}], \omega_x = 100[\text{d.u.}], \omega_y = 150[\text{d.u.}], N = 1000\}$

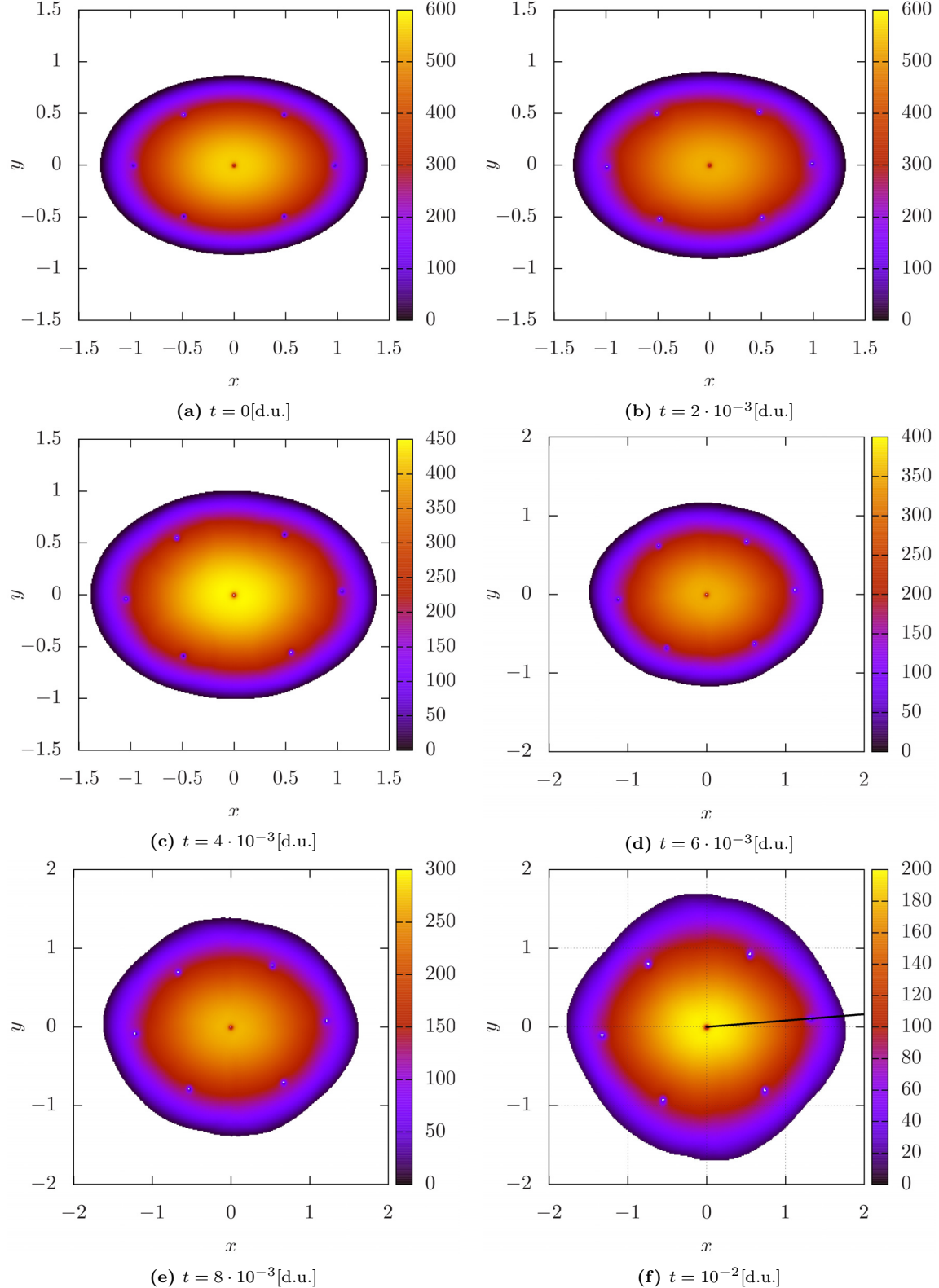


Figure D.15: Density plots of the real-time expansion of an fcc lattice of 7 identical vortices in the unnormalised probability density distribution, $|\Psi|^2$, in time intervals of $2 \cdot 10^{-3}[\text{d.u.}]$. The total real-time evolution consisted of 10^3 iterations of a $10^{-5}[\text{d.u.}]$ time-step. Initially, the square lattice had $n^2 = 1000^2$ points and so the axes, which were defined from -4 to 4, are discretised into intervals of $h = 1/125$. $\{|\Psi|^2 > 10[\text{d.u.}], g = 15[\text{d.u.}], \omega_x = 100[\text{d.u.}], \omega_y = 150[\text{d.u.}], N = 1000\}$

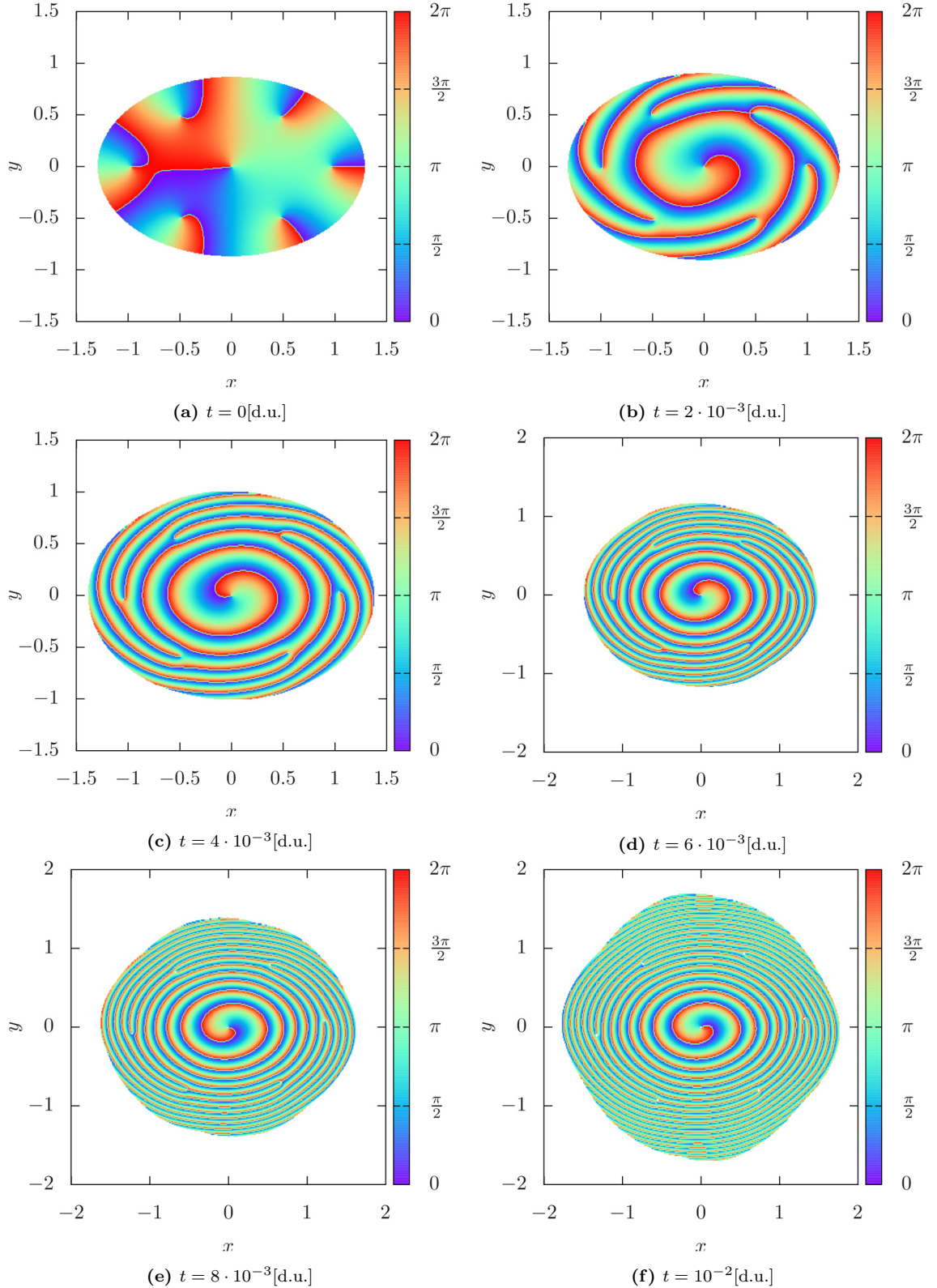


Figure D.16: Phase plots of the real-time expansion of an fcc lattice of 7 identical vortices, in time intervals of $2 \cdot 10^{-3}$ [d.u.]. The total real-time evolution consisted of 10^3 iterations of a 10^{-5} [d.u.] time-step. Initially, the square lattice had $n^2 = 1000^2$ points and so the axes, which were defined from -4 to 4, are discretised into intervals of $h = 1/125$. $\{|\Psi|^2 > 10\}$ [d.u.], $g = 15$ [d.u.], $\omega_x = 100$ [d.u.], $\omega_y = 150$ [d.u.], $N = 1000$

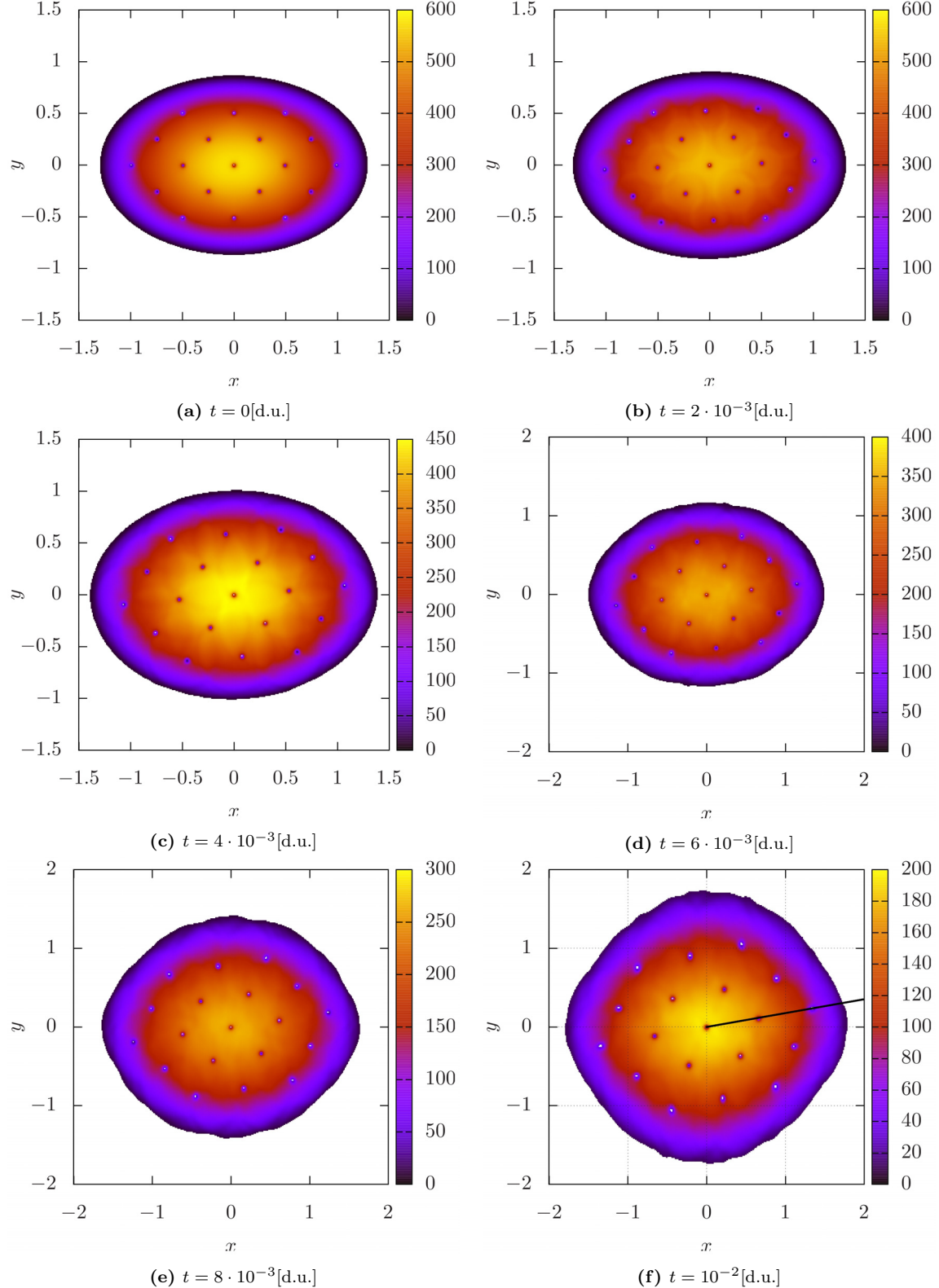


Figure D.17: Density plots of the real-time expansion of an fcc lattice of 19 identical vortices in the unnormalised probability density distribution, $|\Psi|^2$, in time intervals of $2 \cdot 10^{-3}$ [d.u.]. The total real-time evolution consisted of 10^3 iterations of a 10^{-5} [d.u.] time-step. Initially, the square lattice had $n^2 = 1000^2$ points and so the axes, which were defined from -4 to 4, are discretised into intervals of $h = 1/125$. $\{|\Psi|^2 > 10$ [d.u.], $g = 15$ [d.u.], $\omega_x = 100$ [d.u.], $\omega_y = 150$ [d.u.], $N = 1000\}$

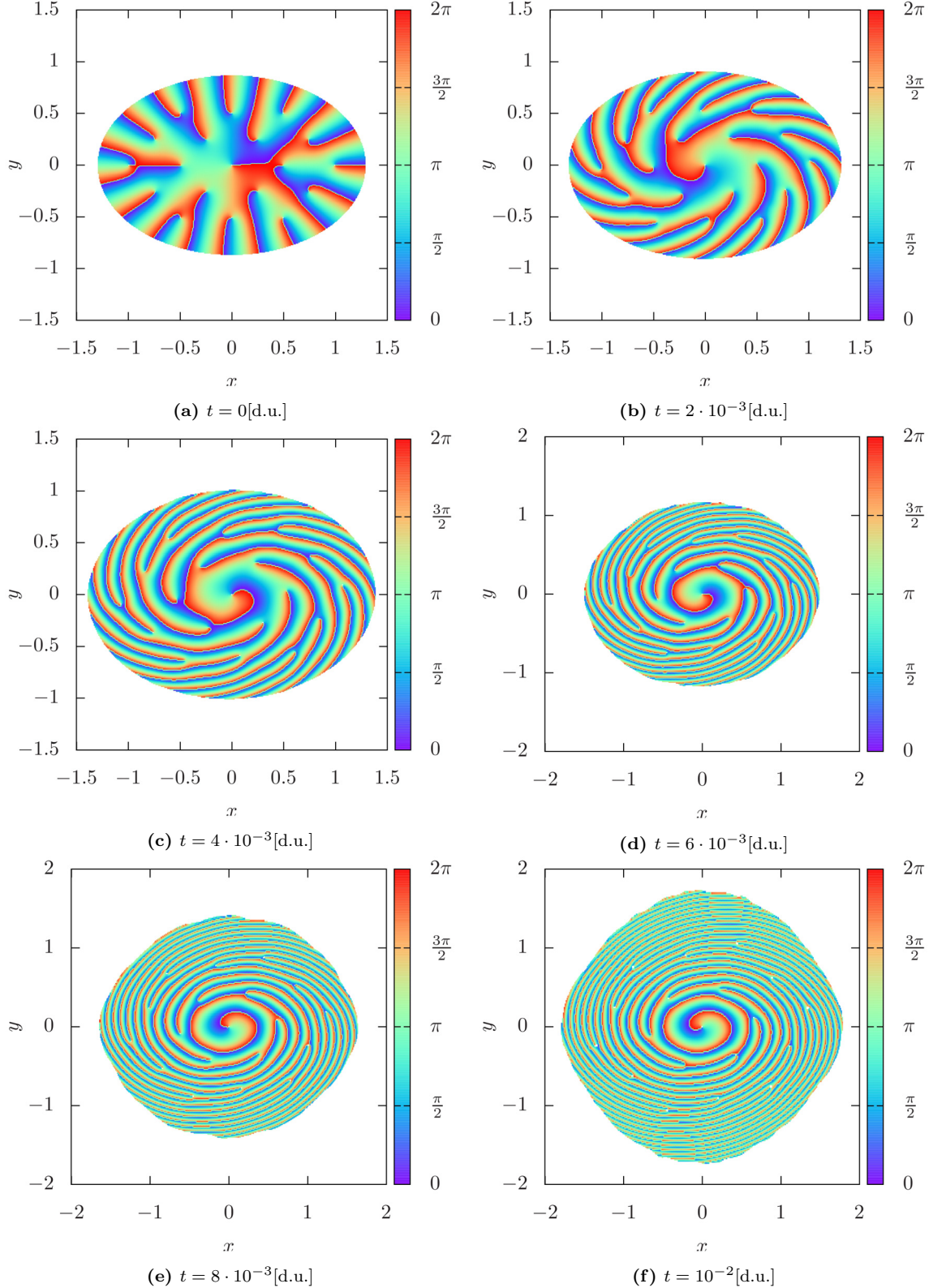


Figure D.18: Phase plots of the real-time expansion of an fcc lattice of 19 identical vortices, in time intervals of $2 \cdot 10^{-3}$ [d.u.]. The total real-time evolution consisted of 10^3 iterations of a 10^{-5} [d.u.] time-step. Initially, the square lattice had $n^2 = 1000^2$ points and so the axes, which were defined from -4 to 4, are discretised into intervals of $h = 1/125$. $\{|\Psi|^2 > 10[\text{d.u.}], g = 15[\text{d.u.}], \omega_x = 100[\text{d.u.}], \omega_y = 150[\text{d.u.}], N = 1000\}$

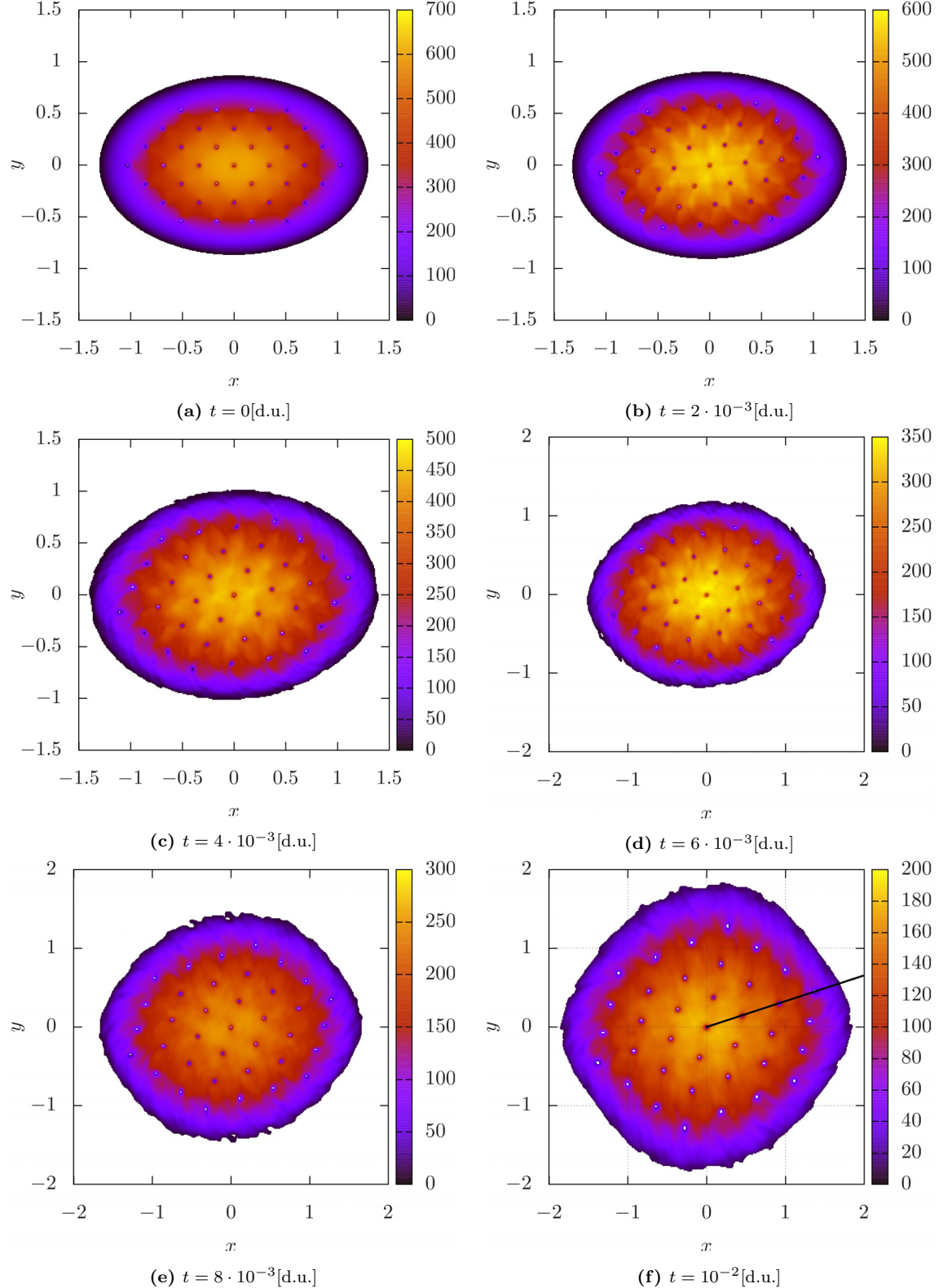


Figure D.19: Density plots of the real-time expansion of an fcc lattice of 37 identical vortices in the unnormalised probability density distribution, $|\Psi|^2$, in time intervals of $2 \cdot 10^{-3}$ [d.u.]. The total real-time evolution consisted of 10^3 iterations of a 10^{-5} [d.u.] time-step. Initially, the square lattice had $n^2 = 1000^2$ points and so the axes, which were defined from -4 to 4, are discretised into intervals of $h = 1/125$. $\{|\Psi|^2 > 10\text{[d.u.]}, g = 15\text{[d.u.]}, \omega_x = 100\text{[d.u.]}, \omega_y = 150\text{[d.u.]}, N = 1000\}$

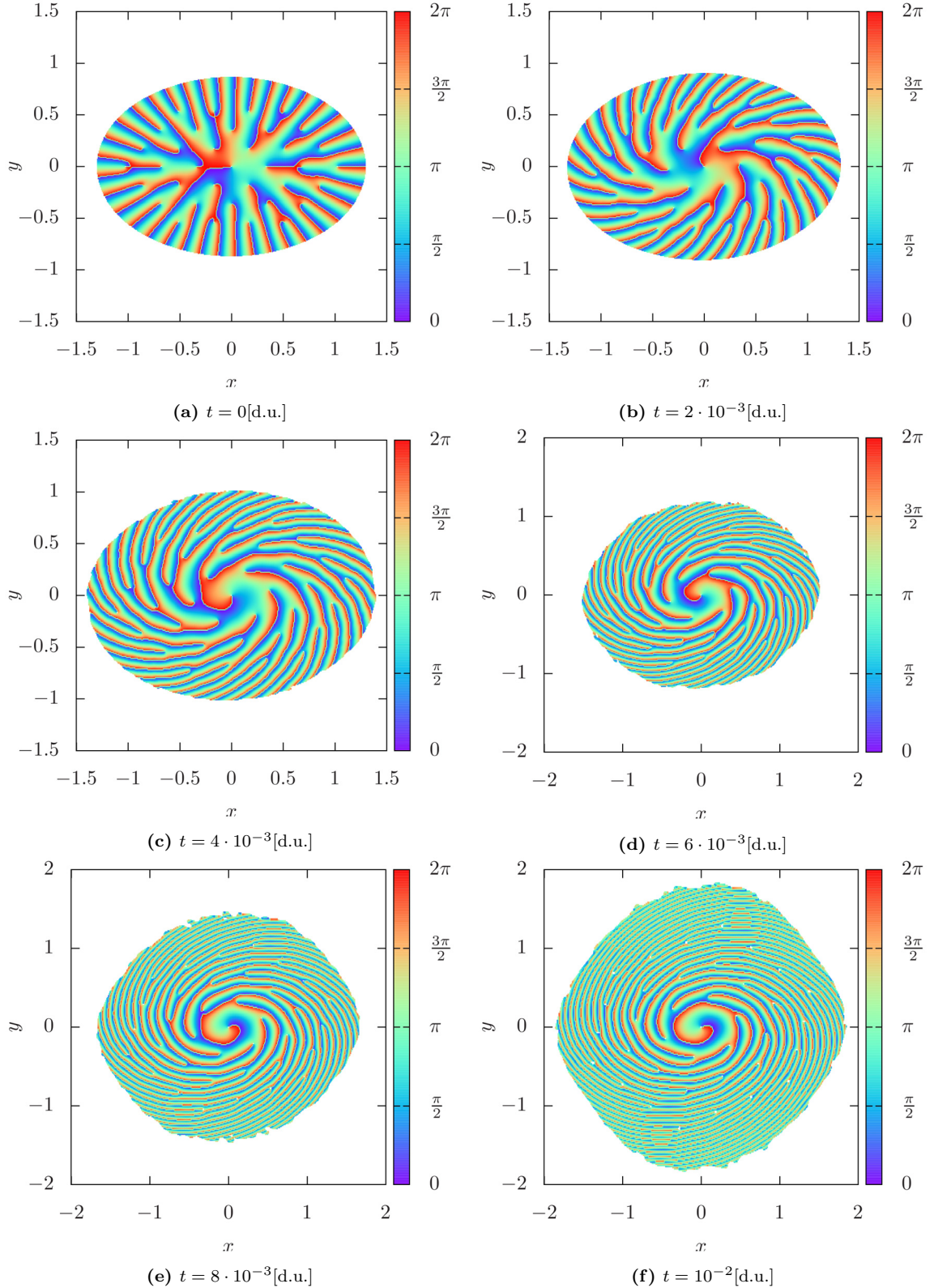


Figure D.20: Phase plots of the real-time expansion of an fcc lattice of 37 identical vortices, in time intervals of $2 \cdot 10^{-3}$ [d.u.]. The total real-time evolution consisted of 10^3 iterations of a 10^{-5} [d.u.] time-step. Initially, the square lattice had $n^2 = 1000^2$ points and so the axes, which were defined from -4 to 4, are discretised into intervals of $h = 1/125$. $\{|\Psi|^2 > 10\}$ [d.u.], $g = 15$ [d.u.], $\omega_x = 100$ [d.u.], $\omega_y = 150$ [d.u.], $N = 1000$

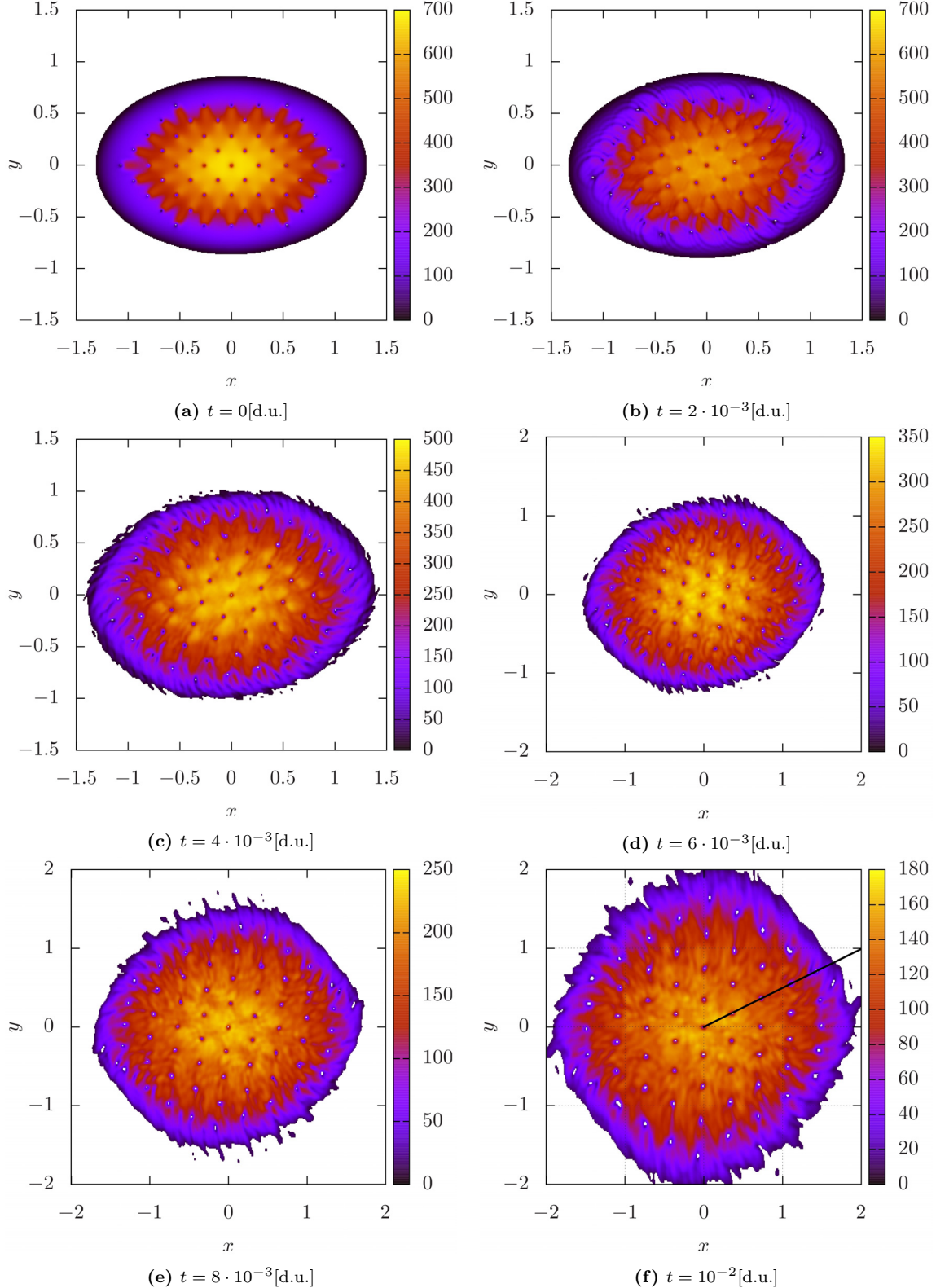


Figure D.21: Density plots of the real-time expansion of an fcc lattice of 61 identical vortices in the unnormalised probability density distribution, $|\Psi|^2$, in time intervals of $2 \cdot 10^{-3}[\text{d.u.}]$. The total real-time evolution consisted of 10^3 iterations of a $10^{-5}[\text{d.u.}]$ time-step. Initially, the square lattice had $n^2 = 1000^2$ points and so the axes, which were defined from -4 to 4, are discretised into intervals of $h = 1/125$. $\{|\Psi|^2 > 10[\text{d.u.}], g = 15[\text{d.u.}], \omega_x = 100[\text{d.u.}], \omega_y = 150[\text{d.u.}], N = 1000\}$

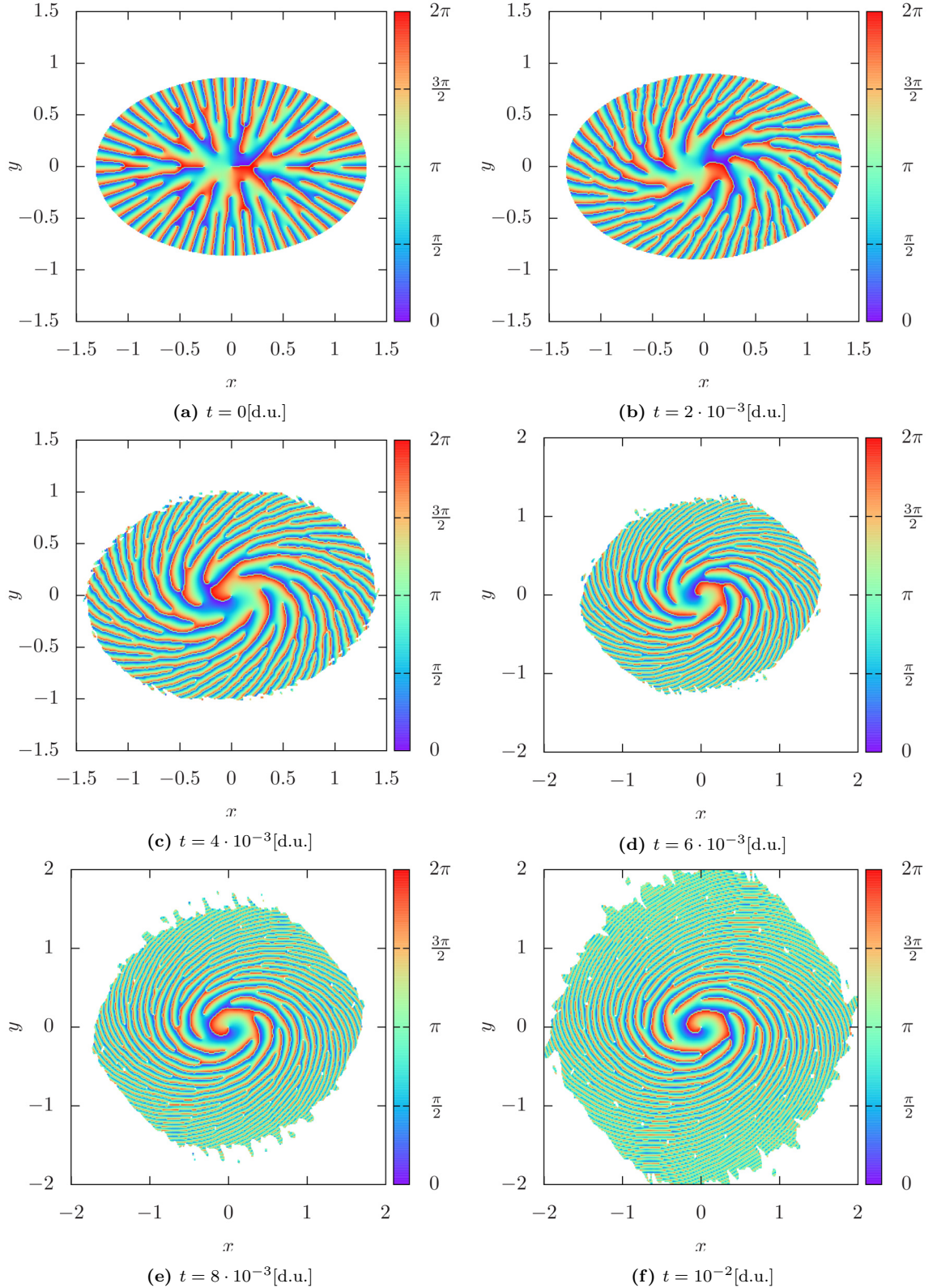


Figure D.22: Phase plots of the real-time expansion of an fcc lattice of 61 identical vortices, in time intervals of $2 \cdot 10^{-3}$ [d.u.]. The total real-time evolution consisted of 10^3 iterations of a 10^{-5} [d.u.] time-step. Initially, the square lattice had $n^2 = 1000^2$ points and so the axes, which were defined from -4 to 4, are discretised into intervals of $h = 1/125$. $\{|\Psi|^2 > 10\}$ [d.u.], $g = 15$ [d.u.], $\omega_x = 100$ [d.u.], $\omega_y = 150$ [d.u.], $N = 1000\}$

References

- [1] P. Weckesser, *Expansion Turbulenter Bose-Einstein Kondensate*, Bachelor thesis, Heidelberg University, Germany (2012).
- [2] E. A. L. Henn, J. A. Seman, G. Roati, K. M. F. Magalhães, and V. S. Bagnato, Emergence of Turbulence in an Oscillating Bose-Einstein Condensate, Phys. Rev. Lett. **103**, 045301 (2009).
- [3] Image source: http://upload.wikimedia.org/wikipedia/commons/thumb/6/6d/Triaxial_Ellipsoid.jpg/640px-Triaxial_Ellipsoid.jpg, [last accessed: 15/06/13].
- [4] M. Caracanhas, A. L. Fetter, S. R. Muniz, K. M. F. Magalhães, G. Roati, G. Bagnato, and V. S. Bagnato, Self-similar Expansion of the Density Profile in a Turbulent Bose-Einstein condensate, J. Low Temp. Phys. **166**, 49 (2012).
- [5] S. N. Bose, Plancks Gesetz und Lichtquantenhypothese, Z. Phys. **26**, 178 (1924).
- [6] A. Einstein, Quantentheorie des einatomigen idealen Gases, Sitzungber. K. Preuss. Akad. Wiss., Phys. Math. Kl. **1924**, 261 (1924).
- [7] A. Einstein, Quantentheorie des einatomigen idealen Gases. Zweite Abhandlung, Sitzungber. K. Preuss. Akad. Wiss., Phys. Math. Kl. **1925**, 3 (1925).
- [8] C. N. Yang, Remarks About Some Developments in Statistical Mechanics, AAPPS **5**, 2 (1995).
- [9] M. H. Anderson, J. Ensher, M. R. Matthews, C. E. Wieman, and E. A. Cornell, Observation of Bose-Einstein Condensation in a Dilute Atomic Vapour, Science **269**, 198 (1995).
- [10] K. B. Davis, M. O. Mewes, M. R. Andrews, N. J. van Druten, D. S. Durfee, D. M. Kurn, and W. Ketterle, Observation of Bose-Einstein Condensation in a Gas of Sodium Atoms, Phys. Rev. Lett. **75**, 3969 (1995).
- [11] L. Boltzmann, Weitere Studien über das Wärmegleichgewicht unter Gasmolekülen, Sitzungsber. K. Preuss. Akad. Wiss. **66**, 275 (1872).
- [12] E. Fermi, Sulla quantizzazione del gas perfetto monoatomico, Rend. Lincei **3**, 145 (1926).
- [13] The Nobel Prize in Physics 1962, http://www.nobelprize.org/nobel_prizes/physics/laureates/1962/ (1962).
- [14] E. M. Lifshitz and L. P. Pitaevskii, *Statistical Physics*, Peragmon Press, Oxford, UK (1980).
- [15] R. Feynman, *Progress in Low Temperature Physics*, North-Holland, Amsterdam, Holland (1955).
- [16] O. Penrose and L. Onsager, Bose-Einstein Condensation and Liquid Helium, Phys. Rev. **104**, 576 (1956).
- [17] L. Pitaevskii and S. Stringari, *Bose-Einstein Condensation*, Clarendon Press, Oxford, UK (2003).

- [18] C. J. Pethick and H. Smith, *Bose-Einstein Condensation in Dilute Gases*, Cambridge University Press, Cambridge, UK (2002).
- [19] The Nobel Prize in Physics 2001, http://www.nobelprize.org/nobel_prizes/physics/laureates/2001/ (2001).
- [20] A. Griffin, D. W. Snoke, and S. Stringari, *Bose-Einstein Condensation*, Cambridge University Press, Cambridge, UK (1995).
- [21] J. Klaers, J. Schmitt, F. Vewinger, and M. Weitz, Bose-Einstein condensation of photons in an optical microcavity, *Nature* **468**, 545 (2010).
- [22] J. Kasprzak, M. Richard, S. Kundermann, A. Baas, P. Jeambrun, J. M. J. Keeling, F. M. Marchetti, M. H. Szymańska, R. André, J. L. Staehli, V. Savona, P. B. Littlewood, B. Deveaud, and L. S. Dang, Bose-Einstein condensation of exciton polaritons, *Nature* **443**, 409 (2006).
- [23] J. Keeling and N. G. Berloff, Exciton-polariton condensation, *Contemp. Phys.* **52**, 131 (2011).
- [24] E. Gross, Structure of a quantized vortex in boson systems, *Nuovo Cimento* **20**, 454 (1961).
- [25] L. P. Pitaevskii, Bose-Einstein condensation in magnetic traps. Introduction to the theory, *Sov. Phys. JETP* **13**, 451 (1961).
- [26] S. Pathak, *An Introduction to Second Quantization*, http://www.phys.lsu.edu/~spathak/Talks/second_quantization.pdf, Lecture notes, Louisiana State University, USA (2010), [last accessed: 15/06/13].
- [27] N. Parker, *Numerical Studies of Vortices and Dark Solitons in Atomic Bose-Einstein Condensates*, Ph.D. thesis, University of Durham, UK (2004).
- [28] M. Cross, *Bose Condensation in Trapped Alkali Gases*, <http://www.pma.caltech.edu/~mcc/Ph127/c/Lecture7.pdf>, Lecture notes, California Institute of Technology, USA (2004), [last accessed: 15/06/13].
- [29] J. Schole, *Turbulenz in einem ultrakalten Bose Gas in zwei Dimensionen*, Diploma thesis, Heidelberg University, Germany (2011).
- [30] S. Erne, *Characterization of solitonic states in a trapped ultracold Bose Gas*, Diploma thesis, Heidelberg University, Germany (2012).
- [31] V. V. Kozlov, *Dynamical Systems X: General Theory of Vortices*, *Encyclopedia of Mathematical Sciences*, volume 67, Springer, Heidelberg, Germany (1998).
- [32] L. Onsager, Statistical Hydrodynamics, *Nuovo Cimento, Suppl.* **2** *6*, 249, 281 (1949).
- [33] B. Nowak, *Non-Thermal Fixed Points and Superfluid Turbulence in Ultracold Quantum Gases*, Ph.D. thesis, Heidelberg University, Germany (2012).
- [34] M. Karl, *The Emergence of Topological Defects and their Role in Non-Equilibrium Dynamics and Turbulence in an Ultracold Two-Component Bose Gas*, Master thesis, Heidelberg University, Germany (2012).
- [35] Image source: http://www.learner.org/courses/physics/visual/img_lrg/vortex_image.jpg, [last accessed: 15/06/13].
- [36] T. Gasenzer, Ultracold gases far from equilibrium, *EPJ ST* **168**, 89 (2009).
- [37] D. Tan and Z. Chen, *On A General Formula of Fourth Order Runge-Kutta Method*, <http://msme.us/2012-2-1.pdf>, *J. Math. Sci. & Math. Educ.*, Vol. 7, No. 2, Southern University, New Orleans, USA (2012), [last accessed: 15/06/13].
- [38] W. H. Press, S. A. Teukolsky, W. T. Vetterling, and B. P. Flannery, *Numerical Recipes in C (2nd ed.): the art of scientific computing*, Cambridge University Press, New York, USA (1992).

- [39] D. J. Griffiths, *Introduction to Quantum Mechanics*, Problem 2.22, Pearson Prentice Hall, New Jersey, USA (2005).
- [40] L. H. Thomas, The Calculation of Atomic Fields, Math. Proc. Cambridge Philos. Soc. **23**, 542 (1927).
- [41] E. Fermi, Un Metodo Statistico per la Determinazione di alcune Proprietà dell'Atomo, Rend. Accad. Naz. **6**, 602 (1927).
- [42] A. I. M. Rae, *Quantum Mechanics*, IoP Publishing, Bristol, UK (2007).
- [43] E. A. L. Henn, J. A. Seman, G. B. Seco, E. P. Olimpio, P. Castilho, G. Roati, D. V. Magalhães, K. M. F. Magalhães, and V. S. Bagnato, Bose-Einstein Condensation in ^{87}Rb : Characterization of the Brazilian Experiment, Braz. J. Phys. **38**, 279 (2008).
- [44] P. E. Matthews, *Bose-Einstein Condensates: Theory, Characteristics and Current Research*, Nova Science Publishers, New York, USA (2010).
- [45] P. G. Kevrekidis, D. J. Frantzeskakis, and R. Carretero-González, *Emergent Nonlinear Phenomena in Bose-Einstein Condensation, Atomic, Optical and Plasma Physics*, volume 45, Springer, Heidelberg, Germany (2008).
- [46] R. English, *Vortex Chaos in a Bose-Einstein Condensate*, Master thesis, Newcastle University, UK (2011).
- [47] The Nobel Prize in Physics 2003, http://www.nobelprize.org/nobel_prizes/physics/laureates/2003/ (2003).
- [48] A. A. Abrikosov, The Magnetic Properties of Superconducting Alloys, J. Phys. Chem. Solids **2**, 199 (1957).
- [49] Image source: <http://www.redorbit.com/images/pic/29514/big-vortex-lattice/>, [last accessed: 15/06/13].
- [50] J. P. Boyd, *Chebyshev and Fourier Spectral Methods*, Dover Publications, New York, USA (2000).
- [51] A. K. Leonhardt, *Expansion wechselwirkender Bose-Einstein-Kondensate*, Bachelor thesis, Heidelberg University, Germany (2011).
- [52] W. Bao, D. Jaksch, and P. A. Markowich, Numerical solution of the Gross-Pitaevskii equation for Bose-Einstein condensation, J. Comput. Phys. **187**, 318 (2003).
- [53] E. Guitton, Démonstration de la formule, Nuov. Ann. Math. **65**, 273 (1906).
- [54] L. H. Lyu, *Numerical Simulation of Space Plasmas, Appendix C: Higher-Order Numerical Integrations*, http://www.ss.ncu.edu.tw/~lyu/lecture_files_en/lyu_NSSP_Notes/Lyu_NSSP_AppendixC.pdf, Lecture notes, National Central University, Graduate Institute of Space Science, Jhongi City, Taiwan (2013), [last accessed: 15/06/13].
- [55] C. J. Farrar, *Vortex Interactions in Bose-Einstein Condensates*, Master thesis, Newcastle University, UK (2011).
- [56] C. Mungan, Density of States for a Particle in a Box, <http://www.usna.edu/Users/physics/mungan/Scholarship/DensityOfStates2.pdf>, USNA, Maryland, USA (2002), [last accessed: 07/04/13].
- [57] Bose-Einstein Condensation in 1, 2 and 3 dimensions for massive and massless bosons in a box, <http://www.physics.ucla.edu/~biritz/Comps/Solutions/01S/01S-13v2.pdf>, UCLA Physics & Astronomy exam solutions, California, USA (2007), [last accessed: 15/06/13].

Acknowledgements

First and foremost, I would like to thank Prof. Thomas Gasenzer for offering me the opportunity to pursue this exciting field of research. Quantum turbulence is an area that shows a lot of promise and I am sure that I will return to it in the future. By taking up this opportunity, I have been shown what it is like to work in a theoretical physics department. This will undoubtedly prove invaluable to me in making my choices for further study and ultimately, for my future career.

I would like to thank Pascal Weckesser for supporting me during my project. In particular, I would like to thank him for his help at the beginning, when I was at my most insecure. Taking the time and effort to talk with me regularly across six time-zones is something for which I am very grateful. I could not have hoped for a better guide to lead me through my project.

I would also like to thank Marcus Karl, Sebastian Erne, Andreas Samberg and Dr. Boris Nowak for their direct help with my thesis. They were always willing to help me with specific aspects of my work; something not many others could offer. Without them, it would have been a much more daunting task.

Furthermore, I would like to extend my thanks to everyone in the Far-From-Equilibrium Quantum Dynamics group for creating a friendly and open working environment and for answering any questions that I had, no matter how frivolous they may have sounded. It was a pleasure working in such a united group and I am sure that our paths will cross again. I wish everyone in the group the best of luck with their future endeavours.

I would like to thank my friends and family for supporting and encouraging me throughout my studies. Thank you for always finding time for me, even when I was very hard to bear. I always felt as though I had someone to talk to, whenever I had any difficulties. This thesis would not have been possible without you.

Last of all, I would like to additionally dedicate this thesis to Andrea Morger. Thank you for giving me the motivation to keep writing.

